

NASA/TM-1998-207668



Characterization of Al-Cu-Li Alloy 2090 Near Net Shape Extrusion

M. J. Birt

Analytical Services & Materials, Inc., Hampton, Virginia

M. S. Domack

Langley Research Center, Hampton, Virginia

R. A. Hafley and W. D. Pollock

Analytical Services & Materials, Inc., Hampton, Virginia

National Aeronautics and
Space Administration

Langley Research Center
Hampton, Virginia 23681-2199

May 1998

Acknowledgments

The authors would like to thank the other major participants who contributed to the program, specifically: Alcoa (K. P. Armanic); Boeing Aerospace and Defense Group (B. W. Libbey); Langley Research Center (T. T. Bales, W. B. Lisagor, J. A. Wagner); Marshall Space Flight Center (T. P. Vaughn); the National Institute of Standards and Technology (P. T. Purtscher); and Philips Laboratory, Air Force Systems Command (Lt. B. Pham) in the United States. The authors also wish to acknowledge the contributions made by researchers at the All-Russia Institute of Aviation Materials (J. Fridlyander) and the All-Russia Institute of Light Alloys (V. Davydov) in the Commonwealth of Independent States.

The use of trademarks or names of manufacturers in this report is for accurate reporting and does not constitute an official endorsement, either expressed or implied, of such products or manufacturers by the National Aeronautics and Space Administration.

Available from the following:

NASA Center for AeroSpace Information (CASI)
7121 Standard Drive
Hanover, MD 21076-1320
(301) 621-0390

National Technical Information Service (NTIS)
5285 Port Royal Road
Springfield, VA 22161-2171
(703) 487-4650

Contents

List of Tables	v
List of Figures	vi
Nomenclature	viii
Abstract	1
1. Introduction	1
2. Extruded Panels	2
2.1. Presentation of Data for Tables and Figures	2
2.2. Material and Processing	2
2.3. Inspection	4
3. Experimental Procedure	4
3.1. Microstructural Characterization	4
3.2. Tensile Tests	5
3.3. Fracture Tests	5
3.3.1. Part-through surface crack fracture tests	5
3.3.2. Through-crack fracture tests	5
3.4. Welding	5
3.5. Corrosion Tests	6
3.5.1. Exfoliation	6
3.5.2. Stress corrosion	7
4. Results and Discussion	7
4.1. Microstructural Characterization	7
4.1.1. Metallography	7
4.1.2. Texture analyses	8
4.2. Tensile Properties	14
4.3. Fracture Properties	21
4.3.1. Part-through surface crack tests	21
4.3.2. Through-crack fracture tests	22
4.4. Welding	29
4.4.1. Weldment tensile properties	29
4.4.2. Weldment fracture properties	29
4.5. Corrosion	32
4.5.1. Exfoliation	33
4.5.2. Stress corrosion	34
5. Concluding Remarks	38
6. References	39
Appendix A—Test Specimen Layout	42
Appendix B—Test Specimens	48
Appendix C—Test Results	57

List of Tables

Table 1.	Processing Parameters for 2090 Near Net Shape Extrusions	2
Table 2.	Test Matrix To Characterize 2090 Near Net Shape Extruded Panels	4
Table 3.	Summary of Variable Polarity Plasma Arc Welding (VPPAW) Parameters for 2090 Near Net Shape Extrusion	6
Table 4.	Summary of Surface Crack (PS(T)) Fracture Results	21
Table 5.	Summary of Tensile Properties of Welded 2090 and 2219 Alloys	32
Table 6.	Summary of Weldment Surface Crack (PS(T)) Fracture Results	32
Table 7.	Summary of Exfoliation Results for 2090 Products	33
Table 8.	Summary of Long Transverse Stress Corrosion Test Results for 2090 and 2219 Products	35
Table 9.	Summary of Short Transverse SCC Test Results for 2090 and 2219 Products.	37
Table C1.	Alcoa Tensile Data at 25°C, Panels 1 and 10	57
Table C2.	Boeing Aerospace Tensile Data at 25°C, Panels 4 and 7	57
Table C3.	Boeing Aerospace Tensile Data at -196°C, Panel 4	57
Table C4.	LaRC Tensile Data at 25°C, Panels 11, 6, 4, and 2	58
Table C5.	MSFC Tensile Data at 25°C, Panels 11 and 2	59
Table C6.	MSFC Tensile Data at -196°C, Panels 11 and 2	59
Table C7.	MSFC Tensile Data at -253°C, Panels 11 and 2	60
Table C8.	Boeing Aerospace Surface Crack (PS(T)) Fracture Tests, Panels 4 and 7	60
Table C9.	NIST Surface Crack (PS(T)) Fracture Tests, Panel 6	61
Table C10.	Tensile Properties for 2090 Near Net Shape Extrusion and Other Aluminum Products.	61
Table C11.	Boeing Aerospace Weldment Tensile Data, Panels 4 and 7	62
Table C12.	Boeing Aerospace Weldment Surface Crack (PS(T)) Fracture Tests, Panels 4 and 7	62
Table C13.	NIST Weldment Surface Crack (PS(T)) Fracture Tests, Panel 3	63
Table C14.	Alcoa Exfoliation Test Data for 2090-T86 Extrusion, Panel 6	63
Table C15.	Alcoa MASTMAASIS Exfoliation Test Data for 2090-T86 Extrusion, Panel 6	63
Table C16.	LaRC Direct-Tension Stress Corrosion Data for 2090-T86 Extrusion, Panel 6	64
Table C17.	LaRC Stress Corrosion Data for the Modified c-Ring Specimen, 2090-T86 Extrusion, Panel 6	64

List of Figures

Figure 1.	Extruded 2090 panel in as-received condition	3
Figure 2.	Schematic section of extruded panel (nominal dimensions in mm).	3
Figure 3.	Triplanar optical micrograph of center of skin (anodized by using Barker's reagent and viewed under cross-polarized light).	8
Figure 4.	Triplanar optical micrograph of center of cap (anodized by using Barker's reagent and viewed under cross-polarized light).	8
Figure 5.	Skin-stiffener cross section showing microstructural variations resulting from extrusion process (anodized with Barker's reagent and viewed under cross-polarized light)	9
Figure 6.	Texture results for midplane of cap	10
Figure 7.	Texture results for midplane of web.	11
Figure 8.	Texture results for midplane of skin.	12
Figure 9.	Texture results for midplane of base	13
Figure 10.	Panel-to-panel variation in yield strength and elongation to failure. Results for all LT skin tests at 25°C for each panel (bars represent range of data).	14
Figure 11.	Variation in yield strength and elongation to failure along panel length. Results for panel 11 L skin, LT skin, and LT base at 25°C. Bars represent range of data	15
Figure 12.	Variation in stress-strain behavior with respect to panel element and orientation. Individual tests at 25°C from center of panel 11	15
Figure 13.	Variation in yield strength and elongation to failure with panel element. LaRC results for panels 6 and 11 (T86) and panel 2 (T8E46) at 25°C. Bars represent range of data	15
Figure 14.	Variation in yield strength with temperature for various 2090 product forms and 2219 plate. Bars represent range of data.	17
Figure 15.	Variation in elongation to failure with temperature for various 2090 product forms and 2219 plate. Bars represent range of data	17
Figure 16.	Through-thickness cross section of tensile failure in base tested at 25°C in the LT orientation.	18
Figure 17.	Typical intersubgranular tensile failure at 25°C showing pancake-shaped grains.	18
Figure 18.	Typical tensile failure in skin tested at 25°C in 45° orientation.	19
Figure 19.	Typical tensile failure in skin tested at -196°C in LT orientation	20
Figure 20.	Effect of surface crack shape and temperature on toughness. Results for individual tests at NIST on panel 6 in T-S orientation	22
Figure 21.	Comparison of surface crack test results from Boeing Aerospace for 2090 extrusions with 2090 plate	22
Figure 22.	Through-thickness cross sections of 2090 PS(T) fracture specimens (anodized with Barker's reagent and viewed under cross-polarized light).	23
Figure 23.	Fracture surface of PS(T) specimen in L-S orientation at 25°C.	24
Figure 24.	Fracture surface of PS(T) specimen in T-S orientation at 25°C.	25
Figure 25.	Fracture surface of PS(T) specimen in L-S orientation at -196°C.	26
Figure 26.	Fracture surface of PS(T) specimen in T-S orientation at -196°C.	27
Figure 27.	Comparison of the resistance to stable tearing of 2090-T86 extrusion with 2219-T87 plate in L-T orientation at 25°C. Data from M(T) specimens	28

Figure 28.	Effect of orientation on fracture behavior of 2090-T86 extrusion at 25°C. Data from M(T) specimens	28
Figure 29.	Effect of temperature on fracture behavior of 2090-T8E46 extrusion in L-T orientation. Data from M(T) specimens	28
Figure 30.	Effect of stretch on fracture behavior of 2090 extrusion in L-T orientation at 25°C. Data from M(T) specimens.	28
Figure 31.	Effect of stretch on fracture behavior of 2090 extrusion in T-L orientation at 25°C. Data from M(T) specimens.	28
Figure 32.	SEM fractography of 2090-T8E46 extrusion M(T) specimens tested at 25°C in L-T orientation	30
Figure 33.	SEM fractography of 2090-T8E46 extrusion M(T) specimens tested at -196°C in L-T orientation	31
Figure 34.	General appearance of 2090-T86 exfoliation specimens after EXCO and dry bottom MASTMAASIS exposures.	34
Figure 35.	The 2090-T86 MASTMAASIS exfoliation specimens illustrating pitting attack with undercutting	34
Figure 36.	Variation in breaking stress with exposure stress for 2090-T86 long transverse direct-tension specimens. Bars represent range of data	35
Figure 37.	Long transverse 2090-T86 direct-tension specimen illustrating pitting attack along material flow lines associated with extrusion process	36
Figure 38.	Pitting attack on 2090-T86 modified c-ring	38
Figure A1.	Specimen locations in panel 2	43
Figure A2.	Specimen locations in panel 6	44
Figure A3.	Specimen locations in panel 11	45
Figure A4.	Specimen locations in panel 4	46
Figure A5.	Specimen locations in panel 7	47
Figure B1.	LaRC and Alcoa subsized tensile specimen (full-panel thickness). Dimensions are in mm	48
Figure B2.	MSFC tensile specimen (full-panel thickness). Dimensions are in mm.	48
Figure B3.	Boeing Aerospace base metal tensile specimen. Dimensions are in mm.	48
Figure B4.	NIST large PS(T) specimen (full-panel thickness). Dimensions are in mm	49
Figure B5.	NIST small PS(T) specimen (full-panel thickness). Dimensions are in mm	49
Figure B6.	Boeing Aerospace PS(T) specimen. Dimensions are in mm	50
Figure B7.	LaRC M(T) specimen (full-panel thickness). Dimensions are in mm	50
Figure B8.	Boeing Aerospace weldment tensile specimen. Dimensions are in mm	51
Figure B9.	Boeing Aerospace weldment PS(T) specimen. Dimensions are in mm.	52
Figure B10.	Alcoa exfoliation corrosion test specimen for EXCO test (full-panel thickness). Dimensions are in mm	52
Figure B11.	Alcoa exfoliation corrosion test specimens for dry bottom MASTMAASIS test (full-panel thickness). Dimensions are in mm	53
Figure B12.	LaRC direct-tension stress corrosion specimen	54
Figure B13.	LaRC modified c-ring stress corrosion specimen. Dimensions are in mm	55
Figure B14.	Loading methods and resulting tensile stresses for modified c-ring specimen	56

Nomenclature

Alcoa	Aluminum Company of America
ASTM	American Society for Testing and Materials
a	crack depth
a/c	aspect ratio of crack depth to half-surface crack length
B	overall specimen thickness
CIS	Commonwealth of Independent States
c	width of notch
DB	dry bottom (MASTMAASIS) test
dA/dK	fatigue crack growth rate
ED	rating per ASTM G34 denoting very severe exfoliation
E.D.	extrusion direction
EDS	energy dispersive spectroscopy
El	elongation
ET	Space Shuttle external tank
EXCO	exfoliation corrosion
GTA	gas tungsten arc welding
HAZ	heat affected zone
ID	inner diameter
K_{CU}	impact toughness
K_{Ie}	effective mode I stress intensity
K_R	crack extension resistance
kN	breaking load
L	longitudinal (extrusion) direction
LaRC	Langley Research Center
LCF	low cycle fatigue
LS	metallurgical plane containing both L and S orientations
L-S	fracture plane normal to L with propagation in S direction
LT	metallurgical plane containing both L and T orientations
L-T	fracture plane normal to L with propagation in T direction
MAM	metric aerospace materials
MASTMAASIS	modified acetic acid salt intermittent spray
MSFC	Marshall Space Flight Center
M(T)	middle-crack tension specimen
NIST	National Institute of Standards and Technology
OD	outer diameter
ODF	orientation distribution function
PS(T)	part-through surface crack specimen
S	short transverse (thickness) direction
S_{net}	net section stress
S_u	ultimate stress
S_y	yield stress

SAE	Society of Automotive Engineers
SCC	stress corrosion cracking
SEM	scanning electron microscope
SPEC	specification
T	long transverse (width) direction
T.D.	transverse direction
TL	denotes metallurgical plane containing both T and L orientations
T-L	denotes fracture plane normal to T with propagation in L direction
TS	denotes metallurgical plane containing both T and S orientations
T-S	denotes fracture plane normal to T with propagation in S direction
VIAM	All-Russia Institute of Aviation Materials
VILS	All-Russia Institute of Light Alloys
VPPAW	variable polarity plasma arc welding
<i>W</i>	specimen width
WDS	wavelength dispersive spectroscopy
σ_{ys}	yield stress
3G	vertical up welding position

Abstract

Aluminum-lithium (Al-Li) alloy near net shape extrusions are being evaluated for potential application in launch vehicle structures. The objective of this study was to determine tensile and fracture properties, corrosion resistance, and weldability of integrally stiffened panels of Al-Cu-Li alloy 2090 in the T8 temper. The microstructure was predominantly unrecrystallized. Texture analyses revealed the presence of fiber components in the stiffeners and a combination of fiber and rolling components in the skin. Variations in grain morphology and texture through the extruded cross section were correlated with the tensile, fracture, and corrosion behavior. Tensile strengths at room and cryogenic temperatures of the 2090 extrusions were similar to other 2090 product forms and were higher than aluminum alloy 2219-T87, the primary structural material in the Space Shuttle external tank; however, ductilities were lower. The fracture resistance of the 2090 extrusion was lower than 2219-T87 plate at room temperature. At cryogenic temperatures, tensile ductility and fracture behavior of the 2090 extrusion were similar to other 2090 product forms but were lower than 2219-T87 plate. The exfoliation and stress corrosion resistance of the 2090 extrusion compared favorably with the characteristics of other 2090 product forms. The weldability and weldment properties of the extrusions were similar to 2090 and 2219 plates.

1. Introduction

Low density aluminum-lithium (Al-Li) alloys offer significant cost-saving advantages over conventional aluminum alloys where weight is a premium. For example, the cost-to-orbit of a kilogram of payload is more than \$4400 in an existing launch vehicle such as the Atlas/Centaur (ref. 1). Therefore, the structural weight savings achieved by using Al-Li alloys convert directly into payload savings. Launch vehicle components, including cryotanks and dry bay structures in the Space Shuttle external tank (ET), are possible applications where Al-Li alloys could replace conventional aluminum alloys. Manufacture of the ET currently involves integrally machining thick plate 2219 aluminum alloy, which produces in excess of 80 percent scrap material. Since the material cost of Al-Li alloys is approximately three to five times higher than 2219 Al alloy, near net shape manufacturing processes (including extrusion, spin forming, and roll forging), in which material scrap is reduced to ~15 percent, are being considered as alternatives for the ET (ref. 2).

A collaborative team effort was established between several laboratories to examine and evaluate the properties of Al-Cu-Li alloy 2090 in the form of a near net shape extrusion. The team included Langley Research Center (LaRC), Marshall Space Flight Center (MSFC), the National Institute of Standards and Technology (NIST), Philips Laboratory, Air Force Systems Command, and private industry (Aluminum Company of America (Alcoa) and Boeing Aerospace) laboratories in the United States, together with the All-Russia Institute

of Aviation Materials (VIAM), and the All-Russia Institute of Light Alloys (VILS) in the Commonwealth of Independent States (CIS). The preliminary results and interpretation of the study presented herein on the 2090 near net shape extrusions are part of an ongoing effort and cover work completed to date by laboratories in the United States.

The objective of the study was to determine the effect of the near net shape extrusion process on the properties of 2090 and the feasibility of producing, by extrusion, an integrally stiffened panel similar to a machined barrel section used in the structure of the ET. In producing the extruded panels, no effort was made to meet any specific design requirement for aerospace Al alloy products. The extruded panels were fabricated on a best effort basis by using an extrusion press and die which were regularly used for the extrusion of a variety of commercial Al alloys but that had not been modified for the 2090 alloy. In order to address the ET service conditions, tensile and fracture testing was conducted at both cryogenic and room temperatures. Weldability and corrosion resistance were also major concerns because most Al cryotanks are welded during fabrication, and once fabricated, tanks may be stored for a considerable length of time before use. Therefore, tensile and fracture data from weldments and general corrosion and stress corrosion cracking data were also obtained for the near net shape extrusion. In the study, data generated for the 2090 near net shape extrusion have been compared with other 2090 product forms and conventional aerospace aluminum alloys, where appropriate.

2. Extruded Panels

2.1. Presentation of Data for Tables and Figures

Extrusion processing information, the characterization test matrix, results from metallurgical analysis, and summary mechanical property test data are presented in tables 1 through 9 and in figures 1 through 38. The location and orientation of test specimens machined from the extruded panels are provided in appendix A, figures A1 through A5. The specimen configurations used for tensile, fracture, and corrosion testing are provided in appendix B, figures B1 through B14. Results from individual test specimens are compiled in appendix C, tables C1 through C17.

2.2. Material and Processing

The nominal composition of the 2090 Al-Cu-Li alloy was determined by the All-Russia Institute of Light Alloys (VILS) on the ingot material prior to extrusion and by Langley Research Center (LaRC) and Aluminum Company of America (Alcoa) on the extruded panels. The LaRC results obtained by using inductively coupled plasma atomic spectroscopy on panel 11 were 2.72Cu, 2.07Li, 0.12Zr, 0.090Fe, 0.05Si, 0.03Ti, balance Al (in weight percent), which are typical for all panels examined.

The 2090 alloy was cast by Alcoa into rectangular ingots ~400 mm wide by 1270 mm long. The ingots were machined into 12 round billets, each 360 mm in diameter by 1000 mm long. The billets were then broach forged by VILS at temperatures between 380° to 420°C into hollow cylindrical billets of 418 mm OD by 306 mm ID by 640 mm long. The hollow billets were extruded by VILS into cylinders 4 m long with eight L-shaped stiffeners formed equidistant on the outside of the cylinder. The

extrusion process was performed by direct means on a horizontal hydraulic press with a central mandrel to maintain constant wall thickness and concentricity. The extrusion processing parameters for individual panels are shown in table 1. The near net shape extrusions were slow air cooled out of the die, cut along the length, gripped at the edges along the length, and mechanically unfolded on a convex table. The extrusions were then flattened by using a rolling mill equipped with a flat plate to support the extrusions. The plate contained grooves for the stiffeners to maintain contact between the plate and the surface of the extrusions during rolling. The degree of deformation introduced by rolling is unknown because the thickness of the extrusions and the variation in curvature before rolling were not measured. The panels were then solution heat treated at 545°C for 45 min and were water quenched, stretched to a nominal 3 percent or 6 percent (as shown in table 1), and were finally flattened by cold rolling. After cropping, the panels had seven stiffeners and final dimensions of 825 mm wide by 3 m long. Alcoa heat treated the panels by using two different practices to achieve the same near peak-aged tensile properties. The two heat treatments were T86 (stretched 6 percent and aged 30 hours at 160°C) and T8E46 (stretched 3 percent and aged by a proprietary practice). A representative photograph of a panel is shown in figure 1, and the nominal dimensions are indicated in a schematic in figure 2.

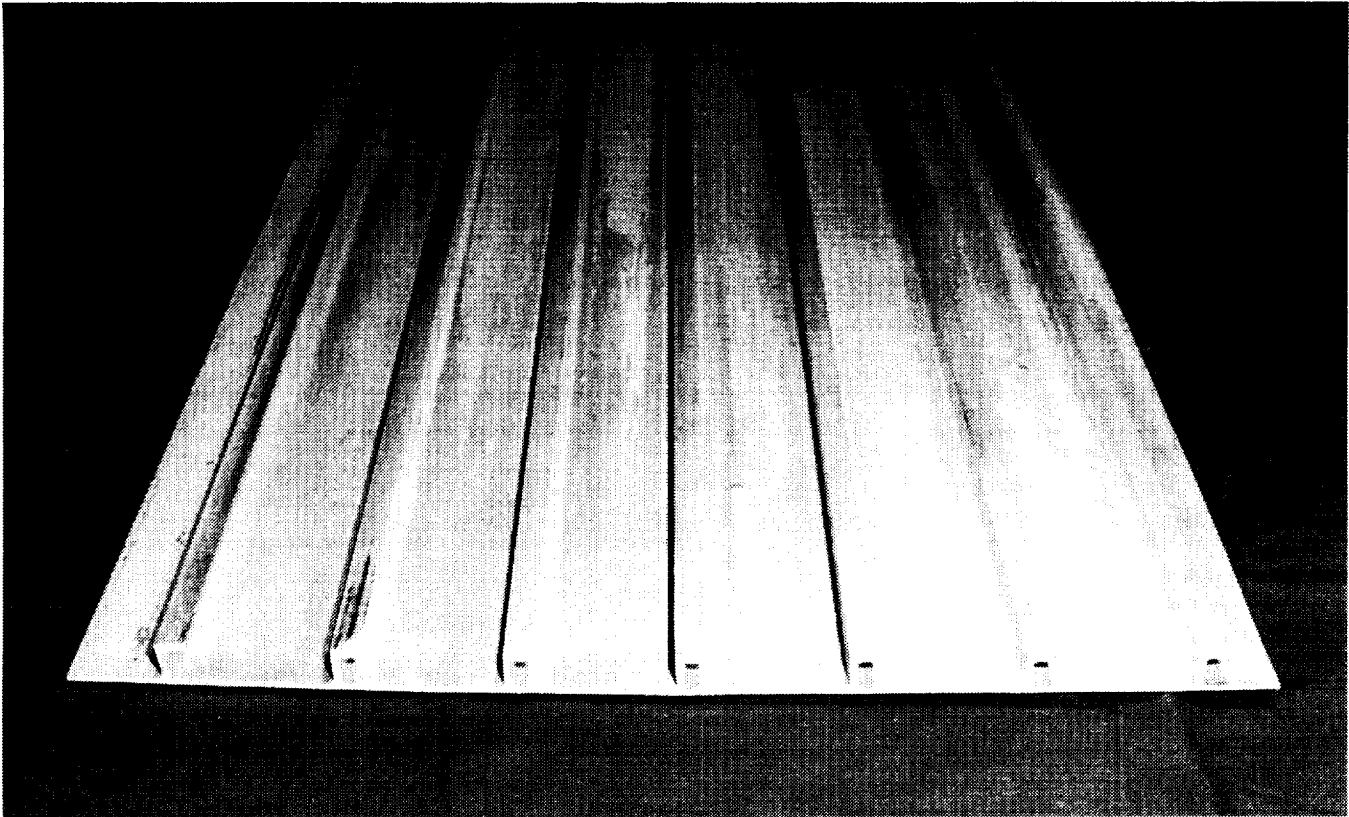
Table 2 shows a matrix indicating the tests which were originally proposed by individual laboratories and which have been completed or are pending completion, together with the panel designations. Panels 8 and 9 were held in reserve. The test matrix was structured to examine panel-to-panel and interlaboratory variations and included microstructural characterization, tensile, fracture, and corrosion testing.

Table 1. Processing Parameters for 2090 Near Net Shape Extrusions

Panel number	Billet temperature, °C	Container temperature, °C	Extrusion rate, m/min	Preaging stretch, percent			Nominal stretch, percent
				Outlet	Central	Residual	
1	360	390	0.4	5.5	5.5	5.5	a ₆
2	400	390	.6	3.0	3.0	3.0	b ₃
3	420	420	.6	6.0	5.0	6.0	a ₆
4	400	390	.6	5.0	5.0	5.5	a ₆
5	400	390	.6	5.5	5.0	5.5	a ₆
6	400	400	.6	6.0	5.0	6.0	a ₆
7	400	390	.6	2.5	2.5	2.5	b ₃
8	360	390	.4	2.5	2.0	2.0	b ₃
9	440	435	.6	5.0	5.0	5.0	a ₆
10	400	410	.6	3.0	3.0	3.0	b ₃
11	400	400	.6	6.0	6.0	6.0	a ₆
12	400	390	.6	2.0	2.0	2.0	b ₃

^aMaterial aged to -T86.

^bMaterial aged to -T8E46.



250 mm

Figure 1. Extruded 2090 panel in as-received condition.

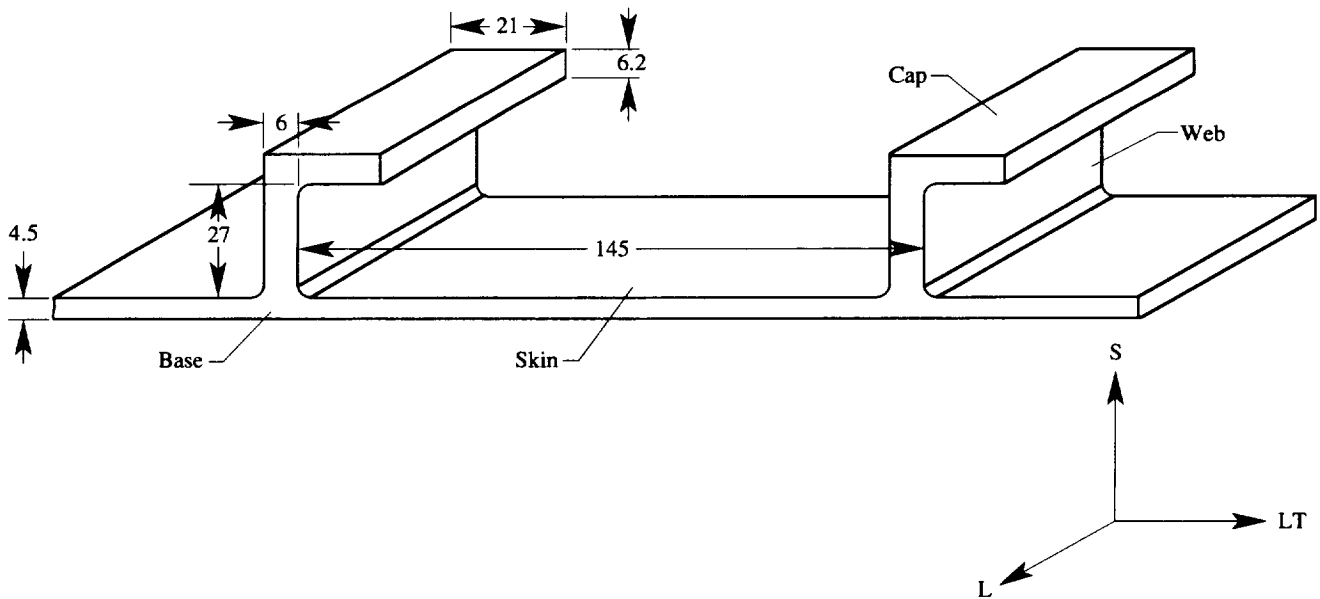


Figure 2. Schematic section of extruded panel (nominal dimensions in mm).

Table 2. Test Matrix To Characterize 2090 Near Net Shape Extruded Panels

Tests	Laboratories					
	LaRC	MSFC	NIST	Alcoa	Boeing Aerospace	VIAM, VILS
Panel	2, 4, 6, 11	2, 3, 11	3, 6	1, 6, 10	4, 7	5, 12
Wet chemistry	(a)			(a)		(a)
Hydrogen concentration	(a)	(b)		(a)		(a)
Optical metallography	(a)			(a)		(a)
TEM	(b)			(a)		(a)
Texture						
Tensile (ASTM E8)						
RT	(a)	(a)		(a)	(a)	(a)
LN ₂		(a)			(a)	(a)
LH ₂ or LHe		(a)				(a)
Fatigue						(a), (e)
Fracture toughness						
RT	(b), (c)		(a), (d)		(a), (d)	(a), (f), (g)
LN ₂	(b), (c)		(a), (d)		(a), (d)	(a), (f)
LH ₂ or LHe	(b), (c)		(a), (d)			(a), (f)
Corrosion						
General corrosion		(b)		(a)		(a)
Stress corrosion	(a)	(b)				(a)
Weldability		(a)			(a)	(a)
Inspection						
Dimensions and internal flaws					(a)	

^aComplete.

^bIn progress.

^cK_R.

^dK_{Ic}.

^eLCF, dA/dN at 25°C and -253°C.

^fK_{CU}.

^gImpact.

2.3. Inspection

Panels 4 and 7 were inspected for dimensional tolerances and general quality by the Boeing Defense and Aerospace Group. The panels were nondestructively examined by visual, dye penetrant, and ultrasonic inspection. Panels were investigated with regard to internal defects, surface corrosion, and damage. Visually, the surfaces of the panels appeared discolored in certain areas; dye penetrant examination associated these areas with microporosity (<0.5 mm) and macroporosity (~1.3 mm) as a result of surface corrosion. Ultrasonic examination, using a scan with a resolution of ~1 mm diameter, revealed that there were no internal defects. Test specimens were taken from areas which were obviously free of corrosion damage and other surface defects. Under visual examination it was noted that some stiffeners were bent, and damage in the form of surface gouges was present. Dimensional tolerances were measured in accordance with Society of Automotive Engineers (SAE) specification Metric Aerospace Materials (MAM) 2205 (ref. 3). Although the thickness of the panels met the specification, measurements of the waviness between the stiffeners and the flatness of the panels did not meet nor-

mally allowed manufacturing tolerances for aerospace aluminum alloy extruded shapes in the United States (ref. 3).

3. Experimental Procedure

3.1. Microstructural Characterization

Metallurgical examination and texture analysis were performed by LaRC to characterize the microstructure associated with processing and to correlate results with tensile, fracture, and corrosion properties. Optical metallography specimens to examine grain morphology were anodized by using Barker's reagent and were viewed under cross-polarized light. Triplanar micrographs were prepared from samples taken from the skin and cap of panel 11. A full cross section was prepared in the T-S plane to include both stiffener and skin from panels 2, 6, and 11. Additional specimens were prepared by using Graff-Sargent reagent and conventional bright field viewing conditions to look for constituent particles. Energy dispersive spectroscopy (EDS) and wavelength dispersive spectroscopy (WDS) were used to identify constituent particles.

Measurements of preferred orientation were carried out by Alcoa and LaRC to determine the effects of texture on mechanical properties. The texture data included in this report were generated at LaRC on panel 11. In all cases, specimens for texture examination were taken from the midplane of the panel element to correlate with the data from tensile and fracture specimens. Data were collected by using the Schultz backward reflection technique over an area ~24 mm in diameter.

3.2. Tensile Tests

Tensile tests were conducted by Alcoa (panels 1 and 10), Boeing Aerospace (panels 4 and 7), LaRC (panels 2, 4, 6, and 11), and MSFC (panels 2 and 11), as shown in table 2. Specimens were machined from several locations along the length of each panel, as shown in appendix A. For panels 2, 6, and 11, multiple specimens were machined at each tensile location at positions in the stiffener and in the skin as shown in the detail view in figures A1 through A3. Individual specimen orientations and locations are shown for panels 4 and 7 in figures A4 and A5. Layouts were not provided by test labs for panels 7 and 10. Testing was performed, where possible, in the longitudinal (extrusion) direction (L), and in the 45° and long transverse (LT) orientations with respect to the extrusion direction (L). The test specimen configurations are shown in appendix B, figures B1 through B3. Tensile data were obtained by using specimens which were either full thickness or that were machined about the midplane to ~3.2 mm, which is the existing external tank (ET) wall thickness. Tests were conducted at three temperatures: ambient (25°C), liquid nitrogen (-196°C), and liquid hydrogen (-253°C). Testing was in accordance with American Society for Testing and Materials (ASTM) B557-84 (ref. 4) or ASTM E8-89 (ref. 5). Boeing Aerospace and Marshall Space Flight Center (MSFC) tested standard size specimens, and Alcoa and LaRC tested subsized specimens. The actual number of specimens tested and the dimensions are indicated in appendix C, tables C1 through C7. Elongation to failure was determined by measuring across fitted halves of fractured specimens with gauge marks (MSFC, Alcoa) or by subtracting the calculated elastic strain from the total measured strain (LaRC). Although each laboratory tested a different size tensile specimen and different methods were used to determine elongation to failure, all procedures were in accordance with ASTM B557-84 or E8-89. Examination of tensile specimen fracture surfaces was performed at LaRC on specimens tested at 25°C by LaRC and at -196°C by Boeing Aerospace.

3.3. Fracture Tests

Fracture testing was carried out by using part-through surface crack (PS(T)) and through crack speci-

mens to determine residual strength and fracture resistance, respectively. Boeing Aerospace and the National Institute of Standards and Technology (NIST) performed the part-through surface crack tests, and LaRC conducted the through-crack tests. Fracture behavior was determined over a range of temperatures in both the transverse and longitudinal directions with respect to the extrusion direction. Testing was in accordance with the relevant ASTM specifications as indicated in section 3.3.1.

3.3.1. Part-through surface crack fracture tests.

Surface crack fracture tests were performed on skin material and weldments by Boeing Aerospace (panels 4 and 7) and by NIST (panel 6) in accordance with ASTM E740-88 (ref. 6). Part-through surface crack specimens were machined in both the L-S (denotes fracture plane normal to L with propagation in the short transverse direction) and T-S orientations, as shown in appendix A, figures A2, A4, and A5. In all cases specimens were taken from skin material with the stiffeners machined off. NIST tested specimens which were the full skin thickness (4.0 to 4.9 mm), shown in appendix B, figures B4 and B5, while Boeing Aerospace tested specimens which were machined about the midplane to the existing ET wall thickness (3.2 mm), as shown in figure B6. Surface cracks were either semicircular or semielliptical with dimensions for individual specimens shown in appendix C, tables C8 and C9. Surface crack tests were conducted at three temperatures: ambient (25°C), liquid nitrogen (-196°C), and liquid helium (-269°C). Optical microscopy and scanning electron microscopy (SEM) were used to examine the fracture surfaces.

3.3.2. Through-crack fracture tests. Fracture toughness behavior was characterized from crack growth resistance tests (R-curves) performed on skin material at LaRC (panels 2 and 11) in accordance with ASTM E561-86 (ref. 7). Crack growth was measured by using the compliance technique. The R-curves were generated from full thickness middle-cracked tension (M(T)) specimens machined from several locations along the length of the extrusion in the L-T and T-L orientations, as shown in appendix A, figures A1 and A3. As with the part-through surface crack tests, specimens were taken from skin material with the stiffeners machined off. The dimensions of the test specimens are shown in appendix B, figure B7. Tests were conducted at two temperatures: ambient (25°C) and liquid nitrogen (-196°C). Optical microscopy and SEM microscopy were used to examine the fracture surfaces.

3.4. Welding

Panels 4 and 7 were evaluated for weldability by Boeing Aerospace, while MSFC evaluated panel 3. The

location of weld panel specimens for panels 4 and 7 are shown in appendix A, figures A4 and A5, respectively. A specimen layout was not provided for panel 3. Sections from panels were variable polarity plasma arc welded (VPPAW) and inspected in accordance with MSFC-SPEC-504C (ref. 8). Welding parameters were varied to determine weld schedules, which are shown in table 3. Sections welded at MSFC were full thickness and 229 or 279 mm wide by 610 mm long, while those welded at Boeing Aerospace were 152 mm wide by 610 mm long and were machined from the midplane to a nominal 3.2 (2.7 to 3.8) mm. Stiffeners were machined off prior to welding. Joint preparation at Boeing Aerospace consisted of dry machining the abutting edges, followed by chemical cleaning and wire brushing. MSFC also dry-machined the abutting edges but used manual scraping prior to welding. The filler wire was 2319 Al alloy, which has become standard for Al-Cu-Li alloys joined by arc welding processes (refs. 9 and 10). Clamping techniques were modified by Boeing Aerospace to accommodate flatness and thickness variations. All sections were welded in the 3G (vertical up) position with inert gas backside shielding. Boeing Aerospace measured the weldment tensile properties by using the specimen shown in appendix B, figure B8. Boeing Aerospace evaluated fracture behavior on panels 4 and 7 by using the specimen shown in figure B9, and NIST evaluated panel 3, welded at MSFC, by using the specimen shown in figure B5.

3.5. Corrosion Tests

Corrosion studies were performed to determine how the extrusion process affected the corrosion properties of

near peak-aged 2090. Corrosion tests were performed on panel 6 by LaRC and Alcoa to document the corrosion resistance, to evaluate whether material flow associated with the extrusion process created preferential corrosion paths, and to show that residual stresses did not exist in magnitudes that would support stress corrosion cracking. Properties in the short transverse orientation of the stiffener web and in the transverse orientation beneath the web were of particular interest because short transverse stress corrosion failures have been reported in 2090 thick plate (ref. 11). All corrosion tests were performed with material from the location shown in appendix A, figure A2. The orientation and dimensions of the corrosion test specimens are provided in appendix B, figures B10 through B13.

3.5.1. Exfoliation. Alcoa conducted exfoliation tests by using both the exfoliation corrosion (EXCO) test described in ASTM G34-90 (ref. 12), and the dry bottom modified acetic acid salt intermittent spray (MASTMAASIS) test described in ASTM G85-85, Annex 2 (ref. 13), and by Colvin and Murtha (ref. 14). The EXCO test involves continuous immersion in an acidified salt solution followed by visual inspection of the specimen surface. Specimens from the 2090 extrusion were exposed for four days, as is recommended in ASTM G34 for 2XXX aluminum alloys, and were inspected and rated daily. The MASTMAASIS procedure is a modified salt spray test and involves cyclic exposure to an acidified salt fog within an environmental chamber. Dry bottom refers to an additional test modification which requires draining residual liquid from the chamber during the drying cycle to lower the chamber

Table 3. Summary of Variable Polarity Plasma Arc Welding (VPPAW) Parameters for 2090 Near Net Shape Extrusion

(a) Welding Schedule

Lab	Pass	Welding current, A	Welding voltage, volts	Travel rate, mm/s	Wire feed rate, mm/s	Wire diameter, mm	Electrode diameter, ^b mm	Orifice diameter, mm
MSFC	Root	95	22.6	4.1	23.3	1.6	3.96	3.18
	Cover	70	21	3.6	4.2	1.6	3.96	3.18
Boeing	Root	^a 60,48	31	3.2	15.2	1.6	3.18	

^aPulsed current, 0.250 s at 60 A, 0.150 s at 48 A.

^bType, 2-percent thoriated tungsten.

(b) Welding Gas Flow Rates

Lab	Pass	Shield gas	Shield gas flow rate, l/s	Backside shield gas flow rate, l/s	Plasma gas	Plasma gas flow rate, l/s
MSFC	Root	Helium	0.55	0.79	Argon	0.04
	Cover	Helium	0.55	0.55	Argon	0.02
Boeing	Root	Helium	0.79	0.79	75% argon, 25% helium	

humidity. Specimens from the 2090 extrusion were exposed for four weeks with inspection and rating at one-, two-, and four-week intervals. For both procedures, specimen evaluation is based on comparison with standard photographs provided in ASTM G34-90 to rate the extent of attack. Two specimen configurations were used: one which tested the skin between stiffeners, as shown in appendix B, figures B10 and B11(b), and one which tested both skin and stiffeners, as shown in figure B11(a). Specimens from the skin were exposed to each of the EXCO and MASTMAASIS environments. Two extrusion sections were exposed by the dry bottom MASTMAASIS procedure, one with the stiffeners facing up and the other with the stiffeners facing down. Metallographic sections were prepared after exposure to determine the corrosion morphology.

3.5.2. Stress corrosion. LaRC performed stress corrosion testing by using both direct-tension and modified c-ring specimens. Direct-tension specimens (appendix B, fig. B12(a)) were prepared and tested according to ASTM G49-85 (ref. 15). The specimens were machined in the long transverse orientation with the middle of the reduced section centered beneath the stiffener web, as shown in appendix B, figure B12(b). Specimens were initially loaded to applied stress levels equivalent to 25 percent, 50 percent, and 75 percent of the yield stress (S_y) under constant displacement conditions. The specimen exposure load was based on LT base mechanical properties and was verified by specimen extension that was measured with an extensometer for each specimen during loading. Triplicate specimens were exposed for 40 days to a 3.5-percent NaCl solution by alternate immersion according to ASTM G44-88 (ref. 16). Residual strength measurements (breaking load divided by original cross-sectional area) were obtained for each specimen after exposure. Unstressed specimens were also exposed to determine the reduction in residual strength due to general corrosion. Metallographic sections were prepared from selected specimens to examine the corrosion morphology.

A modified c-ring specimen was devised to test the stress corrosion resistance of the stiffener web under short transverse loading. Modified c-ring specimens were machined to include the stiffener cap and web as well as skin material extending to either side of the web (appendix B, fig. B13). Two loading methods were used to control the location of tensile stresses, as illustrated in appendix B, figure B14. In the first method, figure B14(a), the stiffener cap was pulled down, causing tensile stresses on the outer surface of the web and at the fillet formed by the web-skin intersection. In the second method, figure B14(b), the stiffener cap was pushed up, causing tensile stresses on the inside surface of the web

and at the fillets formed by the cap-web and the web-skin intersections. A modified c-ring instrumented with strain gauges was used to evaluate the strains in the web and at the web-skin and cap-web fillet during loading. The resulting strain distribution with specimen height, measured at the loading bolt, was used as a loading curve for the specimens. The c-rings were loaded such that the maximum stress was 70 percent S_y . Short transverse mechanical properties were not measured; therefore, the c-ring loads were based on the LT base mechanical properties. The stiffener web was coated with wax for one specimen loaded by each method in an attempt to localize cracking at the fillet that might result in separation of the stiffener. Specimens were exposed to a 3.5-percent NaCl solution by alternate immersion according to ASTM G44-88 for 75 days. Metallographic sections were prepared after exposure to examine corrosion morphology.

4. Results and Discussion

4.1. Microstructural Characterization

The microstructure of the 2090 near net shape extrusion was found to be predominantly unrecrystallized and elongated parallel to the extrusion axis, which is common for extruded Al-Li products (refs. 17 through 20). The unrecrystallized microstructure is a result of the ~9:1 extrusion ratio (the ratio of the cross-sectional area of the billet to extrusion) (refs. 17 and 21), which is lower than is typically found in commercial Al-Li extrusion practice (>20:1) (ref. 18). There were differences in grain morphology within the extruded section as a result of local variations in the extrusion aspect ratio (width to thickness of the extrusion). Texture analysis revealed that type and strength of texture components also varied throughout and confirmed a predominantly unrecrystallized microstructure, with small amounts of recrystallization in regions of higher aspect ratio.

4.1.1. Metallography. Optical macrographs of panels 2, 6, and 11 indicated that the grain morphology was similar for these three panels. Further metallographic examination was performed on panel 11 only. Triplanar micrographs of the skin and cap for panel 11 are shown in figures 3 and 4, respectively. The structures shown are typical, regardless of location along the length of the panel. Figure 3 reveals that a pancake-shaped grain morphology dominated the skin, which is similar to that of a rolled product (refs. 19 and 20). High aspect ratio (>20:1) extrusions would be expected to have a microstructure of pancake-shaped grains similar to a rolled product (ref. 19). Figure 4 shows that the grain morphology was fibrous in the cap, which corresponds to an extrusion

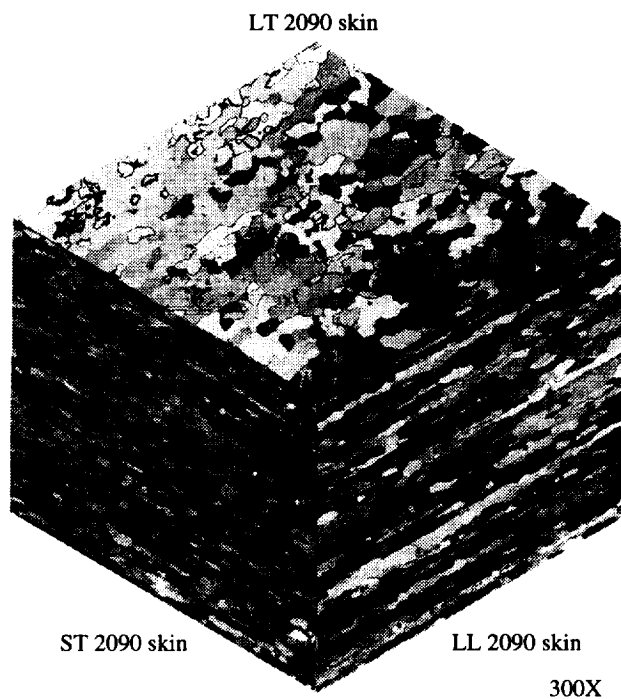


Figure 3. Triplanar optical micrograph of center of skin (anodized by using Barker's reagent and viewed under cross-polarized light).

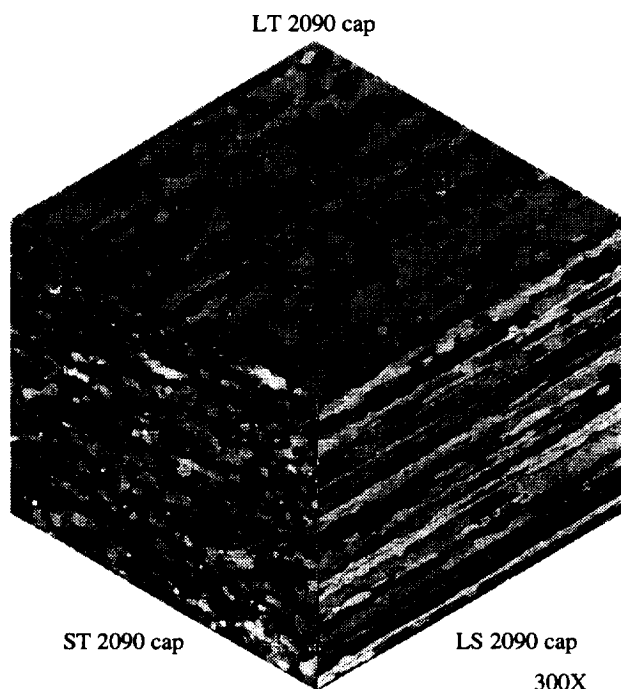


Figure 4. Triplanar optical micrograph of center of cap (anodized by using Barker's reagent and viewed under cross-polarized light).

formed at a low aspect ratio (refs. 17, 19, and 20). In an axisymmetric extrusion, where the aspect ratio is close to unity, the grain structure will be fibrous (ref. 19). In this study the lowest extrusion aspect ratios were found in the cap (~4:1), while the skin had an aspect ratio >25:1.

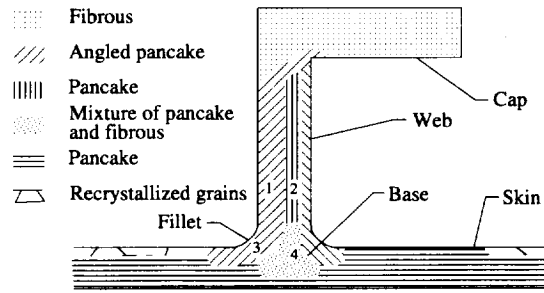
The typical variation in grain structure through the cross section is summarized in figure 5. On the stiffener side of the skin, large recrystallized grains were observed on the surface. These large grains were not observed under the cap or web of the stiffener. Their presence suggests local deformation during processing that was sufficient to promote recrystallization. This deformation presumably occurred during the rolling process to flatten the panels. Subsequent growth of recrystallized grains likely occurred during solution heat treatment and aging.

The complex microstructures in the web and the base are shown schematically in figure 5(a). Selected micrographs that illustrate the different grain structures within these areas are also included in figures 5(b) through (e). The microstructure in the web consisted of areas of pancake-shaped grains with distinct orientations. Pancake-shaped grains in the web were of lower aspect ratio than those found in the skin. (The extrusion aspect ratio of the web was approximately 6:1.) Adjacent to the surface of the web the grains were inclined in a manner corresponding to material flow during extrusion (fig. 5(b)). The core of the web contained an area of pancake-shaped grains oriented perpendicular to the skin (fig. 5(c)). The grains were offset from the midplane of the web nearer the cap side of the stiffener and had a lower aspect ratio in the TS plane than the inclined grains at the surfaces.

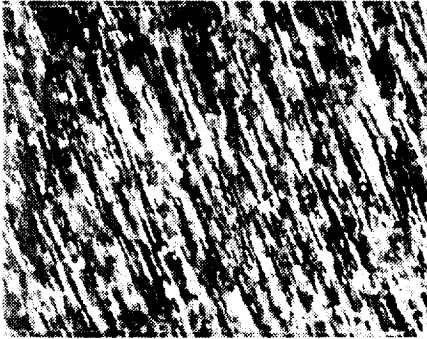
The microstructure in the base was comprised of a mixture of grain structures. The microstructure on the non-stiffened side was essentially the same as the majority of the skin. The material flow lines present in the grain structure followed the contours of the fillet at the junction of the web with the skin (fig. 5(d)). At the center of the base, the microstructure was similar to the cap and appeared fibrous (fig. 5(e)).

Specimens prepared by using Graff-Sargent reagent that were viewed under conventional bright field conditions had large stringers aligned in the direction of material flow. EDS and WDS analyses revealed that the stringers contained Al, Cu, and Fe and were likely AlCuFe constituent particles, which are commonly found in Al-Li alloys (refs. 22 and 23).

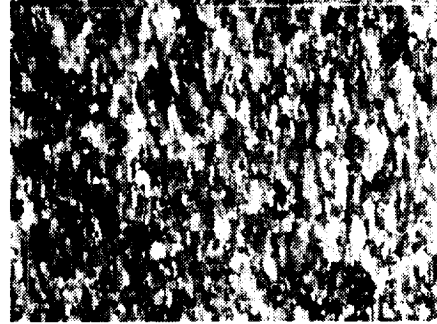
4.1.2. Texture analyses. The results obtained from preferred orientation measurements are shown in figures 6 through 9. Data are presented in the form of {111} pole figures and orientation distribution function (ODF) plots, which were constructed using the {111}, {200},



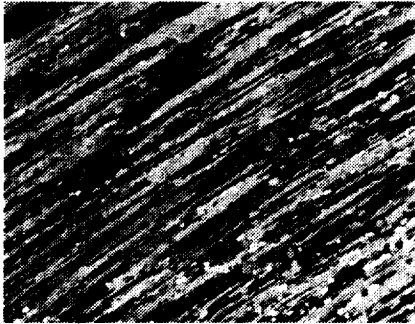
(a) Panel element schematic.



(b) Web, region 1.



(c) Web, region 2.



(d) Base, region 3.



(e) Base interior, region 4.

Figure 5. Skin-stiffener cross section showing microstructural variations resulting from extrusion process (anodized with Barker's reagent and viewed under cross-polarized light).

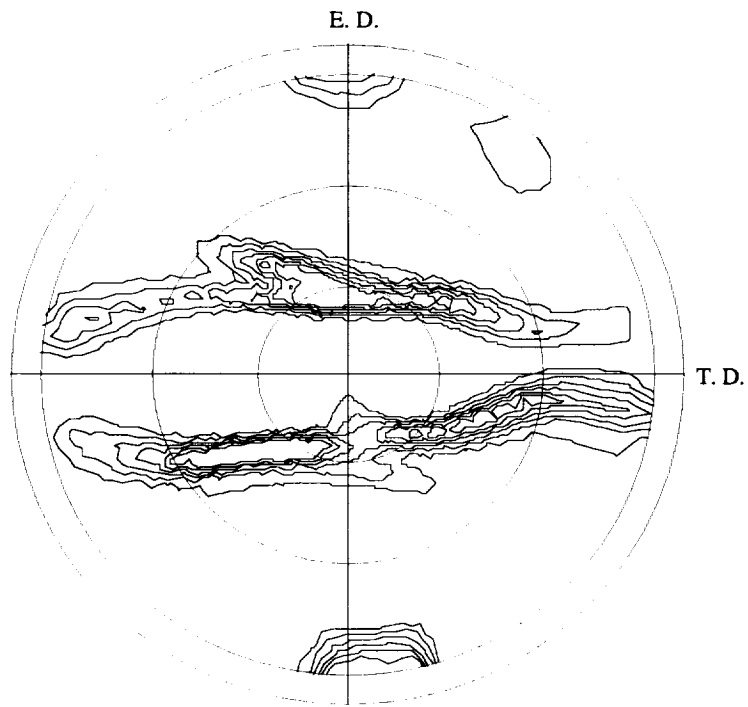
and $\{220\}$ partial pole figures. The ODF analyses were plotted following the Bunge notation with ϕ_2 sections held constant from 0° to 90° in multiples of 5° . Data were corrected by using measured background intensities and a calculated defocusing correction.

Cap: The $\{111\}$ pole figure and the ODF plot obtained from material in the midplane of the cap are shown in figure 6. These plots indicate that the texture was a combination of the fiber components present. Both the $\langle 111 \rangle$ and the $\langle 112 \rangle$ fiber components were observed, with the $\langle 111 \rangle$ fiber being predominant. The $\langle 111 \rangle$ fiber would be expected to increase yield strength

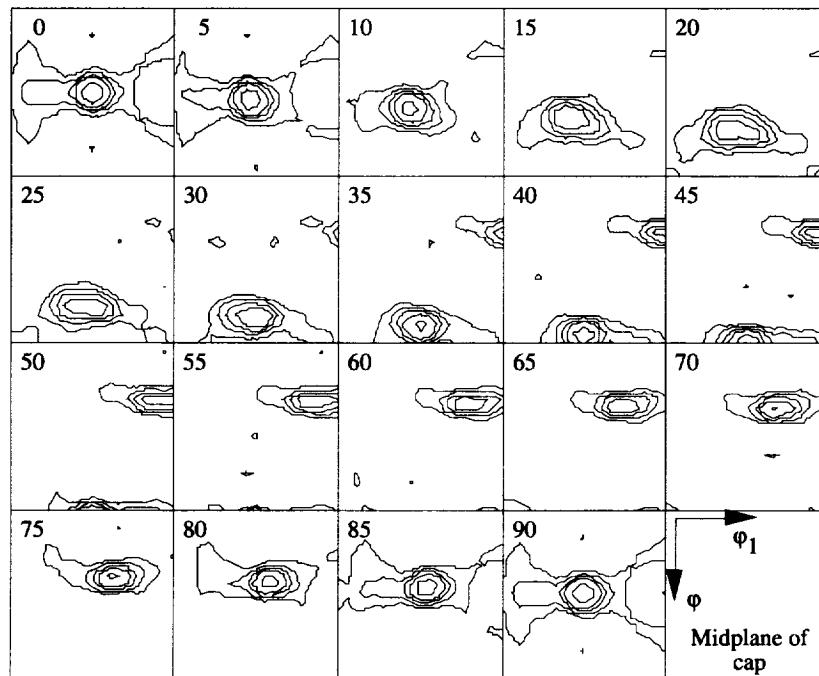
values to a greater extent than the $\langle 112 \rangle$ fiber (refs. 21 and 24).

Web: Texture samples for the web were taken from the region identified in figure 5(c). The texture was similar to an extruded tube and exhibited a well-developed $\langle 112 \rangle$ fiber component, as shown in figure 7. A small degree of recrystallization was observed from the texture data, which were identified from the Goss component, $\{001\} \langle 110 \rangle$.

Skin: The $\{111\}$ pole figure and the ODF plot obtained from material in the center of the skin are shown in figure 8. This figure indicates that the

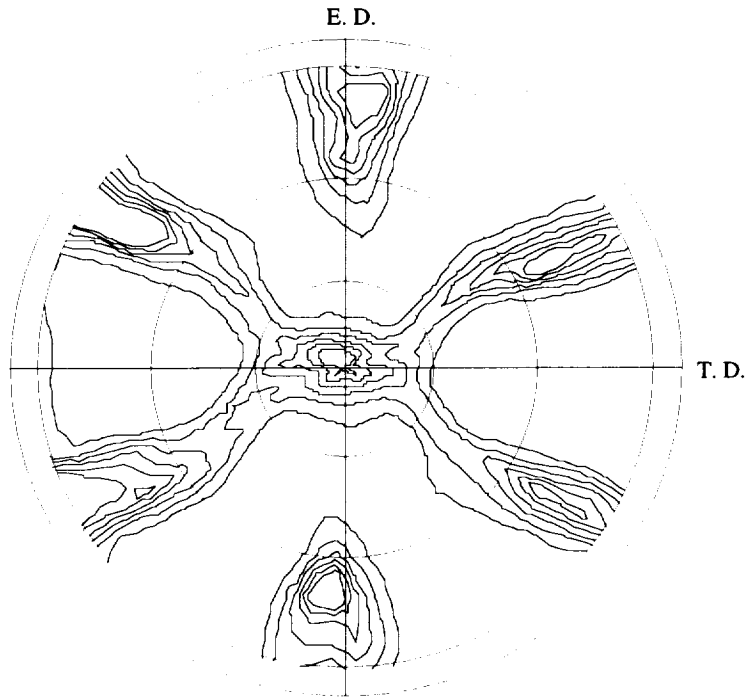


(a) {111} pole figure.

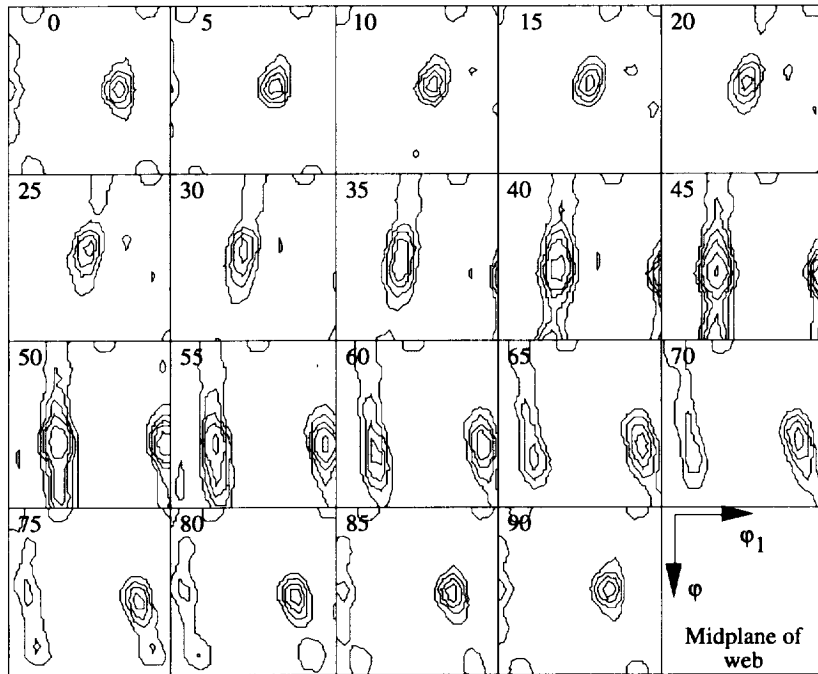


(b) ODF plot with constant ϕ_2 sections.

Figure 6. Texture results for midplane of cap.

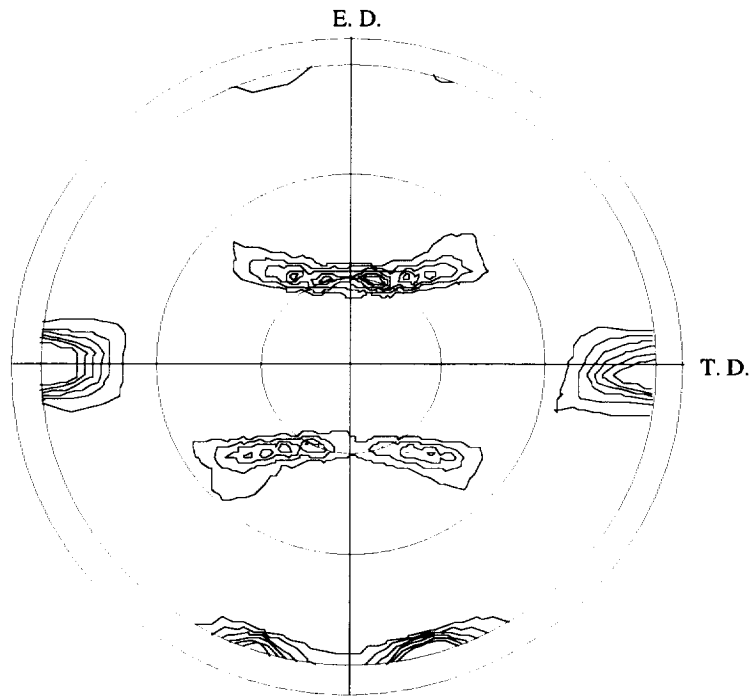


(a) {111} pole figure.

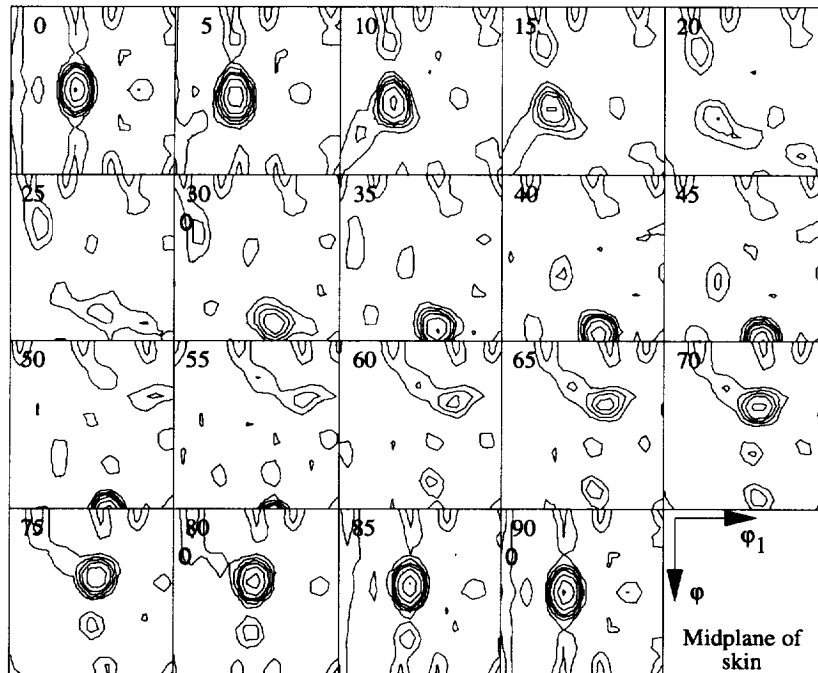


(b) ODF plot with constant ϕ_2 sections.

Figure 7. Texture results for midplane of web.

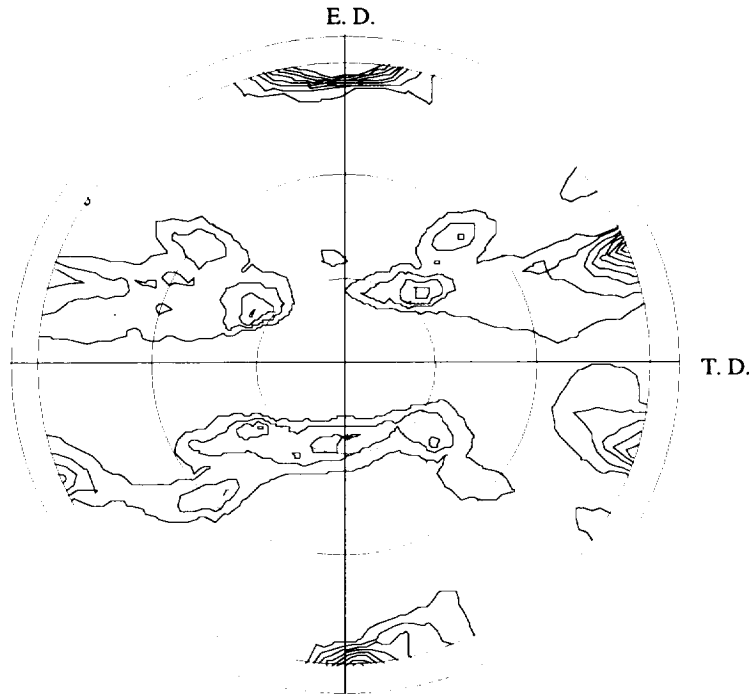


(a) {111} pole figure.

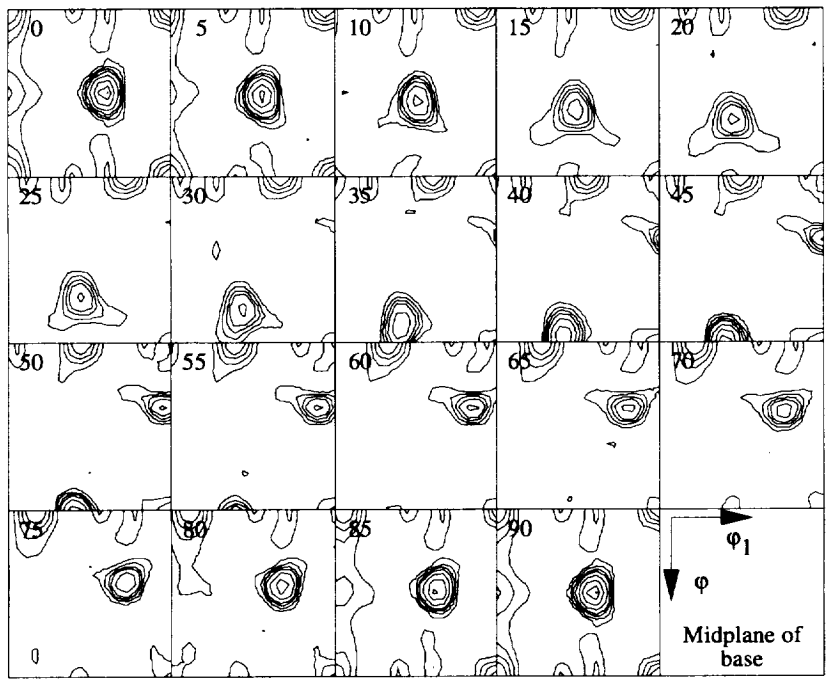


(b) ODF plot with constant ϕ_2 sections.

Figure 8. Texture results for midplane of skin.



(a) {111} pole figure.



(b) ODF plot with constant ϕ_2 sections.

Figure 9. Texture results for midplane of base.

microstructure was predominantly unrecrystallized and that the rolling component, Brass {110} <112>, had the highest intensity values. There were limited quantities of the recrystallization components, Cube {001} <100> and Goss, together with the <112> fiber texture found in the stiffener.

Base: The complex microstructure in this region, shown in figure 5(e), resulting from extrusion and rolling produced a range of textures, as shown in figure 9. The major component was the <111> fiber. The <001> fiber was observed to a lesser degree. There were also elements of the rolling component, Copper {112} <111>, together with some recrystallization (Goss component).

4.2. Tensile Properties

Complete tensile data obtained by each of the participating laboratories are shown in appendix C, tables C1 through C7. The tensile properties were obtained for the various panel elements to characterize the near net shape extrusion. In addition, tensile properties in the L and LT orientation were required to support calculation of fracture toughness. Pressure vessels, such as the ET, are proof tested to establish the maximum undetected flaw size in the wall of the vessel; therefore, adequate yield strength is required in the LT orientation to support the hoop stresses resulting from pressurization. Data for the LT base, the L skin, and the LT skin are discussed in terms of variation between panels, with location along the panel length, with position and orientation in panel elements, with temper, and with test temperature.

Panel-to-panel variation: Tensile data for four T86 (6-percent stretch) panels (1, 4, 6, and 11), tested at four different laboratories (Alcoa, Boeing Aerospace, LaRC, and MSFC), were evaluated to examine panel-to-panel

variation. The yield strengths and elongations to failure for the panels are shown in figure 10 and represent averages of all LT skin tests at 25°C on each panel. The yield strengths for panels 6 (LaRC) and 11 (MSFC) were similar, with average values within 5 percent of each other. The yield strength of panel 1 was about 10 percent below the average for panels 6 and 11; however, the result for panel 1 was from a single test. The yield strength for panel 4 was lowest, with the average (LaRC and Boeing Aerospace data) about 16 percent below the average for panels 6 and 11. Review of the processing parameters (table 1) for these panels could not explain the lower yield strength of panel 4, suggesting that these differences may be related to the post-extrusion processing (flattening). There was considerable variation in the elongation-to-failure data, with values over the range of ~2 percent to ~9 percent, making panel-to-panel comparisons difficult. Elongation-to-failure values differed substantially between laboratories for tests on the same panel where strength measurements were similar, for example, LaRC and MSFC data for panel 11. Some experimental error in the data may have been introduced because of the different techniques used to measure elongation to failure, as discussed in section 3.2; however, it is difficult to reconcile such large variations because all techniques were in accordance with ASTM specifications. The variation in average elongation may be related to the different numbers of specimens tested at the various laboratories.

Panel length variation: Data for panel 11 (from LaRC and MSFC) were reviewed to assess the variation in tensile properties along the length of the near net shape extruded panel. Room temperature yield strength and elongation to failure are shown in figure 11 and in appendix C, tables C4 and C5, for the L skin, the LT skin, and the LT base orientations measured at three panel locations. The data plotted in figure 11 represent averages of duplicate tests from LaRC and single tests from MSFC. The yield strength for each orientation decreased from the front to the back end of the panel, with the reduction ranging from 7 percent for the L skin to 14 percent for the LT base. This reduction may be associated with recovery processes due to billet heating during extrusion (ref. 17). Optical metallography of the microstructure at locations along the length of the panel did not indicate evidence of recrystallization. However, texture analyses at the midplane of the skin revealed the presence of recrystallization. The relative degree of recrystallization along the panel length was not determined. The data in figure 11 indicate that the room temperature elongation to failure increased from front to back for the LT skin but decreased for the L skin. The variation in elongation for the LT base was not as systematic, but there was an overall increase from front to back for both the LaRC and

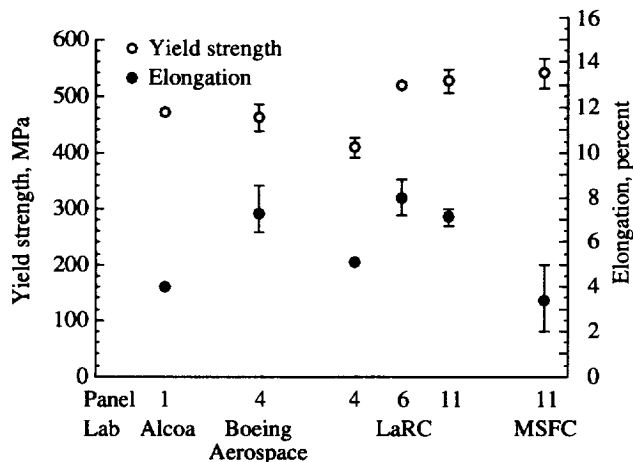


Figure 10. Panel-to-panel variation in yield strength and elongation to failure. Results for all LT skin tests at 25°C for each panel (bars represent range of data).

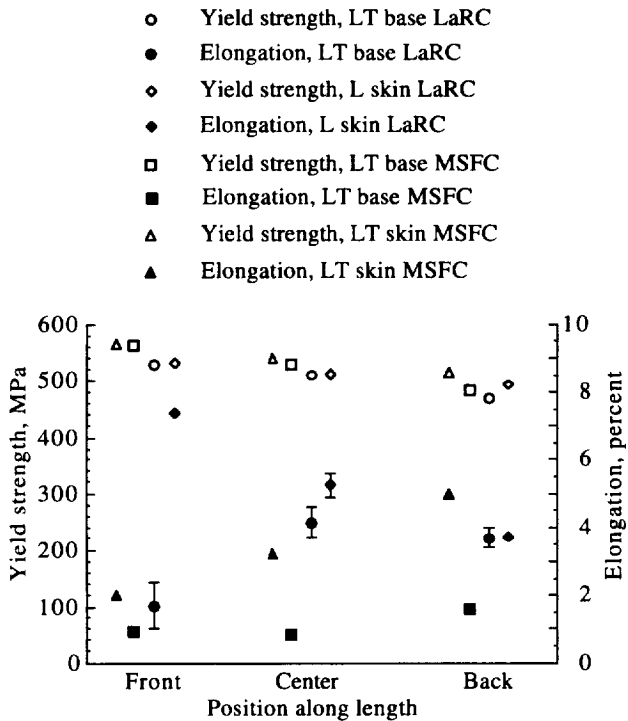


Figure 11. Variation in yield strength and elongation to failure along panel length. Results for panel 11 L skin, LT skin, and LT base at 25°C. Bars represent range of data.

MSFC data. The differences in LaRC and MSFC values may be related to the different methods used to measure elongation to failure.

MSFC data at -196°C and -253°C for the L skin, the LT skin, and the LT base for panel 11 (provided in appendix C, tables C6 and C7) also exhibit a similar reduction in yield strength from the front to the back end of the panel. Elongations to failure did not exhibit a clear trend from the front to the back of the panel in either the L or the LT orientations.

Stress-strain behavior: The variation in the stress-strain behavior at 25°C for the base, cap, and skin is shown by the curves in figure 12. The data shown are for panel 11 and are typical of the results obtained on other panels. Al-Li extrusions with axisymmetric shapes and a concomitant <111> fiber texture tend to have high yield strength and low elongation to failure, whereas extrusions of high aspect ratio, which exhibit rolling-type textures, tend to have lower strengths and higher elongations to failure (refs. 19 and 21). The present data for the 2090 extrusions tend to support these observations, and as figure 12 shows, the highest overall stress-strain curves are associated with areas of the extrusion that have low aspect ratio (cap and base), while areas of high aspect ratio have lower strength with the highest elongation to failure observed in the 45° skin. Where regions of

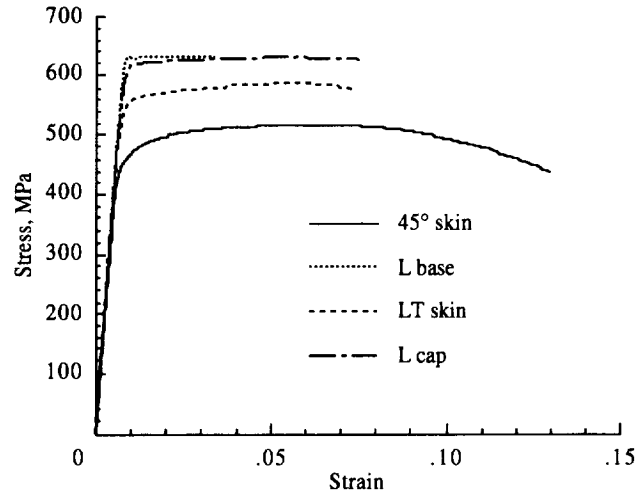


Figure 12. Variation in stress-strain behavior with respect to panel element and orientation. Individual tests at 25°C from center of panel 11.

mixed microstructure exist (base), the changes in grain structure (pancake-shaped to fibrous) appear to override textural differences, and the elongations to failure are more dependent upon grain alignment in the base-fillet region that results from grain flow during extrusion.

Panel element variation: Tensile yield strength and elongation to failure are plotted in figure 13 from LaRC data shown in appendix C, table C4, for several panel elements and orientations. The T86 data represent averages of room temperature tests for each panel element along the length of panel 11 and the front of panel 6. The T8E46 data represent averages of room temperature tests for each panel element at the middle of panel 2. Trends in yield strength for each panel element were the same for

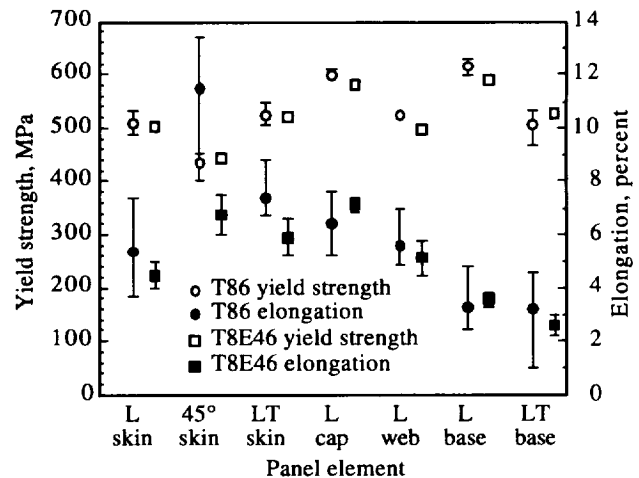


Figure 13. Variation in yield strength and elongation to failure with panel element. LaRC results for panels 6 and 11 (T86) and panel 2 (T8E46) at 25°C. Bars represent range of data.

the two tempers. Yield strengths were highest for the L base and the L cap and lowest for the 45° skin. The L and the LT skin, the L web, and the LT base had similar yield strengths. Both the L and the LT base had low elongation to failure, with values under 4 percent. Elongation to failure was highest for the 45° skin in the T86 temper and for the L cap in the T8E46 temper. The L cap, the web, the skin, and the LT skin had similar elongations to failure.

The yield strengths and elongations to failure could be directly related to the texture and grain morphologies in individual panel elements. The highest strengths were associated with regions of fibrous grains and the $\langle 111 \rangle$ fiber texture (cap and base). Lower strengths were associated with rolling type textures, the $\langle 112 \rangle$ fiber component (skin and web), and with pancake-shaped grain morphologies. The skin material exhibited the lowest strength and highest elongation to failure in the 45° orientation with similar strength and elongation to failure in the L and the LT orientations. These results are similar to other unrecrystallized Al-Li alloys in sheet and plate (refs. 25 through 27) and compare favorably with the expected behavior predicted by the texture data, discussed in section 4.1.2.

Aluminum alloy extrusions generally retain a mixture of $\langle 111 \rangle$ and $\langle 100 \rangle$ fiber textures when the extruded cross section is axisymmetric (aspect ratio ~1:1) (refs. 19 and 24). The yield strength of an axisymmetric extrusion of an Al-Li-Cu alloy (where most grains were oriented within 5° of the $\langle 111 \rangle$ fiber axis) was shown to be 27 percent higher than an extrusion with an aspect ratio of 8:1 (ref. 21). In the present study, the 2090 near net shape extrusion had an aspect ratio which varied from 4:1 to 25:1 and contained a number of texture components which were dependent upon position in the cross section. The room temperature tensile results obtained for panel 11 in appendix C, table C4, showed that the material in the skin, which had an aspect ratio of 25:1, typically had ~10 to 20 percent lower yield strength in the extruded direction than did the material in the cap and base, which had an aspect ratio of 4–6:1. Tempus, Scharf, and Calles (ref. 19) also observed that the tensile strength of extruded 8090 Al-Li alloy was reduced by ~10 percent when the aspect ratio was increased from 1:1 to ~7:1, with a corresponding transition from a fiber to a rolling texture.

Yield strength and elongation to failure for three panel elements (L skin, LT skin, and LT base) at 25°C, -196°C, and -253°C are shown in appendix C, tables C5 through C7. The variation in yield strength with temperature was the same for both the T86 (panel 11) and the T8E46 (panel 2) tempers. The average yield strengths increased with decreasing temperature for all elements,

and the relative strengths of the panel elements were the same at each temperature. Elongations to failure increased with decreasing temperature for the L skin and remained relatively constant for the LT orientations.

Effect of temper: Cold work typically improves the tensile properties of 2090 alloy by promoting a higher dislocation density and therefore more sites for nucleation of the strengthening precipitate, T_1 (Al_2CuLi), during aging (refs. 28 and 29). Therefore, the 6-percent stretch material (T86) should have higher yield strength than the 3-percent stretch material (T8E46). However, by using different aging practices, the near net shape extruded panels were aged to produce the same target mechanical properties; therefore, the properties should be similar, regardless of temper. The yield strengths at 25°C for the skin in the L, the LT, and the 45° orientations (fig. 13) were nearly identical for both stretch levels. The average yield strengths were slightly higher in the T86 condition for the L cap, the L web, and the L base than in the T8E46. The average yield strength was less in the T86 condition for the LT base; however, the T8E46 data fall within the range of the T86 data. An exception to these observations is reflected in the yield strength of panel 4 (T86), appendix C, tables C2 and C4, which was observed to be lower than the other 6-percent stretch panels (fig. 10), and was also less than the yield strength of panel 2 (T8E46), appendix C, tables C4 and C5. Elongation values for T86 and T8E46 overlap for every panel element except LT and 45° skin. As stated earlier and as illustrated in figure 13, panel element position has a greater effect on yield strength for the near net shape extruded panels than does the temper.

Comparisons with other alloys and product forms: The tensile properties for panel 11 were compared with published results for other 2090 Al-Li alloy products and 2219 Al alloy sheet and plate, as shown in appendix C, table C10 (refs. 11, and 30 through 34). Tensile data for the near net shape extruded panel included in table C10 represent averages of all tests performed at MSFC on panel skin for each orientation and temperature regardless of location along the panel length. Data for 2219 and 2090 plate are shown for comparison as the ET is integrally machined from thick plate. Data for a 2090 T-section extrusion is included for similar product comparison. Yield strength data plotted in figure 14 are averages of L and LT. The yield strength of the near net shape extruded panels was comparable to other 2090 products at room temperature and slightly lower at reduced temperatures, as shown in figure 14. The 2090 products were higher strength than 2219 at all temperatures, and the yield strengths increased by about the same amount with decreasing temperature. Values of elongation to failure shown in figure 15 are for the LT orientation only. The values for 2219 were higher than 2090

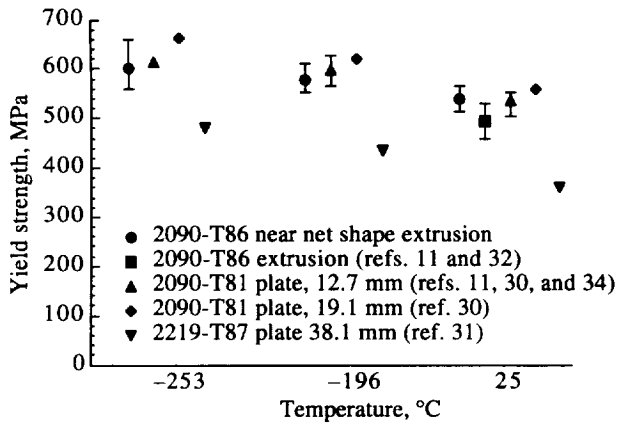


Figure 14. Variation in yield strength with temperature for various 2090 product forms and 2219 plate. Bars represent range of data.

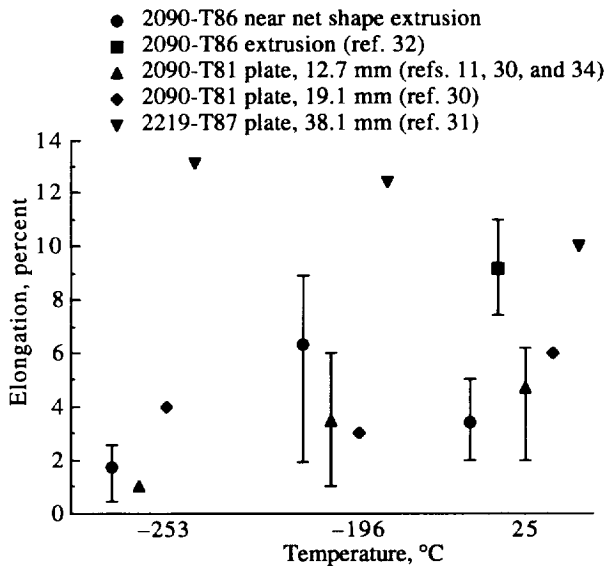


Figure 15. Variation in elongation to failure with temperature for various 2090 product forms and 2219 plate. Bars represent range of data.

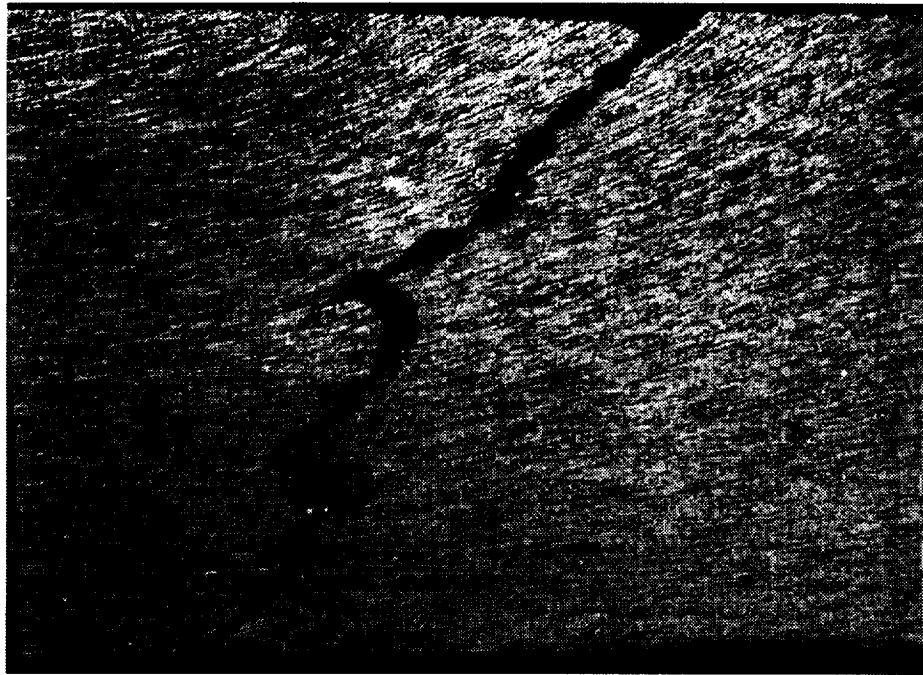
products at room temperature and increased with reduction in temperature. Elongation to failure for the 2090 products did not exhibit consistent trends with decreasing temperature. Transverse elongation for the near net shape extruded panel increased with reduction in temperature to -196°C , followed by a decrease with further reduction to -253°C . Data for the 19-mm plate exhibit the reverse trend, with a decrease in elongation to -196°C followed by an increase to -253°C . Data for the 12-mm plate decrease with each reduction in temperature. The combined data for the 2090 products represented, however, show a clear trend of decreasing elongation with reduction in temperature. The L orientation data shown in

appendix C, table C10, for the near net shape extruded panel and for the 1.6-mm sheet indicate a trend similar to the LT orientation for the near net shape extruded panel: an increase with reduction to -196°C , followed by a decrease with reduction to -253°C . Conversely, elongation in the L orientation for the 2090 plate products increased with decreasing temperature; however, the values were still below 2219 at each temperature. The data for a T8E46 extruded panel (panel 2), shown in appendix C, tables C5 through C7, indicate increased strength with reduction in temperature, while elongation first increased and then decreased. These data agree with the findings of Glazer et al. (ref. 35) for 2090-T8E41 plate.

Fractography: Fractographic examinations of tensile specimens were carried out at LaRC on specimens tested at 25°C by LaRC and at -196°C by Boeing Aerospace. Fractured tensile specimens were examined from the web and cap (L), from the base (L and LT), and from the skin (L, LT, and 45°). The macroscopic fracture was related to the grain morphology (grain shape and alignment), which varied with panel element as shown in figure 5. The microscopic mode of failure was predominantly by intersubgranular separation, regardless of test temperature or specimen position and orientation. Constituent particles, which were revealed in the metallographic studies, were occasionally observed on the fracture surfaces, although they did not play a dominant role in the fracture process.

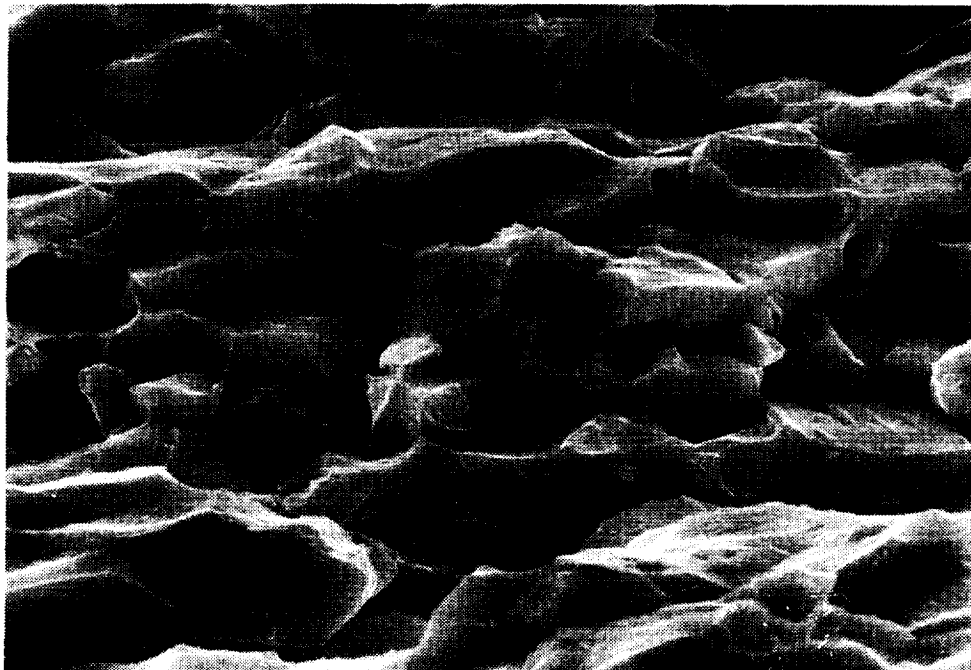
Tensile specimen fractography of the base in the L and LT orientations showed that macroscopic fracture was dependent upon grain orientation associated with material flow during extrusion. Figure 16 shows that the LT base specimens typically fractured at an angle to the tensile axis. The primary fracture tended to follow boundaries of pancake-shaped grains which were aligned with the fillet, as was shown in figure 5(d). Microscopically, failure was intersubgranular, as shown in figure 17. Fracture was more complex in the L base specimens and included an interior region of flat fracture and two areas of slant fracture. The flat fracture was associated with the region of mixed fibrous and pancake-shaped grains shown in figure 5(e), and the areas of slant fracture were associated with the pancake-shaped grains aligned in the fillet, figure 5(d). The strengthening contribution of the region of mixed fibrous and pancake-shaped grains resulted in higher yield strength in the L base than in the LT base (fig. 13). Elongations to failure were low for both orientations and were related to the grain boundaries approximately parallel to the critically resolved shear stress.

The tensile fracture of all skin specimens was by macroscopic shear. Grain boundary delamination was observed in specimens tested in the 45° orientation at



0.4 mm

Figure 16. Through-thickness cross section of tensile failure in base tested at 25°C in the LT orientation.



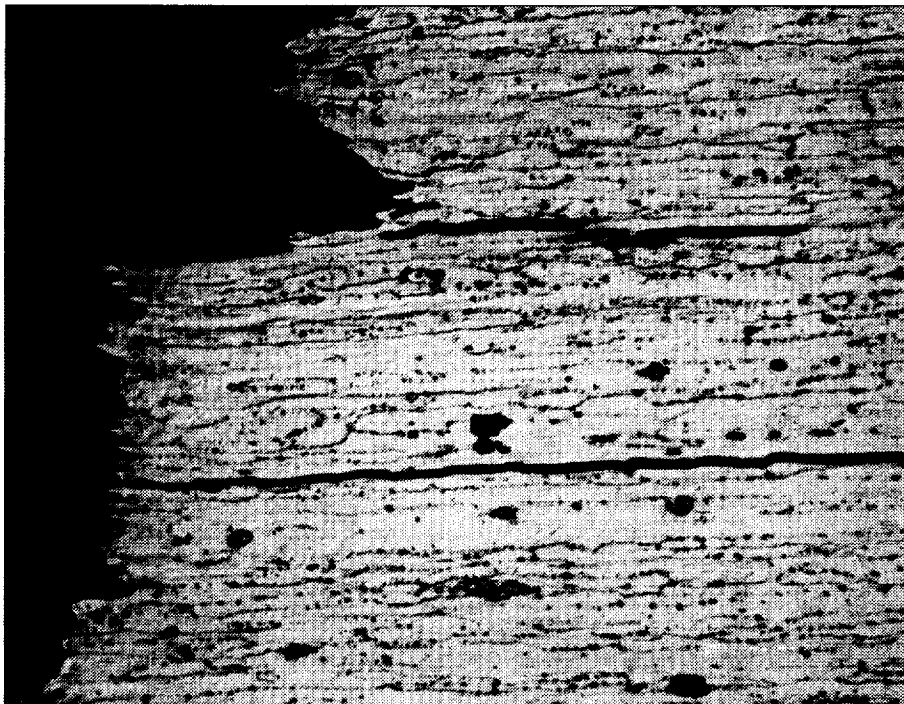
5 μ m

Figure 17. Typical intersubgranular tensile failure at 25°C showing pancake-shaped grains.



0.5 mm

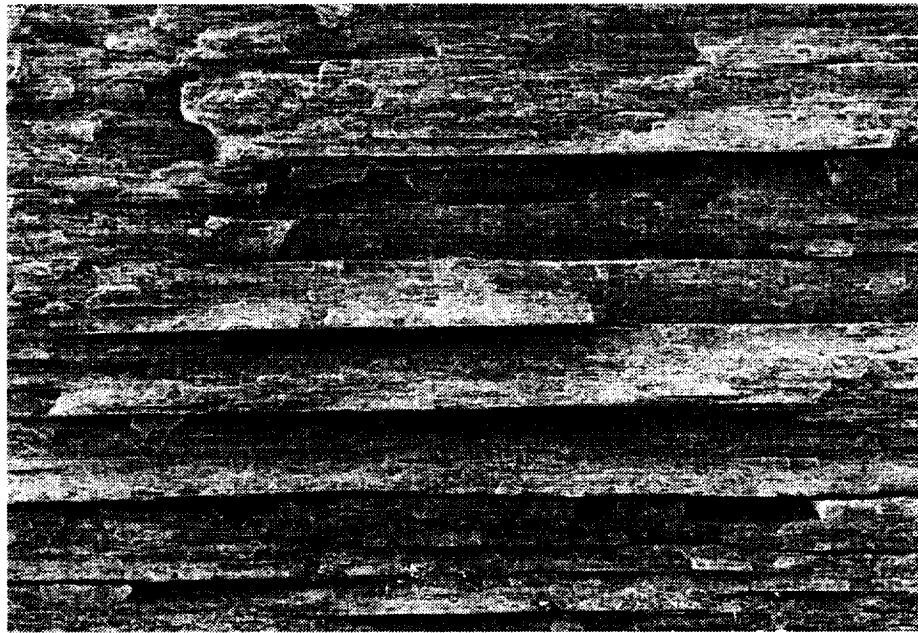
(a) Low-magnification micrograph showing steps caused by delamination.



25 μ m

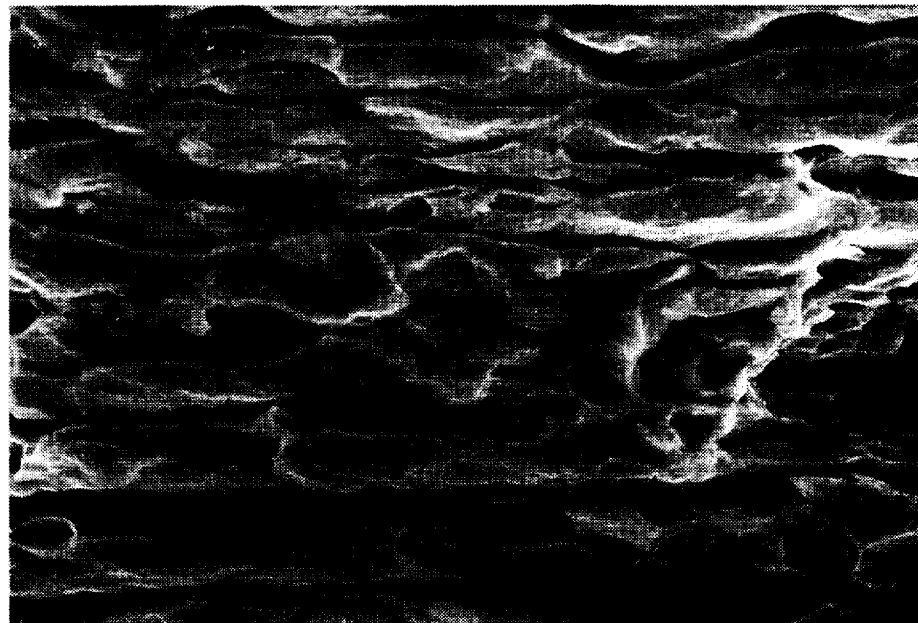
(b) High-magnification micrograph showing delamination along grain boundaries.

Figure 18. Typical tensile failure in skin tested at 25°C in 45° orientation.



1 mm

(a) Low-magnification fractograph showing extensive delamination.



5 μm

(b) High-magnification fractograph showing intersubgranular separation.

Figure 19. Typical tensile failure in skin tested at -196°C in LT orientation.

25°C, as shown in figure 18. Delamination was more evident in specimens tested at -196°C, as seen on the fracture surface shown in figure 19(a), than at 25°C, although only the LT orientation was examined. Consistent with room temperature and other panel element tests, intersubgranular separation was the predominant microscopic failure mode, as shown in figure 19(b). Other investigators (refs. 35 and 36) have observed similar fracture behavior in unrecrystallized 2090-T81 and in 2090-T8E41 plate.

4.3. Fracture Properties

As stated earlier, the ET is proof tested to determine the maximum undetected flaw size in the vessel wall. It is not economical to proof test the ET at the cryogenic use temperature; however, since the fracture toughness of 2219 increases at cryogenic temperatures, proof testing can be done at ambient temperature. To determine whether the fracture properties for the near net shape 2090 extrusion exhibited a trend of increasing toughness with decreasing temperature, fracture data were obtained at room and cryogenic temperatures. Fracture testing on the 2090 extrusion was carried out by using specimens containing either part-through surface cracks (to simulate a defect in the welded ET) or by using through cracks (to determine the extent of stable crack growth). Testing was performed to determine the effects of crack geometry, orientation, temperature, and temper on the fracture behavior of the near net shape extrusion and to enable comparison to be made with other 2090 product forms and conventional Al alloys.

4.3.1. Part-through surface crack tests. Surface crack data generated at Boeing Aerospace (panels 4 and 7) and NIST (panel 6) for extruded skin material are shown in appendix C, tables C9 and C10, respectively, and are summarized in table 4. Data from all tests performed were evaluated to identify trends in material performance regardless of the validity requirements of ASTM E740-88. The residual strength and toughness (K_{Ie}) were determined as a function of crack geometry, orientation, temperature, and temper.

Surface crack geometry: NIST examined the effect of crack geometry on toughness behavior with T-S orientation specimens by using two crack shapes, semielliptical and semicircular. As indicated in the notes of table 4, the crack geometries examined were such that a/c (the ratio of crack depth to half-surface crack length) was in the range of 0.28 to 0.38 for semielliptical and 0.72 to 0.94 for semicircular cracks. For the NIST fracture data (summarized in table 4), K_{Ie} values were overall highest for the semielliptical crack. The semielliptical crack showed a trend for increased residual strength and K_{Ie} with decreasing temperature, as shown for K_{Ie} in figure 20, whereas the data for the semicircular crack decreased from 25°C to -196°C with no further degradation from -196°C to -269°C. The data in table 4 also indicate that the residual strength and K_{Ie} values for 2090 alloy plate (ref. 37) were generally superior to the 2090 extrusion for a specimen containing a similarly shaped crack, that is, crack geometries c and d . The residual strengths and K_{Ie} values of the 2219 plate (ref. 38) were significantly higher than the 2090 extrusion, considering relative specimen widths (table 4

Table 4. Summary of Surface Crack (PS(T)) Fracture Results

Laboratory	Alloy/condition	W, mm	a/c	Temperature, °C	Orientation	Residual strength, MPa	K_{Ie} (MPa \sqrt{m})	
Boeing Aerospace	2090-T86 Panel 4 5-percent stretch	64	0.48-0.54 (semicircular)	25	T-S L-S	393.6 ± 6.9 383.7 ± 7.9	40.3 ± 0.1 38.4 ± 0.8	
				-196	T-S L-S	333.7 437.4 ± 7.2	33.8 43.5 ± 0.8	
	2090-T8E46 Panel 7 2.5-percent stretch			25	T-S L-S	373.0 337.1	37.9 33.2	
				-196	T-S L-S	192.3 406.8	19.2 40.7	
NIST	2090-T86 Panel 6 6-percent stretch	102	0.28-0.38 (semielliptical)	25 -196 -269	T-S T-S T-S	204.5 ± 17.5 244.0 ± 13.0 274.0 ± 7.0	31.2 ± 2.6 34.0 ± 1.3 37.6 ± 0.9	
		64	0.72-0.94 (semicircular)	25 -196 -269	T-S T-S T-S	366.5 ± 30.5 316.5 ± 29.5 322.0 ± 14.0	27.8 ± 4.2 23.1 ± 1.9 23.7 ± 0.9	
	Ref. 37	2090-T81	102	0.48-0.55 (semicircular)	25	T-S L-S	339.5 440.8	32.9 42.5
					-196	T-S L-S	405.7 514.5	40.0 50.3
Ref. 38	2219-T87	38.2	1.16-1.20 (semicircular)	25 -196	T-S T-S	435 521	79.8 100.1	

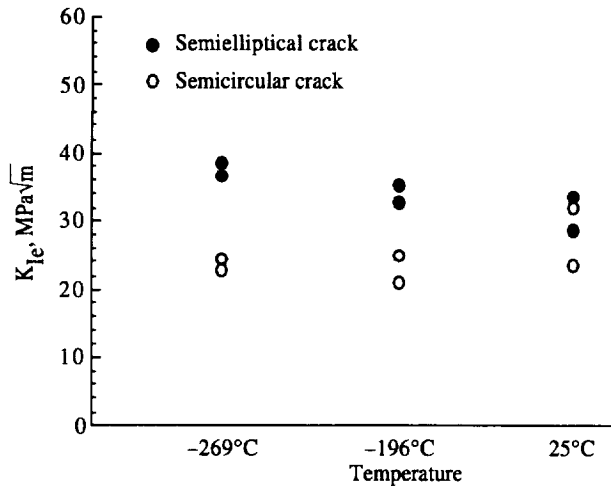


Figure 20. Effect of surface crack shape and temperature on toughness. Results for individual tests at NIST on panel 6 in T-S orientation.

notes). Similar observations have been made on 2.3- and 3.2-mm 2090-T81 plate, where residual strengths were found to be 6 percent less than 2219-T87 plate of the same thickness (ref. 38).

Orientation and temperature: Boeing Aerospace tested samples in the L-S and T-S orientations with semi-circular crack geometries. The data plotted in figure 21 show that for both 2090 tempers (T86 and T8E46), the L-S orientation was tougher than T-S at -196°C and that the T-S orientation was tougher than L-S at 25°C . Earlier tests (ref. 37) on similar specimens of 19.1-mm 2090-T81 plate machined to 3.2 mm showed that the toughness increased for both T-S and L-S orientations with a decrease in temperature, as shown in figure 21. This result would therefore imply that the reverse trend in the data at 25°C for the 2090 extrusion is related to extrusion or post-extrusion processing.

Temper: Boeing Aerospace examined the effect of temper on the toughness of the near net shape extrusion. The data plotted in figure 21 show that the T86 temper (6-percent stretch) was slightly tougher than the T8E46 temper (3-percent stretch) regardless of orientation or test temperature. Both T86 and T8E46 materials exhibit a reduction in the K_{Ic} value with decreasing temperature in the T-S orientation, as shown in table 4 and in figure 21. The reason for the loss in toughness in the T-S orientation is unclear; however, it is probably related to processing because the mechanical properties of Al-Li alloys typically improve with increasing amounts of preaging stretch (refs. 18, 29, and 39).

Fractography: LaRC carried out fractographic examinations on the T86 part-through surface crack (PS(T)) specimens from panel 4 tested at Boeing

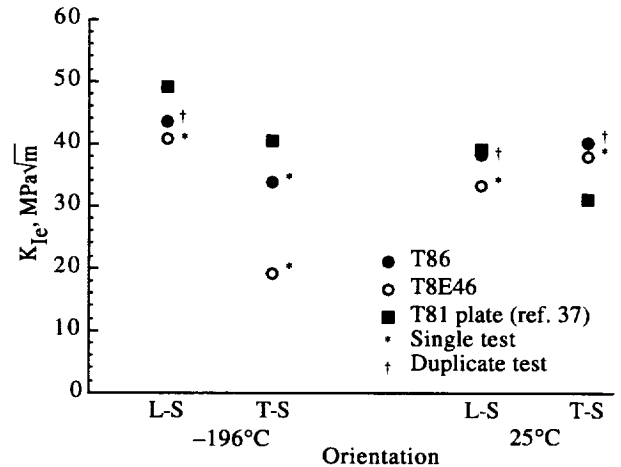
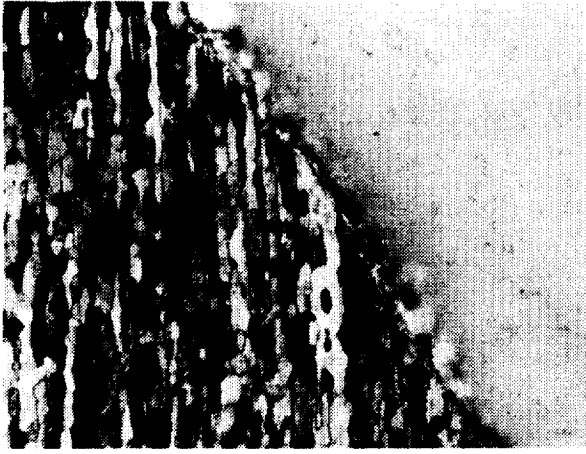


Figure 21. Comparison of surface crack test results from Boeing Aerospace for 2090 extrusions with 2090 plate.

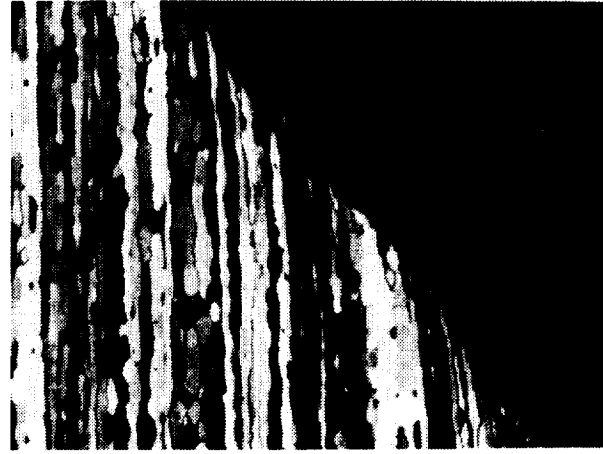
Aerospace. Photomicrographs of through-thickness fractured sections, examined by using polarized light, are shown in figure 22. These micrographs indicate that the specimens tested at 25°C in both the L-S and the T-S orientations had slant fracture, while those tested at -196°C exhibit flat fracture. This phenomenon has been observed by other workers (refs. 40 and 41) and has been attributed to a change in the stress state in the test sample as the temperature decreases.

The electron micrographs shown in figures 23 through 26 display features of the order of subgrain size, which indicate that microscopically, failure occurred by intersubgranular separation for both L-S and T-S orientations at 25°C and -196°C . Similar observations have been made on 2090-T8E41 plate (ref. 36) where it was noted that failure mode was unchanged with test temperature over the range 25°C to -269°C . Macroscopically, grain boundary delaminations were observed only in specimens tested at -196°C and were more evident in the L-S specimens (fig. 25) than the T-S specimens (fig. 26). Grain boundary delamination was not observed during fracture at 25°C . Increases in the fracture toughness of Al-Li alloys with decreasing temperature have been attributed in part to the process of delamination toughening, which results from the splitting of grain boundaries as the crack tip advances (refs. 40 and 41). While delaminations were present on the fracture surfaces of specimens tested at -196°C , the delaminations were not sufficiently deep or numerous enough to explain the differences in the toughness values with temperature.

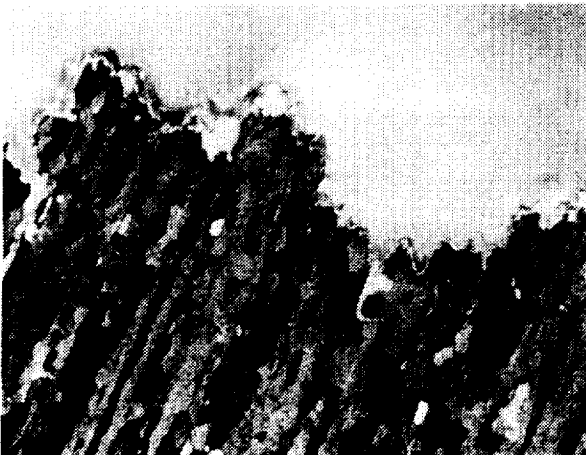
4.3.2. Through-crack fracture tests. Results from middle-cracked tension (M(T)) specimens machined from skin material panels 11 and 2 and tested at LaRC are presented in the form of R-curves in figures 27



(a) T-S specimen tested at 25°C.



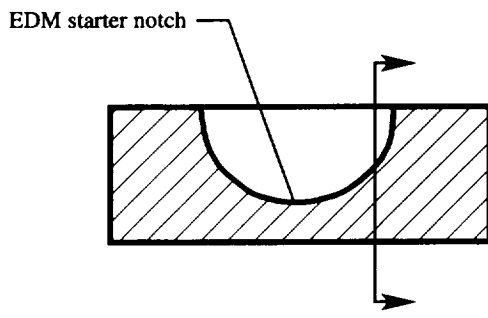
(b) L-S specimen tested at 25°C.



(c) T-S specimen tested at -196°C.

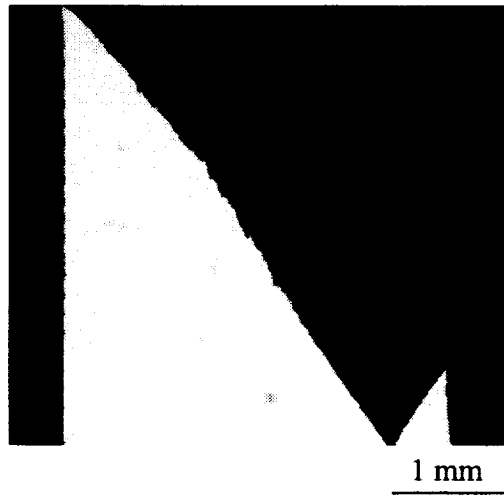


(d) L-S specimen tested at -196°C.

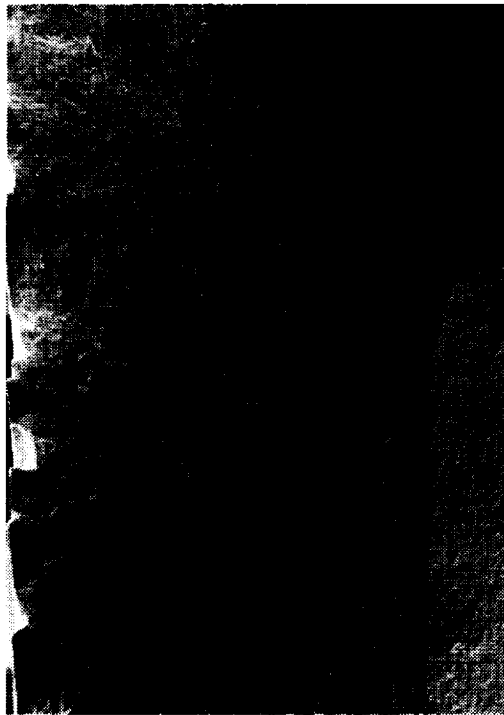


(e) Schematic of PS(T) fracture surface showing location of cross sections.

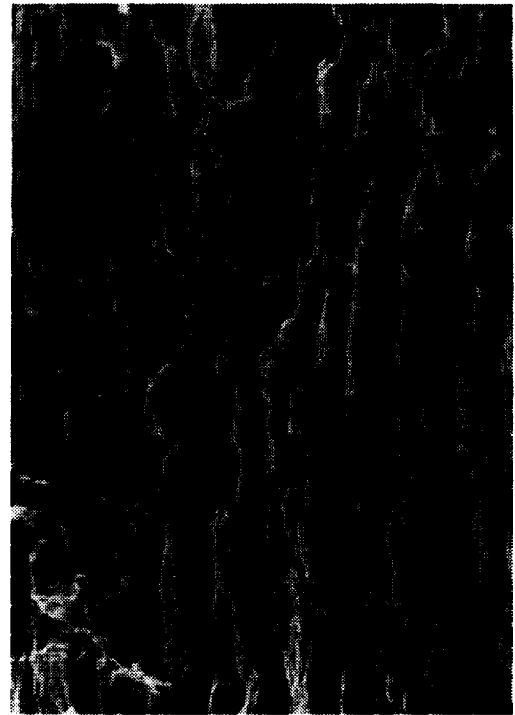
Figure 22. Through-thickness cross sections of 2090 PS(T) fracture specimens (anodized with Barker's reagent and viewed under cross-polarized light).



(a) Through-thickness cross section.

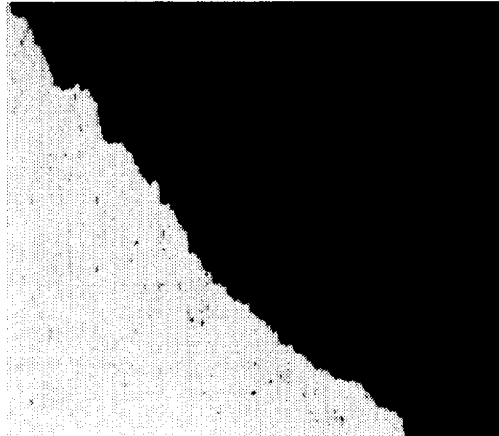


(b) Top view of cross section.



(c) Area in center of figure 23(b).

Figure 23. Fracture surface of PS(T) specimen in L-S orientation at 25°C.



500 μm

(a) Through-thickness cross section.



500 μm

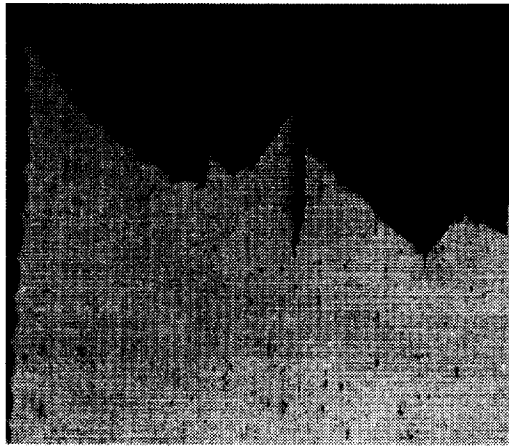
(b) Top view of cross section.



20 μm

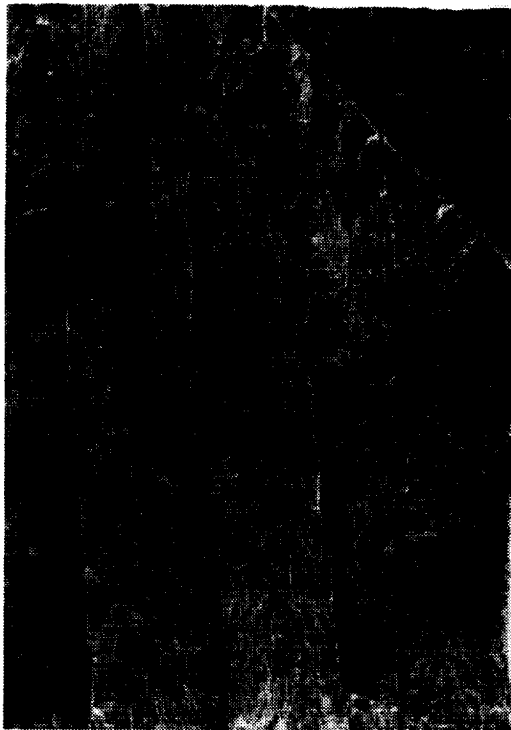
(c) Area in center of figure 24(b).

Figure 24. Fracture surface of PS(T) specimen in T-S orientation at 25°C.



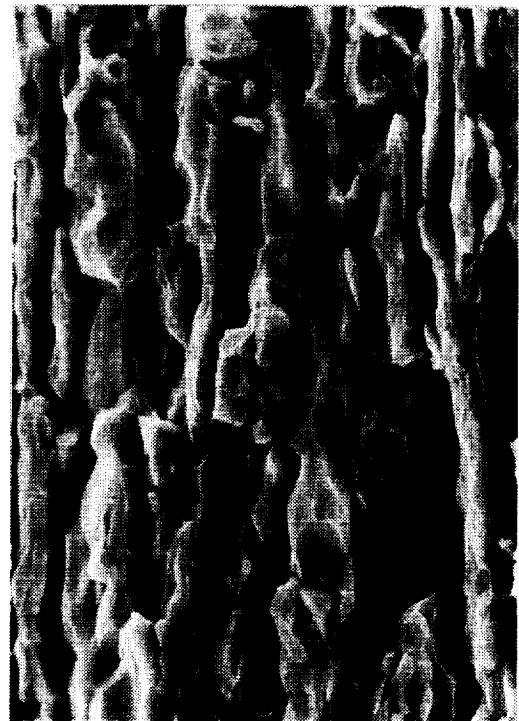
500 μm

(a) Through-thickness cross section.



500 μm

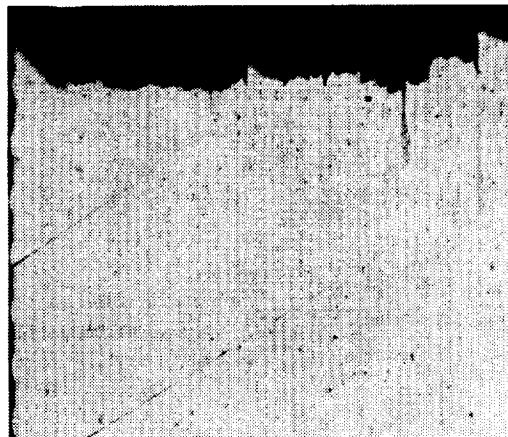
(b) Top view of cross section.



20 μm

(c) Area in center of figure 25(b).

Figure 25. Fracture surface of PS(T) specimen in L-S orientation at -196°C .



500 μm

(a) Through-thickness cross section.



500 μm

(b) Top view of cross section.



20 μm

(c) Area in center of figure 26(b).

Figure 26. Fracture surface of PS(T) specimen in T-S orientation at -196°C .

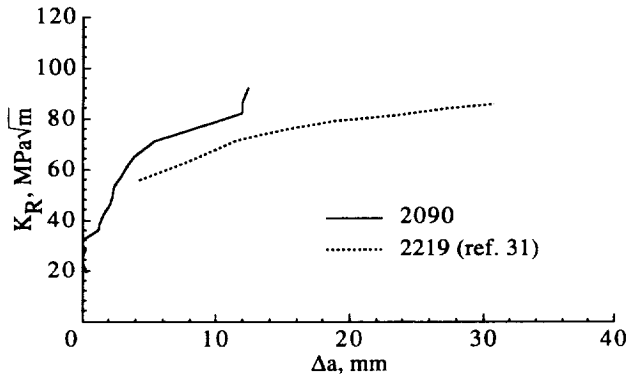


Figure 27. Comparison of the resistance to stable tearing of 2090-T86 extrusion with 2219-T87 plate in L-T orientation at 25°C. Data from M(T) specimens.

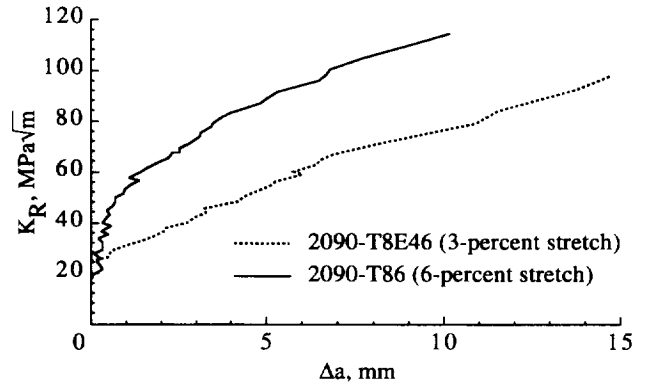


Figure 30. Effect of stretch on fracture behavior of 2090 extrusion in L-T orientation at 25°C. Data from M(T) specimens.

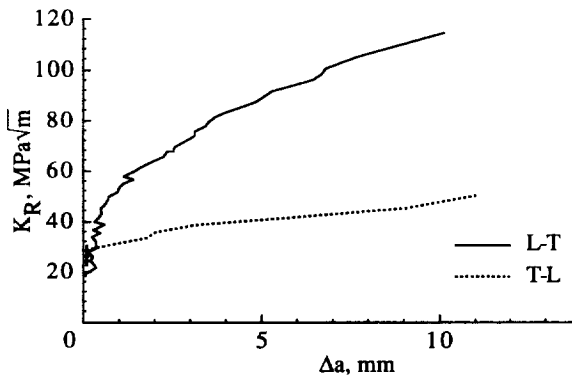


Figure 28. Effect of orientation on fracture behavior of 2090-T86 extrusion at 25°C. Data from M(T) specimens.

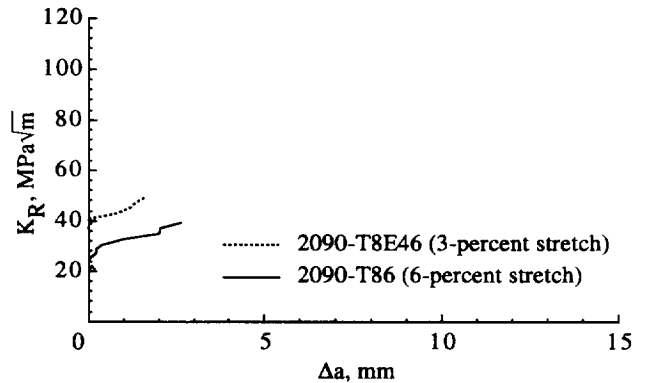


Figure 31. Effect of stretch on fracture behavior of 2090 extrusion in T-L orientation at 25°C. Data from M(T) specimens.

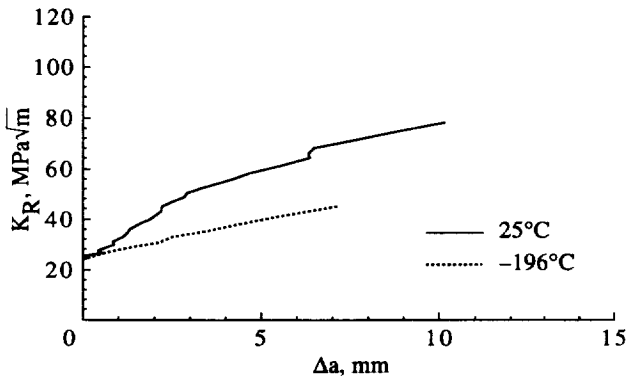


Figure 29. Effect of temperature on fracture behavior of 2090-T8E46 extrusion in L-T orientation. Data from M(T) specimens.

through 31. The width of the specimens was insufficient to maintain elastic conditions at all values of the applied load, and the net section stress exceeded yield; hence, the tests do not meet the requirements of ASTM E561-86 and are invalid. Furthermore, because of the overall wav-

iness in the specimens, crack length determination with the compliance technique was difficult. Therefore, only a limited number of tests have been completed. Alternative specimen designs and techniques for crack length measurement are currently being explored to overcome this problem. A comparison between the R-curves obtained for the 2090 extrusion and the 2219-T87 (ref. 31) plate, machined down to the same thickness, is shown in figure 27. The R-curves are plotted as a function of orientation, temper, and temperature in figures 28 through 31.

Orientation: The variation in stable tearing with orientation is illustrated in figure 28 for the T86 material, tested at 25°C. The R-curves indicate that the resistance to stable tearing is higher in the L-T orientation than in the T-L orientation. The material in the skin is predominantly unrecrystallized, as shown by the texture data. R-curve tests on other unrecrystallized Al-Li alloys have exhibited a similar trend with orientation (refs. 26 and 27) in that the toughness of rectangular and T-section extrusions was approximately halved in the

T-L orientation when compared with the L-T orientation at 25°C. Therefore, the loss in toughness in the T-L orientation in the present study is likely a result of the effects of preferred orientation resulting from the unrecrystallized grain structure.

Temper: The effect of the T86 temper (6-percent stretch) and the T8E46 temper (3-percent stretch) on R-curve behavior was determined at 25°C in both the L-T and T-L orientations. As shown in figure 30, the R-curve in the L-T orientation is higher for the T86 material. The data in figure 31 indicate the opposite trend for the T-L orientation, although only limited data from one test in each orientation are available. Other investigators have observed a similar trend in the fracture toughness of Al-Li alloys in the T8X temper with orientation (refs. 26 and 42).

Temperature: One test has been completed to date at -196°C. The test was on T8E46 material in the L-T orientation and is shown for comparison with a 25°C test in figure 29. A drop in the resistance to stable tearing was observed with decreasing temperature from 25°C to -196°C. However, this is not typical behavior for 2090 alloy in sheet and plate form, which would be an expected increase in crack growth resistance; therefore, no attempt has been made to draw conclusions from one data set.

Fractography: The fracture surfaces of the T8E46 material (panel 2) were examined after testing in the L-T orientation at 25°C and -196°C. The fractography of the M(T) specimens was very similar to the PS(T) specimens described earlier. Optical microscopy revealed large shear lips and slant fracture at 25°C and flat fracture at -196°C. The scanning electron micrographs of the fracture surfaces, taken close to the fatigue crack where stable crack growth would be expected to occur, are shown in figures 32 and 33. The fractographs indicate that failure occurred by intersubgranular separation at both temperatures. The figures also show that grain boundary delamination was absent in the specimen tested at 25°C; however, minor delaminations were present at -196°C. Constituent particles were not observed on the fracture specimen surfaces.

4.4. Welding

Based on visual appearance of the welded sections, Boeing Aerospace found no observable difference between welded specimens of 2090 sheet, used for weld schedule development, and the near net shape extrusion of equal thickness. Boeing Aerospace used a single pass weld schedule on both the sheet and extrusion, as shown in table 3. The weldments were inspected to the requirements of MSFC-SPEC-504C with respect to surface and internal defects and were found acceptable.

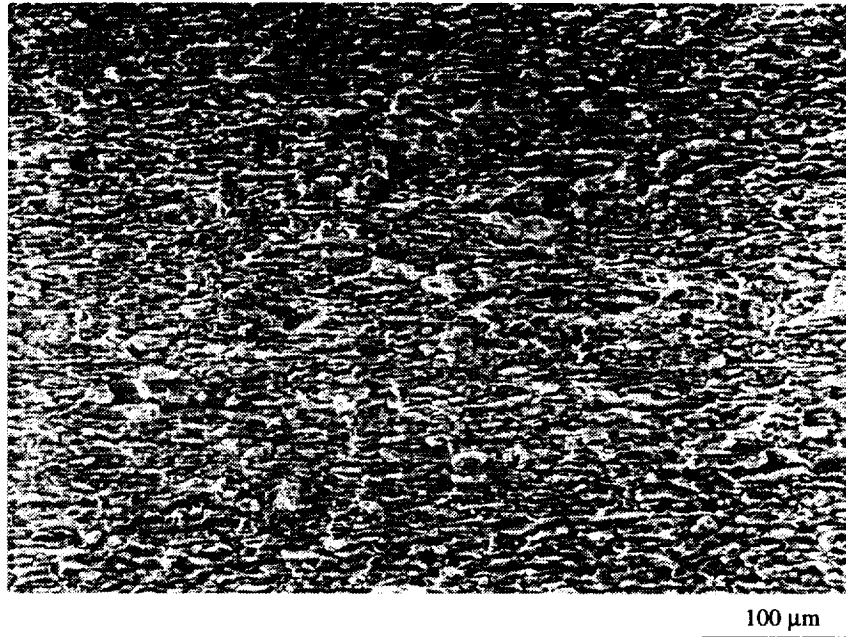
MSFC noted that much less heat input (15 amps) was required to produce an acceptable weld on the 2090 alloy extrusion when compared with another Al-Li alloy, 2095. A cover pass, as shown in table 3, was required due to undercut in some sections of the weld. Radiographic examination of the welds revealed some scattered microporosity along the weld toes; however, the welds were acceptable per specification, MSFC-SPEC-504C.

4.4.1. Weldment tensile properties. Weldment tensile properties at 25°C and -196°C for 2090 extrusions welded by Boeing Aerospace are compared to 2090-T81 plate and 2219-T87 sheet (ref. 31) in table 5. The 2090 extrusion data represent properties averaged for four T86 welded panels and for one T8E46 welded panel, with complete data shown in appendix C, table C11. For both orientations, weldments exhibited higher yield and ultimate strengths at -196°C than at 25°C. At both temperatures, weldments of 2090-T8E46 extrusion had the highest yield and ultimate strengths of all the product forms compared. At 25°C the 2090-T86 extrusions had a higher ultimate strength than the 2090-T81 plate or 2219-T87 sheet. At -196°C, the 2090-T86 extrusion had a higher ultimate strength than the 2090-T81 plate and a slightly lower ultimate strength than 2219-T87 sheet.

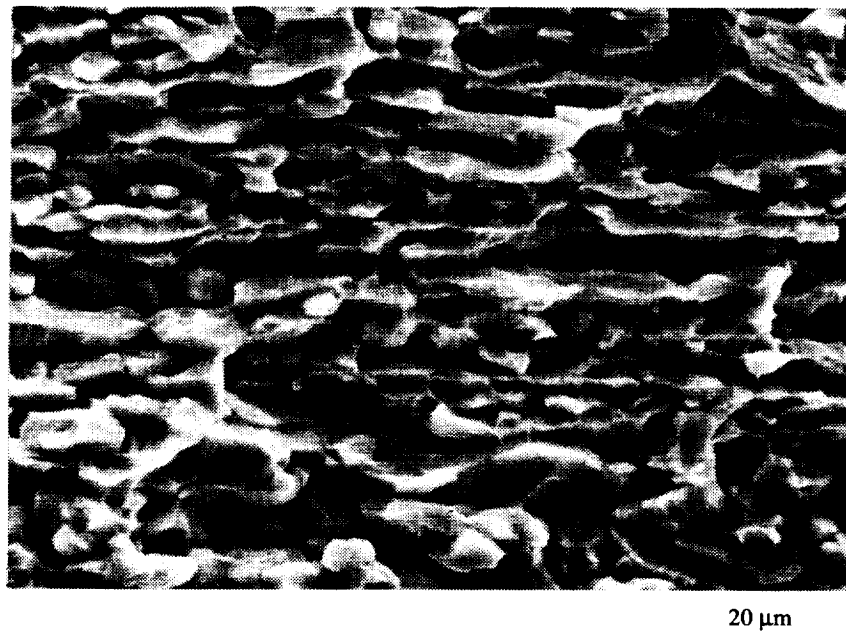
Boeing Aerospace observed that failure of the welds of the 2090 extrusion occurred in the heat-affected zone (HAZ) of the weld. The reduction in properties in the HAZ compared to the parent metal was overaging and softening that resulted from thermal cycling during welding (ref. 43).

4.4.2. Weldment fracture properties. The 2090 near net shape extrusion weld metal fracture data, generated by Boeing Aerospace and NIST, are summarized in table 6 and shown in detail in appendix C, tables C12 and C13. Data for welded 2090-T81 plate and 2219-T87 sheet are also shown in table 6. All surface crack tests were invalid according to ASTM E740-88, as indicated in tables C12 and C13. All specimens were tested with the surface crack positioned in the fusion zone of the weldments. The mechanical properties in the fusion zone are not related to those of the worked skin material because the melting and solidification during welding removes any effect of prior processing. Therefore, no difference in fracture data was expected or observed for comparable crack geometries, with respect to product form, stretch, or orientation.

Boeing Aerospace reported that the fracture toughness of both the 2090 plate and the extrusion weldments were similar (ref. 37). The residual strength and K_{Ic} increased for both the extrusion and the sheet weldments at -196°C when compared with 25°C. Again, there

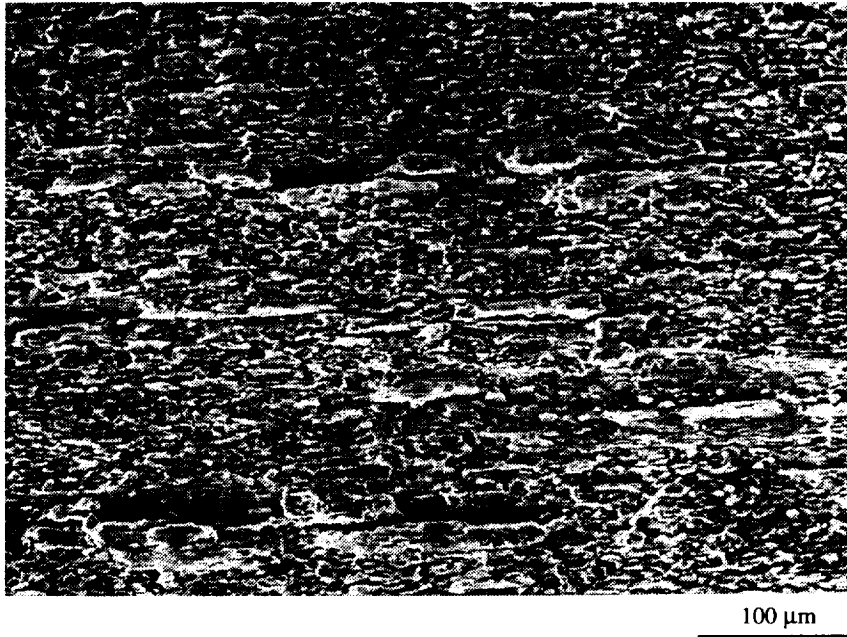


(a) Low-magnification micrograph of fracture surface.

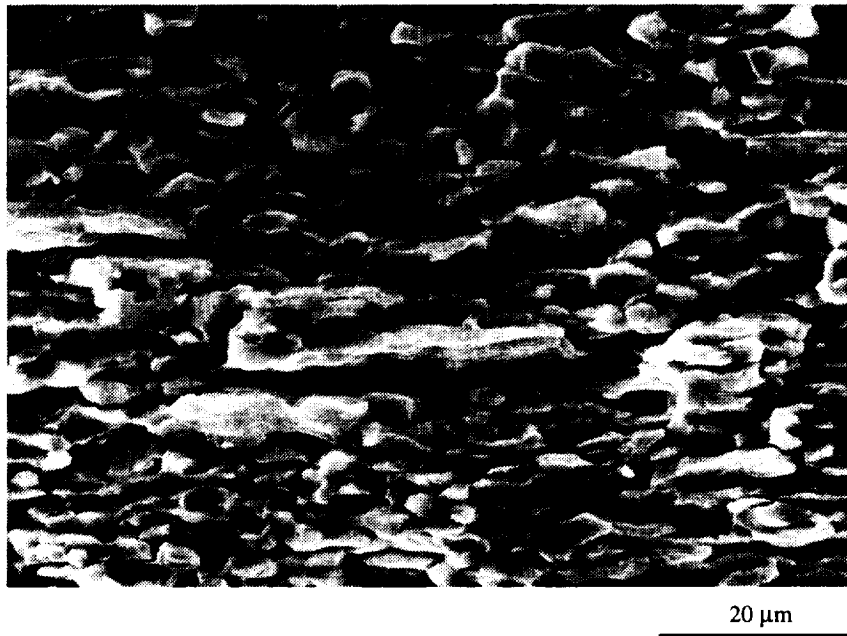


(b) High-magnification micrograph showing intersubgranular separation.

Figure 32. SEM fractography of 2090-T8E46 extrusion M(T) specimens tested at 25°C in L-T orientation.



(a) Low-magnification micrograph of fracture surface and grain boundary delamination.



(b) High-magnification micrograph showing intersubgranular separation.

Figure 33. SEM fractography of 2090-T8E46 extrusion M(T) specimens tested at -196°C in L-T orientation.

Table 5. Summary of Tensile Properties of Welded 2090 and 2219 Alloys

Alloy/condition	Product form	Welding process	Orientation	25°C		-196°C	
				S_y (MPa)	S_u (MPa)	S_y (MPa)	S_u (MPa)
2090-T86	Extrusion	VPPA	L	196.5	296.4	206.8	358.5
			LT	175.2	313.4	222.7	368.0
2090-T8E46	Extrusion	VPPA	L	219.1	337.6	270.9	413.3
2090-T81 (ref. 37)	Plate	VPPA	L	156.8	296.8	205.8	377.8
			LT	171.1	286.6	198.9	332.3
2219-T87 (ref. 31)	Sheet	GTA		195.1	279.2	218.5	376.4

Table 6. Summary of Weldment Surface Crack (PS(T)) Fracture Results

Laboratory	Alloy/condition	W, mm	<i>a/c</i>	Temperature, °C	Orientation	Residual strength, MPa	K_{Ic} (MPa \sqrt{m})	
Boeing Aerospace (VPPA)	2090-T86 Panel 4 5-percent stretch	102	0.42-0.46 (semicircular)	25	T-S L-S	218.2 ± 1.0 212.7 ± 2.4	21.5 ± 0 20.3 ± 0.3	
				-196	T-S L-S	245.4 ± 1.4 230.3 ± 15.9	24.4 ± 0.8 22.4 ± 1.3	
	25			T-S	213.7	21.8		
	-196			T-S	248.2	24.7		
NIST (VPPA)	2090-T86 Panel 6 6-percent stretch	64	0.26-0.32 (semielliptical)	25	T-S	176.0 ± 15.0	24.1 ± 0.6	
		64	0.72-0.94 (semicircular)	-269	T-S	208.0	27.0	
					25	T-S	207.5 ± 8.5	14.3 ± 0.4
					-269	T-S	252.5 ± 4.5	19.2 ± 0.4
Ref. 37 (VPPA)	2090-T81	102	0.42-0.46 (semicircular)	25	T-S L-S	204.6 210.1	20.8 20.9	
				-196	T-S L-S	241.3 238.3	23.0 24.4	
				25		209.6	34.0	
				-196		237.2	40.0	
Ref. 31 (GTA)	2219-T87	95	0.26-0.27 (semielliptical)	-269		256.5	39.0	

was no effect of either stretch for the extrusions, or of orientation for the extrusions or plate, on the toughness reported by Boeing Aerospace.

As shown in table 6, weldments tested by NIST exhibited an increase in toughness for both the semicircular and semielliptical cracks with decreasing temperatures from 25°C to -269°C. Residual strengths for the semielliptical crack were slightly lower than for the semicircular crack at both 25°C and -269°C. Toughness values were higher for the semielliptical crack at both temperatures; however, the calculated fracture toughness values were not valid according to ASTM E740-88, as general yielding occurred at 25°C, and stable crack growth was observed at -269°C. Macroscopically, specimens fractured at 25°C had large shear lips, while those tested at -269°C exhibited flat fracture. Under microscopic examination, there was a transition from dimpled rupture at 25°C to intergranular fracture at -269°C.

In general, the residual strength values for the extrusion weldments generated by Boeing Aerospace and

NIST compare well with data for gas tungsten arc (GTA) welded 2219-T87 (ref. 31), as shown in table 6. However, the K_{Ic} values for the 2219-T87 weldments are nearly twice those of the 2090 near net extrusions.

4.5. Corrosion

Corrosion resistance is highest for 2090 in peak-aged tempers and is maintained with either slight underaging or slight overaging (near peak-aged) (refs. 11, 14, 44, and 45). However, corrosion resistance is greatly reduced with severe underaging (refs. 44 and 46) or overaging (ref. 47). The 2090 near net shape extrusions exhibited comparable exfoliation and stress corrosion resistance to peak and near peak-aged 2090 plate, sheet, and extruded products. Complete tabulated test data for panel 6 are included in appendix C, tables C14 through C17. The corrosion tests were for screening purposes only and were not intended to develop a material rating; however, the results were evaluated relative to ASTM G64-91 (ref. 48) and NASA MSFC-SPEC-522B (ref. 49).

ASTM G64-91 classifies the resistance of aluminum alloys to stress corrosion cracking with ratings A (very high) through D (low), based on laboratory test results from multiple lots of material and on service history. To meet an A rating requires no specimen fractures in laboratory tests with exposure stress at 75 percent of the specified minimum yield strength and no record of service problems. The MSFC specification sets the criteria for selection of materials for launch vehicle application and provides both design guidelines to control stress corrosion cracking and tables of recommended materials, based on laboratory testing and service experience. Materials are grouped in three tables, identified as 1, 2, and 3, and referenced as high, moderate, or low resistance to stress corrosion cracking, respectively. The current external tank material 2219 is rated A by ASTM G64-91 and is considered table 1 material by MSFC-SPEC-522B for all products in T6 and T8 tempers. Stress corrosion test results in the present study indicate the 2090-T8 extrusion would be rated A by ASTM G64-91 and should be sufficient for table 1 inclusion by MSFC-SPEC-522B.

4.5.1. Exfoliation. The exfoliation results for the 2090 extrusion, summarized in table 7, indicate that moderate exfoliation occurred during the EXCO test, while only pitting occurred during the dry bottom MASTMAASIS test. The general appearance of the specimens after exposure is shown in figure 34.

The EXCO test was developed for 2XXX and 7XXX series aluminum alloys and has been documented to produce overly severe ratings for Al-Li alloys (ref. 14),

which develop corrosion pits during exposure to the EXCO environment. The pits undercut the surface, resulting in flaking of the undercut material. This flaking is mistaken for exfoliation during visual inspection and rating and accounts for the ED rating applied to the 2090 extrusions (refs. 11 and 14) and plate (ref. 14) shown in table 7. The dry bottom MASTMAASIS test has been shown to produce results for Al-Li alloys that correlate well with atmospheric exposures (ref. 14). The test also accurately discriminates between resistant and susceptible tempers of 2090. The MASTMAASIS data shown in table 7 indicate the performance of the near net shape extrusion is similar to 2090 plate and extruded products in the T8 condition (refs. 11 and 14). The EXCO test also indicated that exfoliation occurred for the near net shape extrusion, again illustrating the severity of the EXCO test.

Metallographic sections taken from the base and skin of the test samples confirmed that for both EXCO and MASTMAASIS exfoliation test exposures, the corrosion morphology was broad shallow pitting. A representative example of the corrosion morphology is shown in figure 35. The pits were elongated and aligned with grain boundaries in the skin and along material flow lines in the base. The sections do not exhibit the delaminations usually associated with exfoliation (ref. 12); however, there was considerable material dissolution which would be expected in pitting. The extent of corrosion was similar for the extrusion sections exposed by the dry bottom MASTMAASIS procedure with the stiffeners facing up or down.

Table 7. Summary of Exfoliation Results for 2090 Products

Product form	Condition	EXCO (4 day)	Dry bottom MASTMAASIS (4 week)
Near net shape extrusion 50.8-mm × 101.6-mm skin panel	T86	EB ^a	P ^a
Near net shape extrusion 50.8-mm × 152.4-mm extrusion section with two stiffeners	T86		P
10-mm-thick extruded bar (ref. 14)	T86	ED	P
T-stiffened extrusion (ref. 11)	T86	ED	P
12.7-mm-thick plate (ref. 14)	T81	ED	P

^aRatings per ASTM G34-90:
 N no appreciable attack
 P pitting
 EA superficial exfoliation
 EB moderate exfoliation
 EC severe exfoliation
 ED very severe exfoliation

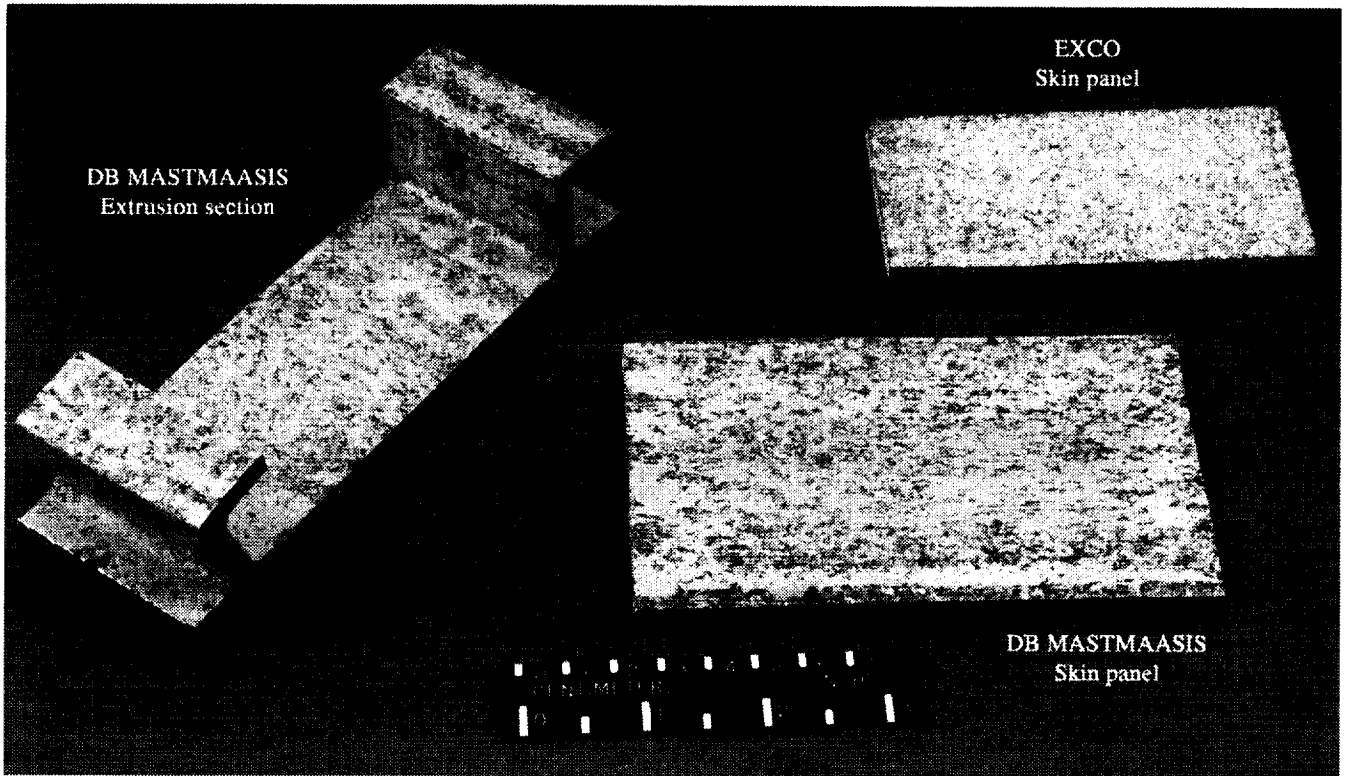
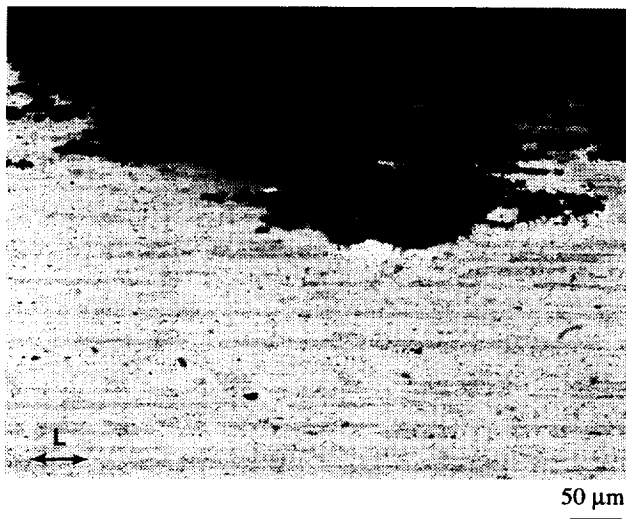
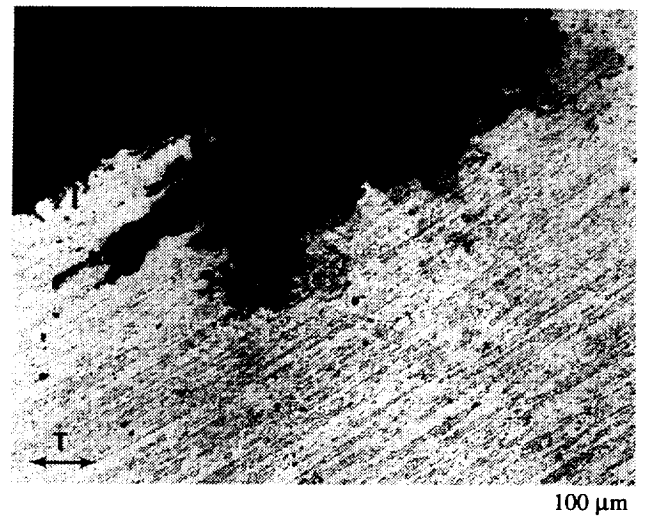


Figure 34. General appearance of 2090-T86 exfoliation specimens after EXCO and dry bottom MASTMAASIS exposures.



(a) Parallel to skin surface.



(b) Along flow lines in fillet associated with extrusion process.

Figure 35. The 2090-T86 MASTMAASIS exfoliation specimens illustrating pitting attack with undercutting.

4.5.2. Stress corrosion.

Direct-tension tests: The direct-tension tests of the 2090 near net extrusion resulted in no failures (specimen fracture) after 40 days exposure with stress as high as 80 percent of the material yield stress. The results are

summarized as pass or fail tests in table 8 for comparison with published results for 2090 and 2219 in similar temper or product forms (refs. 11, 44, and 50). The data indicate that the 2090 near net shape extrusion in the T86 (peak-aged) condition retained the resistance to stress corrosion cracking documented for other peak and near

Table 8. Summary of Long Transverse Stress Corrosion Test Results for 2090 and 2219 Products

Alloy /product form	Condition	Orientation	Exposure stress, MPa (% S_y)	Exposure time, days	NF/NT ^a
2090 Near net shape extrusion	T86	LT Beneath stiffener	136 (25)	40	0/3
			273 (50)		0/3
			409 (80)		0/3
2090 14-mm × 60-mm extruded bar (ref. 44)	Near peak aged	LT	140 (25)	90	0/2
			210 (38)		0/2
			280 (50)		0/2
2090 12.7-mm-thick plate (ref. 11)	T81	LT	414 (75)	30	0/5
2219 12.7-mm-thick plate (ref. 50)	T87	LT	270 (75)	90	0/3

^aNF/NT, number failed/number tested.

peak-aged 2090 product forms and performed equally well to peak-aged 2219.

Resistance to stress corrosion can also be determined with direct-tension specimens by measurements of post exposure residual strength. Residual strengths, expressed as breaking stress (failure load/original cross-sectional area), are plotted in figure 36 for specimens exposed at several stress levels. The breaking stress was reduced by about 12 percent for the unstressed specimens exposed for 40 days, with only an additional 3-percent reduction for the highest stress exposures. The data indicate that the reduction in breaking stress was due primarily to general corrosion. Bucci et al. (ref. 11) observed similar corrosion performance with a 12.7-mm 2090-T86 plate (6-percent and 10-percent losses in residual strength for unstressed and 75 percent S_y , respectively). In comparison, data from direct-tension tests with 12.7-mm-thick 2219-T87 (peak-aged) plate indicated a 30-percent reduction in residual strength for LT specimens stressed to 75 percent S_y and exposed by alternate immersion in a 3.5-percent NaCl solution (ref. 50).

Metallographic sections from direct-tension specimens confirmed pitting attack, with pits undercutting the specimen surface along grain-subgrain boundaries. While there were no stress corrosion cracks observed in the stressed specimens, the pits were opened into broad, deep fissures. All direct-tension specimens failed away from the center of the reduced section during the breaking stress tests, with macroscopic fracture along boundaries of pancake-shaped grains aligned with the fillet, as was shown in figure 5(d). Additional specimens exposed at 0 percent and 75 percent S_y were used to further examine the corrosion morphology; therefore, the specimens were not failed in tension. One of these sections, shown

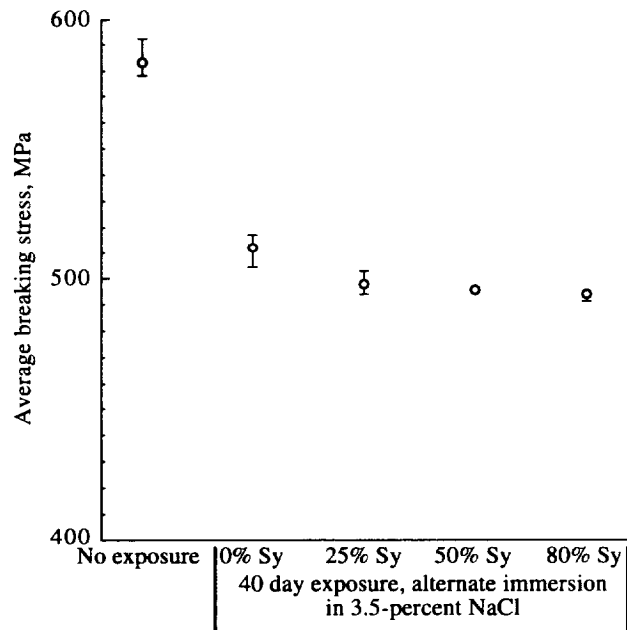
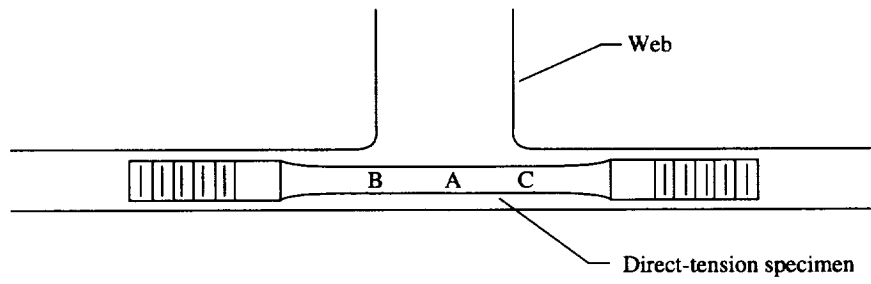
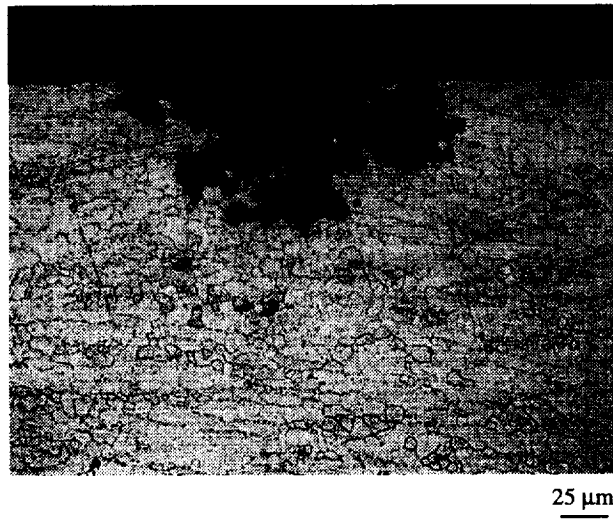


Figure 36. Variation in breaking stress with exposure stress for 2090-T86 long transverse direct-tension specimens. Bars represent range of data.

in figure 37, illustrates that the pits undercut along flow lines associated with the extrusion process. The pits were nearly equiaxed at the center of the reduced section and undercut parallel to the specimen surface. The microstructure at this position at the base of the stiffener exhibited mixed-pancake and fibrous grains, as shown in figure 5(e), with grain boundaries generally aligned parallel to the skin surface. To either side of the center of the reduced section, the pits were deep fissures and undercut at an angle following grain boundaries. The



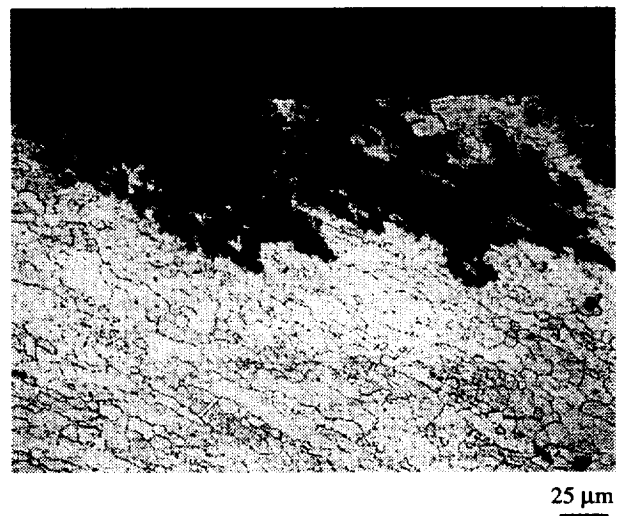
(a) Schematic of transverse direct-tension specimen position.



(b) Region A.



(c) Region B.



(d) Region C.

Figure 37. Long transverse 2090-T86 direct-tension specimen illustrating pitting attack along material flow lines associated with extrusion process.

microstructure at these positions consisted of angled pancake-shaped grains, aligned with the fillet due to material flow during extrusion, as shown in figure 5(d). The direct-tension specimens fractured at these positions, with the fracture surface aligned with the direction of material flow. The pits appeared deeper in the stressed specimens, suggesting that stress-assisted pitting may be the primary form of attack in the stressed specimens.

Modified c-ring tests: Modified c-ring specimens were used to evaluate stress corrosion resistance in the short transverse orientation of the extruded panel. There were no failures observed in the modified c-ring specimens, where failure is defined as the onset of cracking, regardless of the location of the resulting tensile stresses. Specimens with wax coating on the stiffener web did not display cracking in the fillet. The test results are summarized in table 9 and are compared with published short transverse stress corrosion data for thick 2090 and 2219 products. Results from the current near net shape extrusions and a T-stiffened extrusion (ref. 11) indicate stress corrosion resistance at stress levels of 70 percent S_y and approximately 50 percent S_y , respectively. Data in table 9

for thick plate (refs. 11 and 44) indicated that stress corrosion failures can occur at stress levels above ~40 percent S_y in 2090 aged-to-near peak strength, above ~70 percent in peak-aged 2090 (ref. 45), and at 75 percent S_y in peak-aged 2219 (ref. 51). Wrought aluminum products are most susceptible to stress corrosion cracking with short transverse loading because tensile stresses are produced normal to long grain boundaries (preferential crack paths). The microstructure associated with the near net shape extrusion was significantly different from that of thick plate or axisymmetric extrusions. The flow of material into the extrusion die resulted in grain boundaries in the stiffener aligned with the short transverse panel direction (figs. 5(b) and 5(c)). Consequently, stress corrosion tests to evaluate the short transverse orientation produced microstructural stresses parallel to grain boundaries and resulted in higher stress corrosion threshold stress levels.

Metallographic sections from both stressed and unstressed modified c-ring specimens did not identify any stress corrosion cracks but verified pitting with undercutting parallel to the specimen surfaces along

Table 9. Summary of Short Transverse SCC Test Results for 2090 and 2219 Products

Alloy/product form	Condition	Exposure stress, MPa (% S_y)	Exposure time, days	NF/NT ^a
2090 Near net shape extrusion ^b	T86	354 (70)	75	0/12
2090 50-mm × 115-mm extruded bar ^c (ref. 45)	Peak aged	172 (40) 241 (55) 310 (71)	84 84 30	0/6 0/6 1/6
2090 T-stiffened extrusion ^d (ref. 11)	T86	104 (20) 173 (34) 242 (47)	84	0/5 0/5 0/5
2090 38-mm-thick plate ^c (ref. 11)	T81	104 (23) 138 (31) 173 (39) 242 (55)	30	0/5 0/5 4/5 5/5
2090 40-mm-thick plate ^c (ref. 44)	Near peak aged	70 (13) 140 (27) 210 (40)	30	0/3 1/3 3/3
2090 40-mm-thick plate ^e (ref. 44)	Near peak aged	70 (13) 140 (27) 210 (40) 280 (54)	30	0/3 0/3 0/3 3/3
2219 50-mm-thick plate (ref. 51)	T87	275 (75)	30	3/17

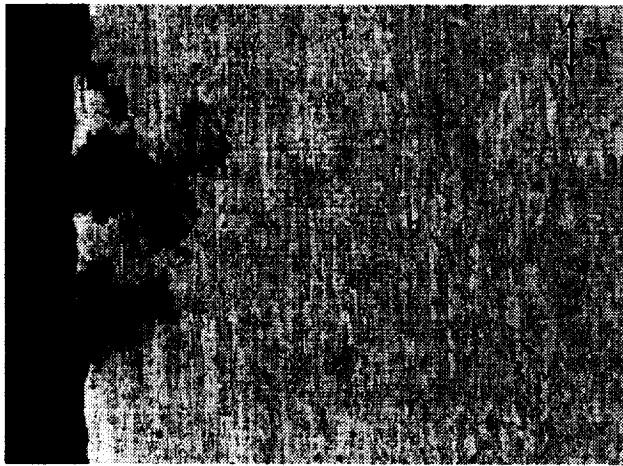
^aNF/NT, number failed/number tested.

^bModified c-ring specimen (appendix C, table C11).

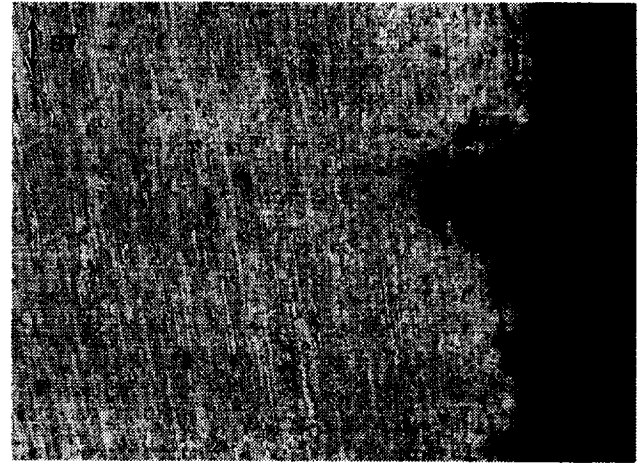
^c3.18-mm diameter tensile specimens.

^d19-mm diameter by 1.6-mm thick c-ring specimens.

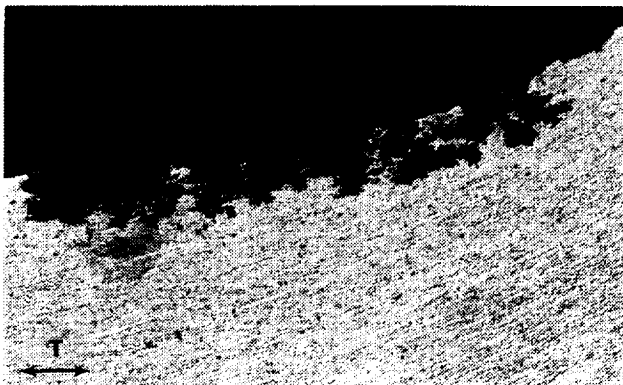
^e18-mm-diameter c-ring specimens.



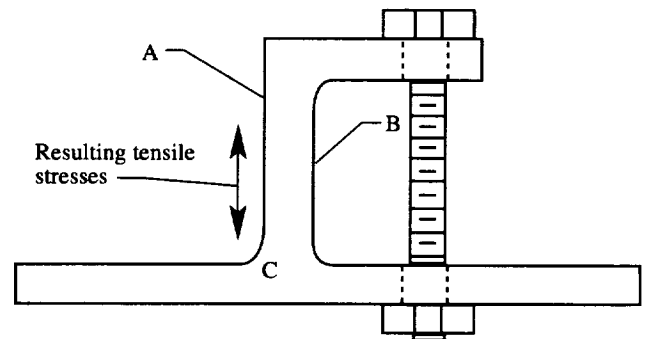
(a) Region A web loaded in tension.



(b) Region B web loaded in compression.



(c) Region C fillet loaded in tension.



(d) Tensile stress at outer web/radius.

Figure 38. Pitting attack on 2090-T86 modified c-ring.

grain-subgrain boundaries associated with material flow, as shown in figure 38. The pits on tensile surfaces were deeper, with less undercutting, but still did not develop prominent crack fronts. The unstressed specimens confirmed that residual stresses were not present in magnitudes that would support stress corrosion cracking.

The current test results from direct-tension and modified c-ring specimens for panel 6 (T86) indicate stress corrosion resistance which would support an A rating according to ASTM G64-91 and should be sufficient for inclusion in table 1 according to MSFC-SPEC-522B. Additional testing is required to certify a material rating; however, based on the current corrosion data, the 2090 near net shape extrusion appears to be a viable substitution for 2219 for cryotank application.

5. Concluding Remarks

The results from this study discuss work which has been completed as part of an ongoing program. As such, this document is primarily a data report with analyses and conclusions based upon all data available at the time of writing. The near net shape extrusions were produced in the Commonwealth of Independent States (CIS) on a best effort basis by using available unmodified production equipment. Therefore, although the present evaluation in the United States shows that the extrusions do not meet current United States manufacturing tolerances for extruded aluminum shapes, other Al-Li alloys and modified production techniques currently under development in the CIS and in the United States will hopefully produce better quality near net shape products.

The 2090 microstructure was complex as a result of the near net shape extrusion process. The material exhibited microstructural directionality parallel to the extrusion axis throughout the cross section. The grain structure was predominantly unrecrystallized; grains were fibrous in the cap and pancake-shaped in the skin, with a mixture of both in the web and in the base.

The results of the texture analysis were consistent with an unrecrystallized material containing isolated areas of recrystallized grains. The cap and the web had predominantly fiber textures which were $\langle 111 \rangle$ and $\langle 112 \rangle$, respectively. The skin had a Brass texture while the base had a mixture of the $\langle 111 \rangle$ fiber and the Copper rolling textures.

The preferred orientation and grain flow patterns exhibited by the microstructure influenced the tensile properties and the fracture behavior. The tensile properties were comparable with typical values reported for other 2090 product forms. The variation in the 45° off-axis properties was a result of the unrecrystallized nature of the microstructure.

The cap and the base had the highest strength, primarily as a result of the fibrous grain structure and $\langle 111 \rangle$ fiber texture. The lowest strengths were measured in the 45° direction in the skin, which is typical of anisotropic, unrecrystallized material. There was a small reduction in yield strength from the front to the back of the extrusion; however, elongation to failure did not vary systematically with panel length. Trends in the tensile behavior with respect to temperature were not discernible due to inconsistencies in the data.

The main thrust of the fracture tests was to determine the effect of temperature on toughness. Toughness data were obtained from specimens in the longitudinal and long transverse orientations. Fracture toughness tests at Langley Research Center (LaRC) using M(T) specimens exhibited a decrease in toughness with decreasing temperature in the T-L orientation. Residual strength tests on surface crack specimens performed by Boeing Aerospace exhibited decreasing toughness with decreasing temperature in the T-S orientation and increasing toughness with decreasing temperature in the L-S orientation. Data generated by NIST indicated that toughness was dependent on the surface crack geometry and test temperature.

The extrusion proved readily weldable by the VPPAW process. Mechanical properties of the extrusion weldments compared favorably to those of welded 2090 sheet and plate. There was a trend of lower tensile strength and toughness in the weldment compared to the skin material.

Corrosion resistance of the extrusion was comparable to other peak-aged 2090 product forms, indicating that the extrusion process did not affect the corrosion resistance. There were no exfoliation or stress corrosion failures in the tests performed. The only form of corrosion observed was pitting as a result of preferential attack along grain boundaries, which delineated material flow associated with the extrusion process. There were no stress corrosion cracks observed in stressed or unstressed specimens, suggesting that the microstructure does not contain preferential paths for sustained stress corrosion cracking and that residual stresses could not support stress corrosion cracking. Corrosion resistance was comparable to peak-aged 2219 plate.

Based on the available data from the fracture tests, it is unlikely that the 2090 near net shape extrusions could be considered a viable replacement for 2219-T87 in the current external tank (ET) structure where damage tolerance at cryogenic temperatures is required, such as in the liquid hydrogen or liquid oxygen tanks. Near net shape extrusions of 2090 could be considered as a replacement in the intertank structure, where failure due to buckling is more important and stiffness is the desirable property.

NASA Langley Research Center
Hampton, VA 23681-2199
December 11, 1997

6. References

1. Kaminski, T.; Willner, E.; Kerr, J.; and Taketani, H.: Aluminum-Lithium in Space Applications. *Aluminum-Lithium*, M. Peters and P.-J. Winkler, eds., DGM, 1991, pp. 1311-1314.
2. Swanson, G. M.; Loechel, L. W.; Hartley, P. J.; and Bolstad, D. A.: Net Shape Processes and Properties of Weldalite™ Components. *Aluminum-Lithium*, M. Peters and P.-J. Winkler, eds., DGM, 1991, pp. 981-986.
3. SAE Aerospace Material Specification MAM2205A: *Tolerances, Metric Aluminum Alloy and Magnesium Alloy Extrusions*. SAE International, Oct. 1983. URL: <http://www.sae.org>, Accessed December 3, 1997.
4. Standard Methods of Tension Testing Wrought and Cast Aluminum- and Magnesium-Alloy Products. ASTM Designation: B 557-84, Volume 03.01 of the *1989 Annual Book of ASTM Standards*, 1989, pp. 50-60.
5. Standard Test Methods of Tension Testing of Metallic Materials. ASTM Designation: E 8-89, Volume 03.01 of the *1989 Annual Book of ASTM Standards*, 1989, pp. 131-146.
6. Standard Practice for Fracture Testing With Surface-Crack Tension Specimens. ASTM Designation: E 740-88, Volume 03.01 of the *1989 Annual Book of ASTM Standards*, 1989, pp. 674-681.

7. Standard Practice for R-Curve Determination. ASTM Designation: E 561-86, Volume 03.01 of the 1989 *Annual Book of ASTM Standards*, 1989, pp. 570–581.
8. Anon.: Welding, Aluminum Alloys. MSFC-SPEC-504C, Nov. 1990, pp. 1–39.
9. Martukanitz, R. P.; Natalie, C. A.; and Knoefel, J. O.: The Weldability of an Al-Li-Cu Alloy. *J. Metals*, vol. 39, no. 11, Nov. 1987, pp. 38–42.
10. Lippold, John C.: Weld Solidification Cracking in Commercial Al-Li Alloys. *Advances in Joining Newer Structural Materials*, Pergamon Press, 1990, pp. 263–270.
11. Bucci, R. J.; Malcolm, R. C.; Colvin, E. L.; Murtha, S. S.; and James, R. S.: *Cooperative Test Program for the Evaluation of Engineering Properties of Aluminum-Lithium Alloy 2090-T8X Sheet, Plate, and Extrusion Products*. Alcoa Rept. No. NSWC-TR-89-106, Sept. 1989. (Available from DTIC as AD-B141340L.)
12. Standard Test Method for Exfoliation Corrosion Susceptibility in 2XXX and 7XXX Series Aluminum Alloys (EXCO Test). ASTM Designation: G 34-90, Volume 03.02 of the 1992 *Annual Book of ASTM Standards*, 1992, pp. 127–132.
13. Standard Practice for Modified Salt Spray (Fog) Testing. ASTM Designation: G 85-85, Volume 03.02 of the 1992 *Annual Book of ASTM Standards*, 1992, pp. 357–361.
14. Colvin, E. L.; and Murtha, S. J.: Exfoliation Erosion Testing of Al-Li Alloys 2090 and 2091. *Proceedings of the 5th International Aluminum-Lithium Conference—Aluminum-Lithium Alloys*, 1989, pp. 1251–1260.
15. Standard Practice for Preparation and Use of Direct Tension Stress-Corrosion Test Specimens. ASTM Designation: G 49-85, Volume 03.02 of the 1992 *Annual Book of ASTM Standards*, 1992, pp. 189–193.
16. Standard Practice for Evaluating Stress Corrosion Cracking Resistance of Metals and Alloys by Alternate Immersion in 3.5% Sodium Chloride Solution. ASTM Designation: G 44-88, Volume 03.02 of the 1992 *Annual Book of ASTM Standards*, 1992, pp. 170–173.
17. Reynolds, M. A.; and Creed, E.: The Development of 8090 and 8091 Alloy Extrusions. *J. de Phys., Suppl.*, vol. 48, Sept. 1987, pp. C3-195–C3-207.
18. Parson, N. C.; and Sheppard, T.: Extrusion Processing of Al-Mg-Li Alloys. *Proceedings of the Third International Aluminum-Lithium Conference—Aluminum-Lithium Alloys III*, C. Baker, P. J. Gregson, S. J. Harris, and C. J. Peel, eds., London, Inst. of Metals, 1986, pp. 222–232.
19. Tempus, G.; Scharf, G.; and Calles, W.: Influence of Extrusion Process Parameters on the Mechanical Properties of Al-Li-Extrusions. *J. de Phys., Suppl.*, vol. 48, Sept. 1987, pp. C3-187–C3-193.
20. Dinsdale, K.; Harris, S. J.; and Noble, B.: Relationship Between Microstructure and Mechanical Properties of Aluminum-Lithium-Magnesium Alloys. *Aluminum-Lithium Alloys*, Metall. Soc. of AIME, 1981, pp. 101–118.
21. Palmer, I. G.; Lewis, R. E.; and Crooks, D. D.: The Design and Mechanical Properties of Rapidly Solidified Al-Li-X Alloys. *Aluminum-Lithium Alloys*, Metall. Soc. of AIME, 1981, pp. 241–262.
22. Lin, F. S.; Chakraborty, S. B.; and Starke, E. A., Jr.: Microstructure-Property Relationships of Two Al-3Li-2Cu-0.2Zr-XCd Alloys. *Meteorol. Trans.*, vol. 13A, 1982, pp. 401–410.
23. Kar, R. J.; Bohlen, J. W.; and Chanani, G. R.: Correlation of Microstructures, Aging Treatments, and Properties of Al-Li-Cu-Mg-Zr I/M and P/M Alloys. *Proceedings of the Second International Aluminum-Lithium Conference—Aluminum-Lithium Alloys II*, Metall. Soc. of AIME, 1984, pp. 255–285.
24. Dillamore, I. L.; and Roberts, W. T.: Preferred Orientation in Wrought and Annealed Metals. *Metall. Rev.*, vol. 10, no. 39, 1965, pp. 271–380.
25. Gregson, P. J.; and Flower, H. M.: Microstructural Control of Toughness in Aluminum-Lithium Alloys. *Acta Metall.*, vol. 33, Mar. 1985, pp. 527–537.
26. Reynolds, M. A.; Gray, A.; Creed, E.; Jordan, R. M.; and Titchener, A. P.: Processing and Properties of Alcan Medium and High Strength Al-Li-Cu-Mg Alloys in Various Product Forms. *Proceedings of the Third International Aluminum-Lithium Conference—Aluminum-Lithium Alloys III*, London, Inst. Metals, 1986, pp. 57–65.
27. Grimes, R.; Reynolds, M. A.; Titchener, A. P.; Greaves, M. S.; Strassheim, I.; and Warrington, D.: The Commercial Manufacture of 8090 Plate, Sheet and Extrusions. *Aluminum-Lithium*, M. Peters and P.-J. Winkler, eds., DGM, 1991, pp. 3–14.
28. Cassada, W. A.; Shiflet, G. J.; and Starke, E. A., Jr.: The Effect of Plastic Deformation on T1 Precipitation. *J. de Phys., Suppl.*, vol. 48, Sept. 1987, pp. C3-397–C3-406.
29. Rioja, R. J.; Bretz, P. E.; Sawtell, R. R.; Hunt, W. H.; and Ludwiczak, E. A.: Precipitation Reactions, Strength and Toughness of Al-Li-Cu Alloys. *Proceedings of the International Conference—Aluminum Alloys: Their Physical and Mechanical Properties*, Eng. Mater. Advis. Serv., Ltd., 1986, pp. 1781–1797.
30. Reed, R. P.; Purtschere, P. T.; Simon, N. J.; McCloskey, J. D.; and Walsh, R. P.: *Aluminum Alloys for ALS Cryogenic Tanks: Comparative Measurements of Cryogenic Mechanical Properties of Al-Li Alloys and Alloy 2219*. NISTIR-3979, Feb. 1993.
31. Engstrom, W. L.: *Determination of Design Allowable Properties—Fracture of 2219-T87 Aluminum Alloy*. NASA CR-115388, 1972.
32. Buscemi, Charles D.; and Chin, Ernest S. C.: Characterization of X2090 Al-Li-Alloy. *Proceedings of the Twentieth Annual Technical Meeting of the International Metallographic Society*, H. J. Cialoni, G. W. E. Johnson, M. E. Blum, and G. V. Vander Voort, eds., Intern. Metall. Soc./ASM Intern., 1988, pp. 221–230.
33. Venkateswara Rao, K. T.; and Ritchie, R. O.: Fracture-Toughness Behavior of 2090-T83 Aluminum-Lithium Alloy

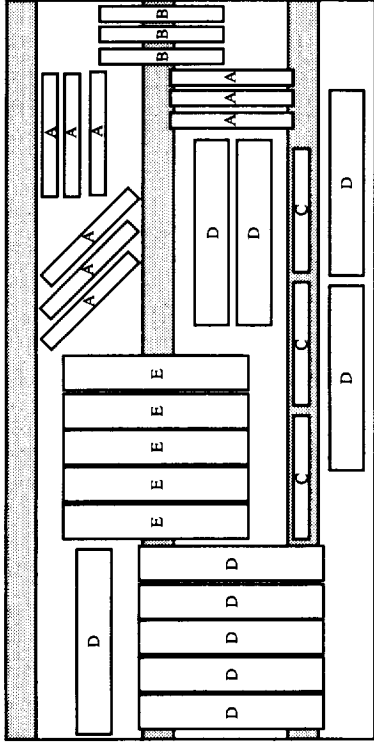
- Sheet at Ambient and Cryogenic Temperatures. *Scripta Metall.*, vol. 23, July 1989, pp. 1129–1134.
34. ALCOA Alloy 2090. *Alloy Digest*, Sept. 1989.
 35. Morris, J. W., Jr.; Glazer, J.; Verzasconi, S. L.; and Sawtell, R.: Mechanical Behavior of Aluminum-Lithium Alloys at Cryogenic Temperatures. *Metall. Trans. A-Phys. Metall. Mater. Sci.*, vol. 18A, Oct. 1987, pp. 1695–1701.
 36. Glazer, J.; Verzasconi, S. L.; Dalder, E. N. C.; Yu, W.; Emigh, R. A.; Ritchie, R. O.; and Morris, J. W., Jr.: Cryogenic Mechanical Properties of Al-Cu-Li-Zr Alloy 2090. *Advances in Cryogenic Engineering Materials*, R. P. Reed and A. F. Clark, eds., Plenum Press, 1986, pp. 397–404.
 37. Libbey, B. W.; and Finger, R. W.: Evaluation of Extruded 2090 Al-Li Wide Stiffened Panels (ADP 3105R) Test Data. AD-B69014L. Boeing Co., Sept. 1992.
 38. Tack, W. T.; and Loechel, L. W.: Use of Applied Fracture Mechanics Principles to Evaluate the Cryogenic Fracture Toughness of Alloy 2090. *Aluminum-Lithium*, M. Peters and P.-J. Winkler, eds., DGM, 1991, pp. 415–420.
 39. Lee, E. W.; and Frazier, W. E.: The Effect of Stretch on the Microstructure and Mechanical Properties of 2090 Al-Li. *Scripta Metall.*, vol. 22, Jan. 1988, pp. 53–57.
 40. Dorward, R. C.: Cryogenic Toughness of Al-Cu-Li Alloy AA 2090. *Scripta Metall.*, vol. 20, Oct. 1986, 1379–1383.
 41. Venkateswara Rao, K. T.; and Ritchie, R. O.: Mechanisms Influencing the Cryogenic Fracture-Toughness Behavior of Aluminum-Lithium Alloys. *Acta Metall. Mater.*, vol. 38, Nov. 1990, pp. 2309–2326.
 42. Gayle, Frank W.; Tack, William Troy; Heubaum, Frank H.; and Pickens, Joseph R.: High Toughness, High Strength Aluminum Alloy Design and Practice. *Aluminum-Lithium*, M. Peters and P.-J. Winkler, eds., DGM, 1991, pp. 203–208.
 43. Kearns, W. H., ed.: *Welding Handbook—Metals and Their Weldability*. American Welding Soc., 1982, p. 318.
 44. Dorward, R. C.; and Hasse, K. R.: Stress Corrosion Characteristics of AlCuLi AA 2090 Alloy. *Corrosion*, vol. 44, no. 12, Dec. 1988, pp. 933–941.
 45. Colvin, E. L.; Murtha, S. J.; and Syss, R. K.: Stress Corrosion Cracking Susceptibility of Alloy 2090. *Proceedings of the International Conference—Aluminum Alloys: Their Physical and Mechanical Properties*, 1986, pp. 1853–1867.
 46. Vasudévan, A. K.; Ziman, P. R.; Jha, S. C.; and Sanders, T. H., Jr.: Stress Corrosion Resistance of Al-Cu-Li-Zr Alloys. *Aluminum-Lithium Alloys III*, C. Baker, P. J. Gregson, S. J. Harris, and C. J. Peel, eds., London, Inst. Metals, 1986, pp. 303–309.
 47. Meletis, E. I.: Stress Corrosion Cracking Properties of 2090 Al-Li Alloy. *Corrosion Cracking*, V. S. Goel, ed., ASM Int., 1986, pp. 315–326.
 48. Standard Classification of Resistance to Stress-Corrosion Cracking of Heat-Treatable Aluminum Alloys. ASTM Designation: G 64-91, Volume 03.02 of the *1992 Annual Book of ASTM Standards*, 1992, 236–238.
 49. *Design Criteria for Controlling Stress Corrosion Cracking*. MSFC-SPEC-522B, Nov. 1977.
 50. Humphries, T. S.: *Stress Corrosion of Aluminum Alloy 2219 Plate and Forging*. NASA TM-79479, 1964.
 51. Humphries, T. S.; and Nelson, E. E.: *Seacoast Stress Corrosion Cracking of Aluminum Alloys*. NASA TM-82393, 1981.

Appendix A

Test Specimen Layout

Figures A1 through A5 present the location and orientation of specimens machined from panels 2, 6, 11, 4, and 7. For panels 2, 6, and 11, multiple specimens were machined at each tensile location at positions in the stiffener and in the skin as shown in the detail view in figures A1 through A3.

- A. L, LT, and 45° skin specimens (LaRC)
- B. LT base specimens (LaRC)
- C. L cap, web, and base specimens (LaRC)
- D. L and LT skin specimens (MSFC)
- E. LT base specimens (MSFC)



Detail of specimen layout at each tensile location

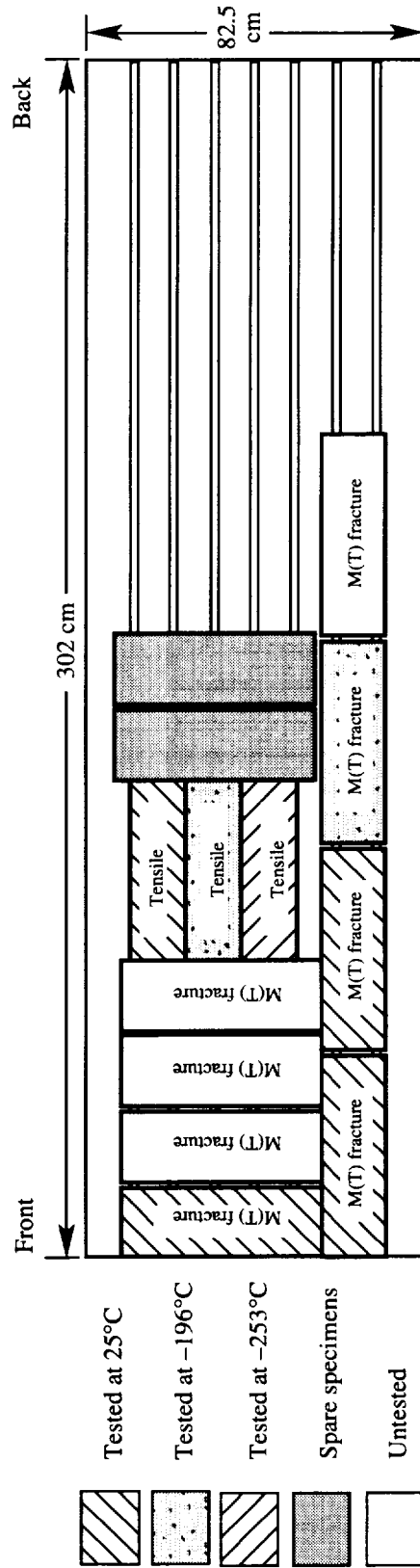
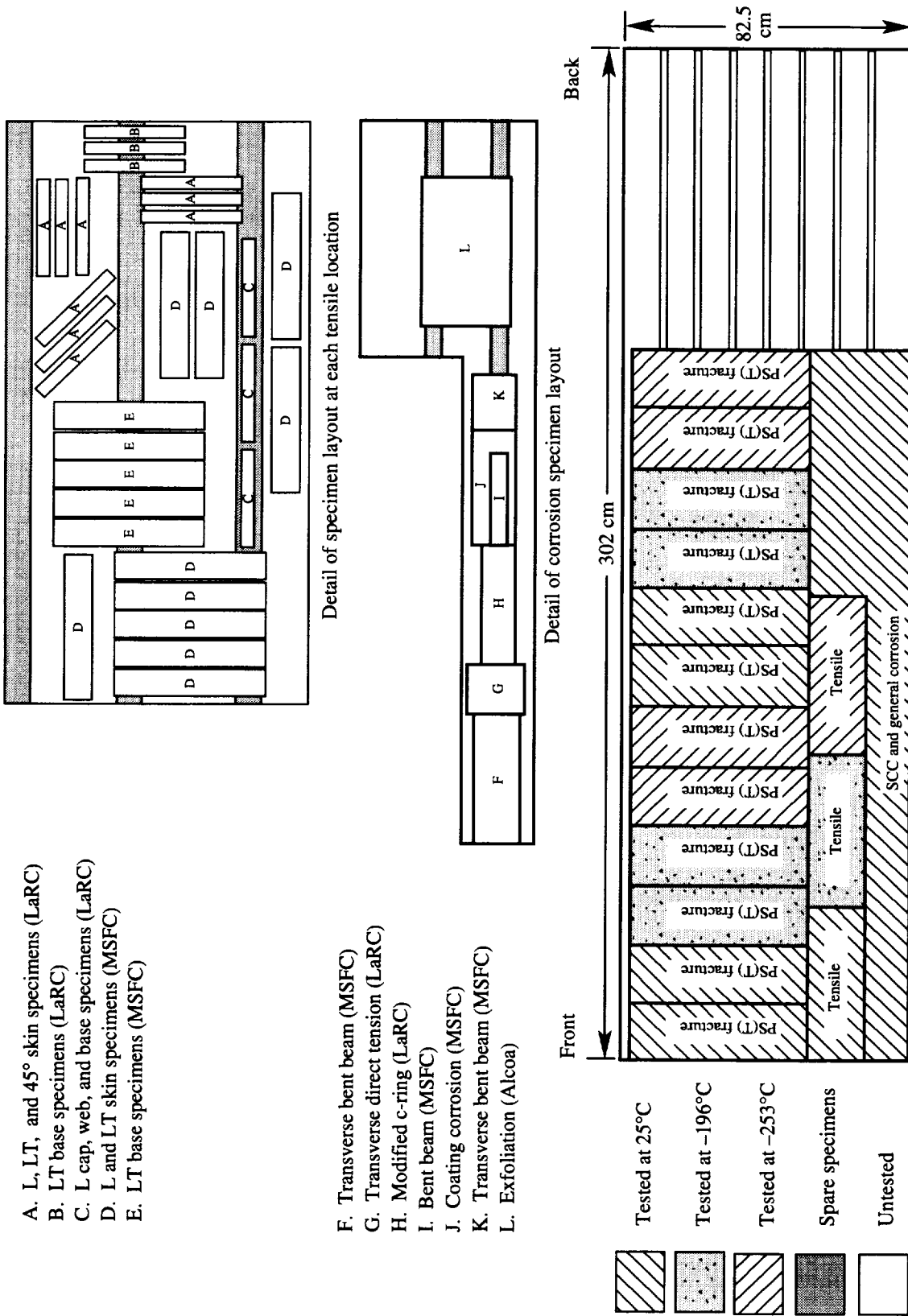


Figure A1. Specimen locations in panel 2.

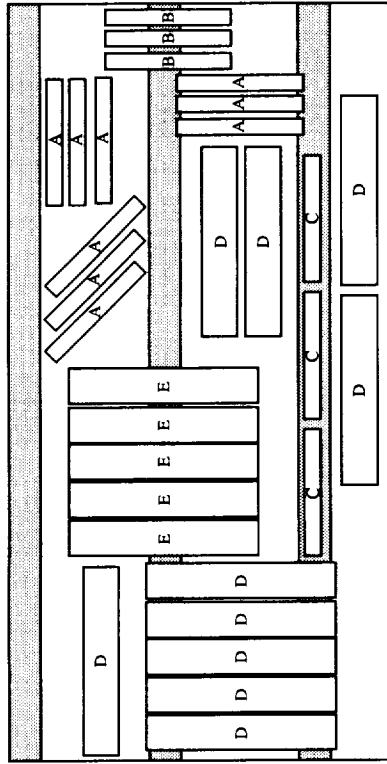


- A. L, LT, and 45° skin specimens (LaRC)
- B. LT base specimens (LaRC)
- C. L cap, web, and base specimens (LaRC)
- D. L and LT skin specimens (MSFC)
- E. LT base specimens (MSFC)

- F. Transverse bent beam (MSFC)
- G. Transverse direct tension (LaRC)
- H. Modified c-ring (LaRC)
- I. Bent beam (MSFC)
- J. Coating corrosion (MSFC)
- K. Transverse bent beam (MSFC)
- L. Exfoliation (Alcoa)

Figure A2. Specimen locations in panel 6.

- A. L, LT, and 45° skin specimens (LaRC)
- B. LT base specimens (LaRC)
- C. L cap, web, and base specimens (LaRC)
- D. L and LT skin specimens (MSFC)
- E. LT base specimens (MSFC)



Detail of specimen layout at each tensile location

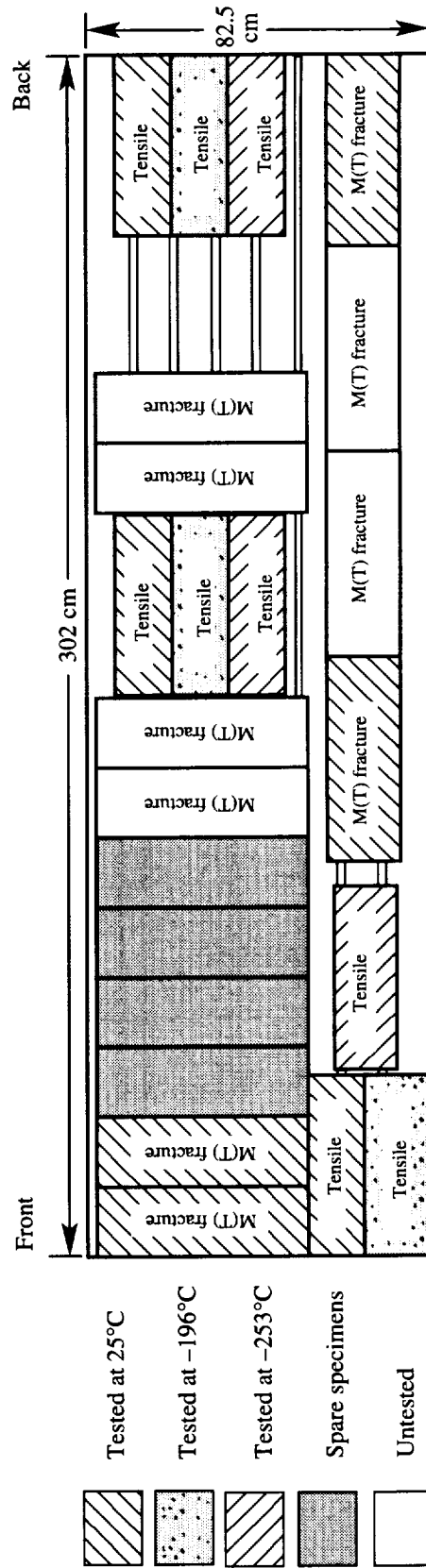


Figure A3. Specimen locations in panel 11.

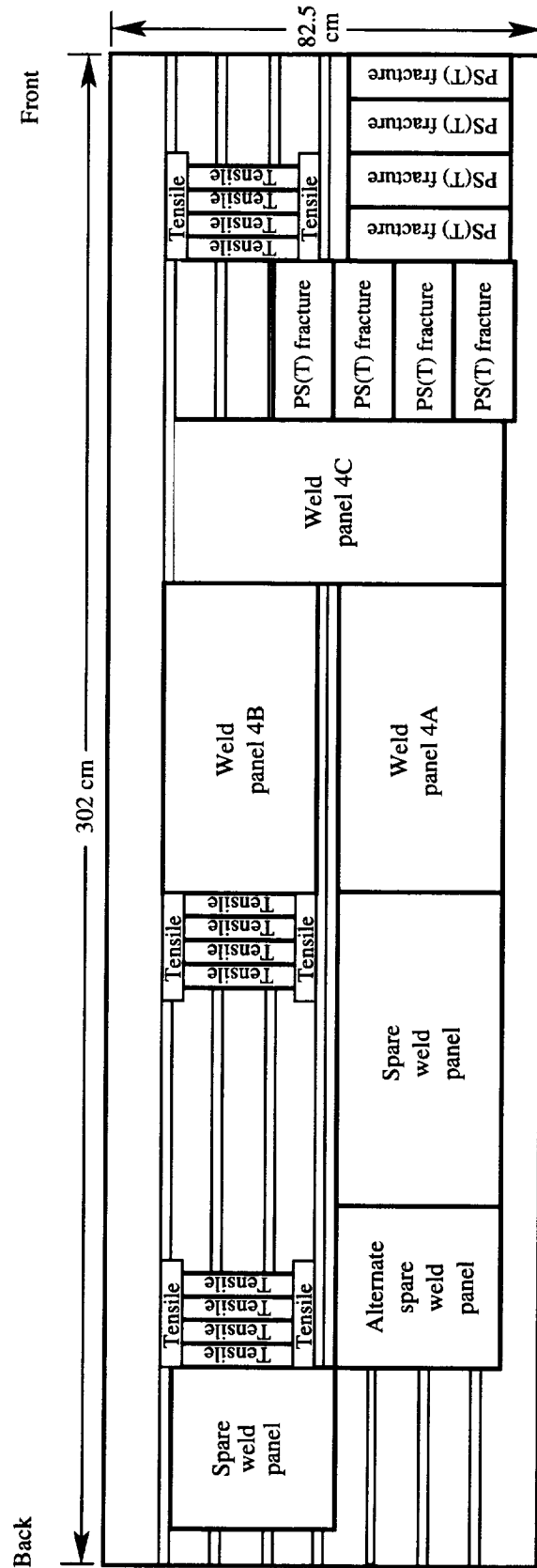


Figure A4. Specimen locations in panel 4.

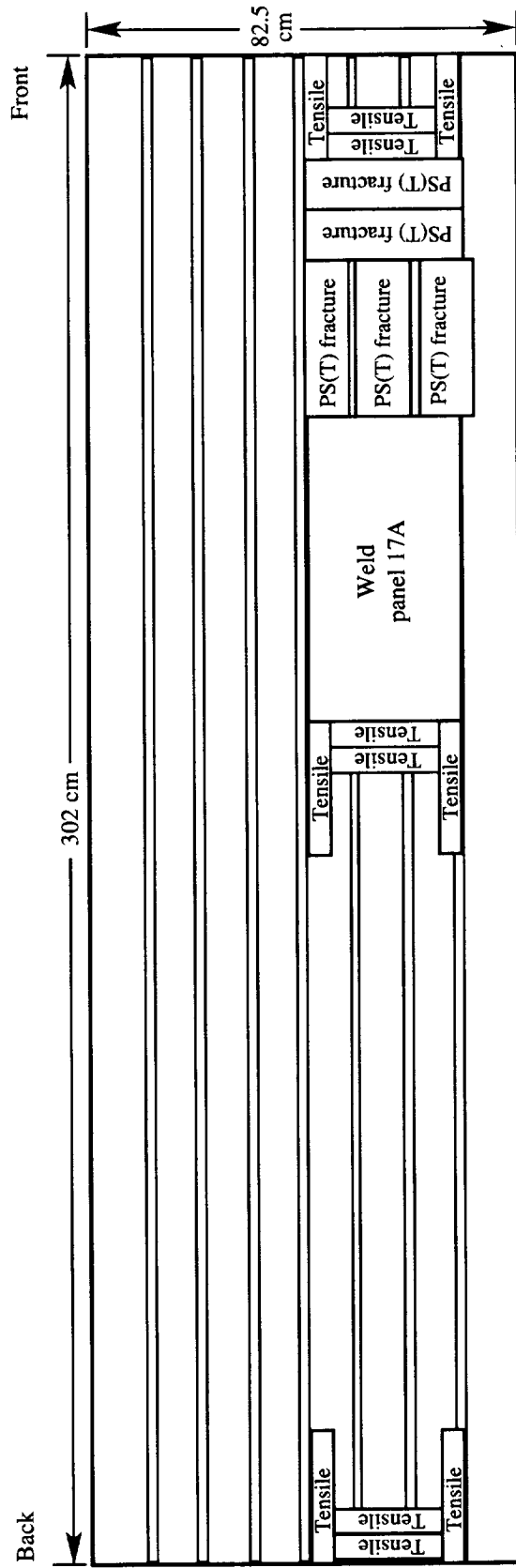


Figure A5. Specimen locations in panel 7.

Appendix B

Test Specimens

Figures B1 through B13 show specimen configurations used for tensile, fracture, and corrosion tests. Figure B14 shows schematically the loading methods used for the c-ring stress corrosion tests.

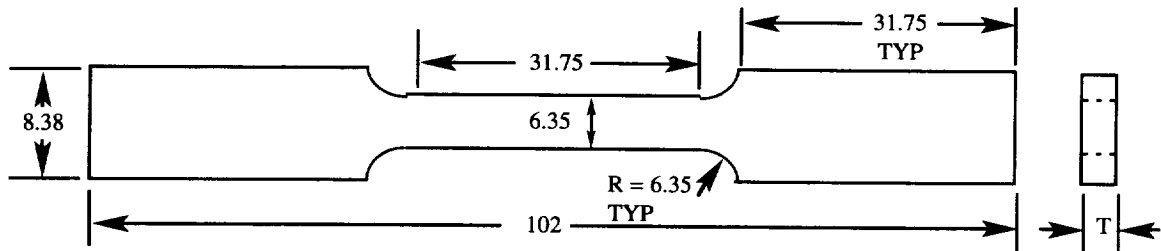


Figure B1. LaRC and Alcoa subsize tensile specimen (full-panel thickness). Dimensions are in mm.

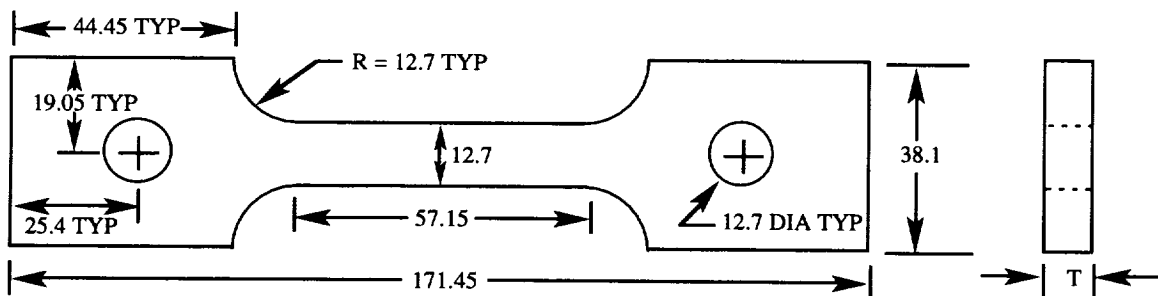


Figure B2. MSFC tensile specimen (full-panel thickness). Dimensions are in mm.

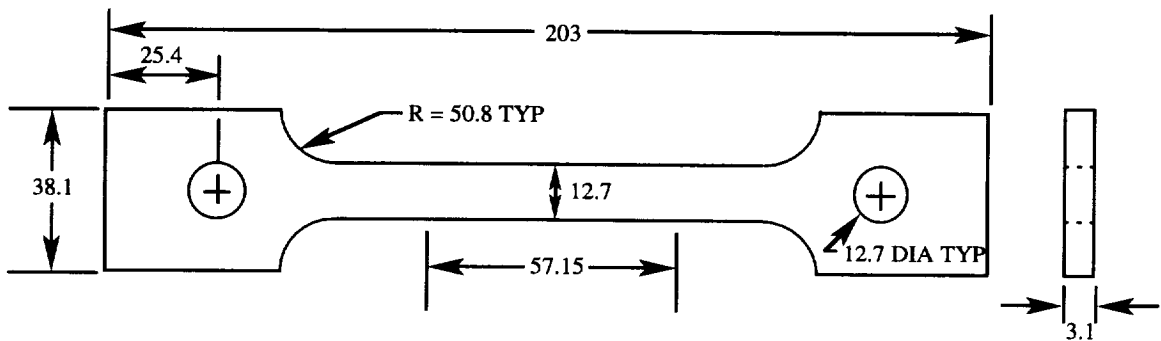


Figure B3. Boeing Aerospace base metal tensile specimen. Dimensions are in mm.

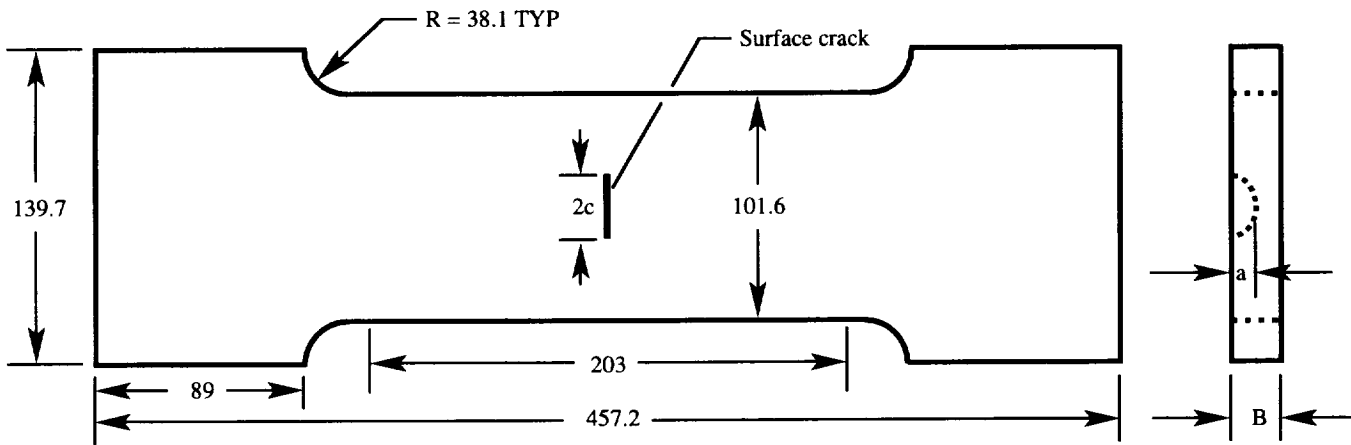


Figure B4. NIST large PS(T) specimen (full-panel thickness). Dimensions are in mm.

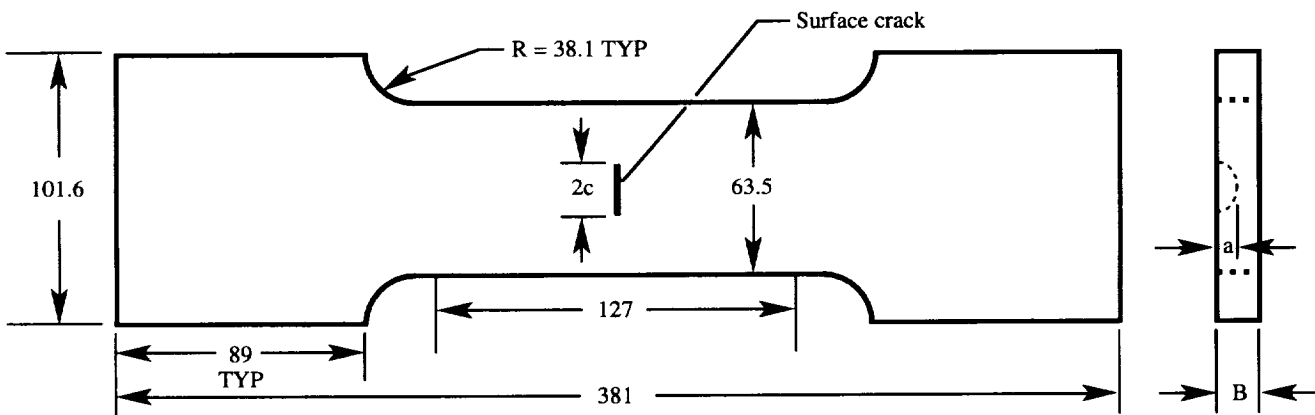


Figure B5. NIST small PS(T) specimen (full-panel thickness). Dimensions are in mm.

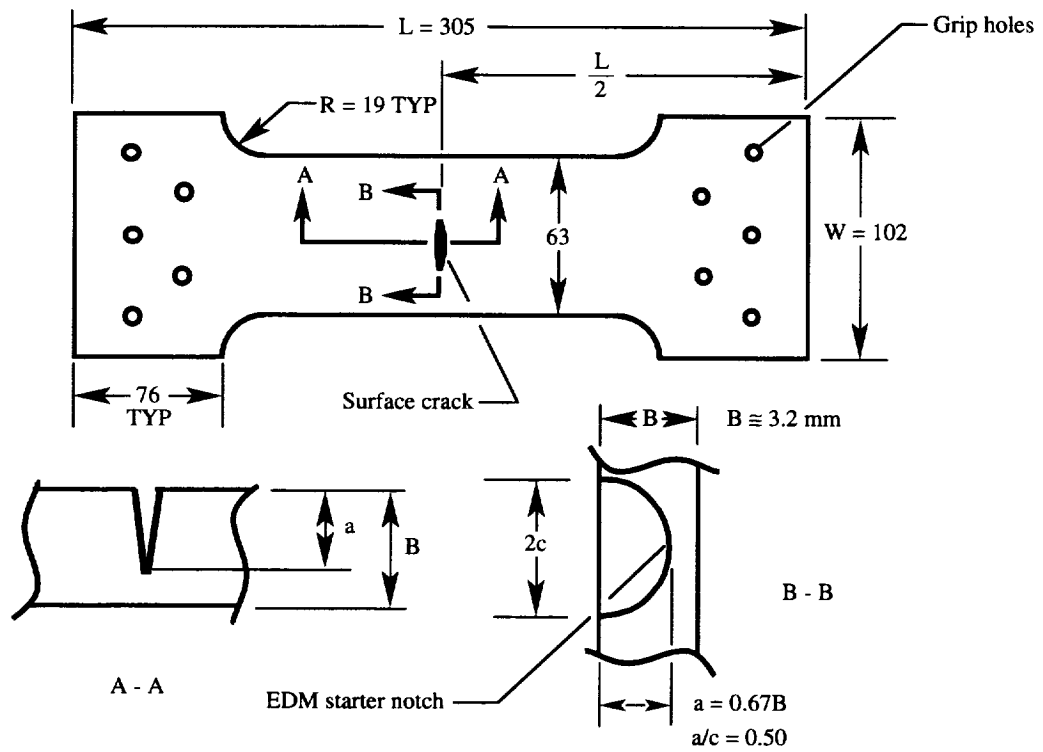


Figure B6. Boeing Aerospace PS(T) specimen. Dimensions are in mm.

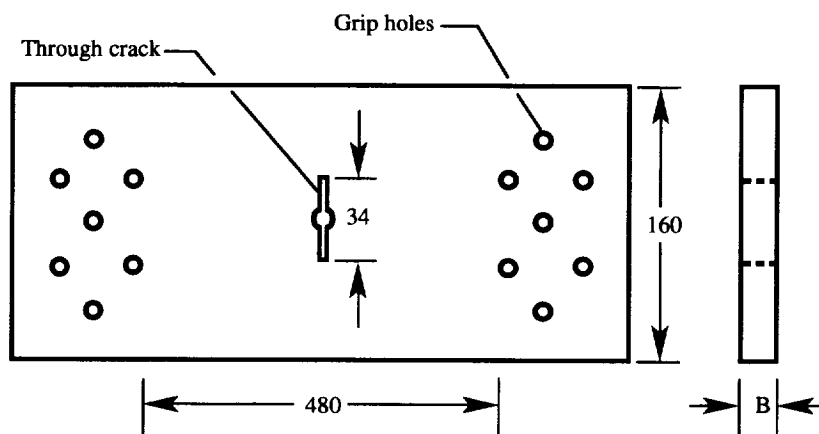


Figure B7. LaRC M(T) specimen (full-panel thickness). Dimensions are in mm.

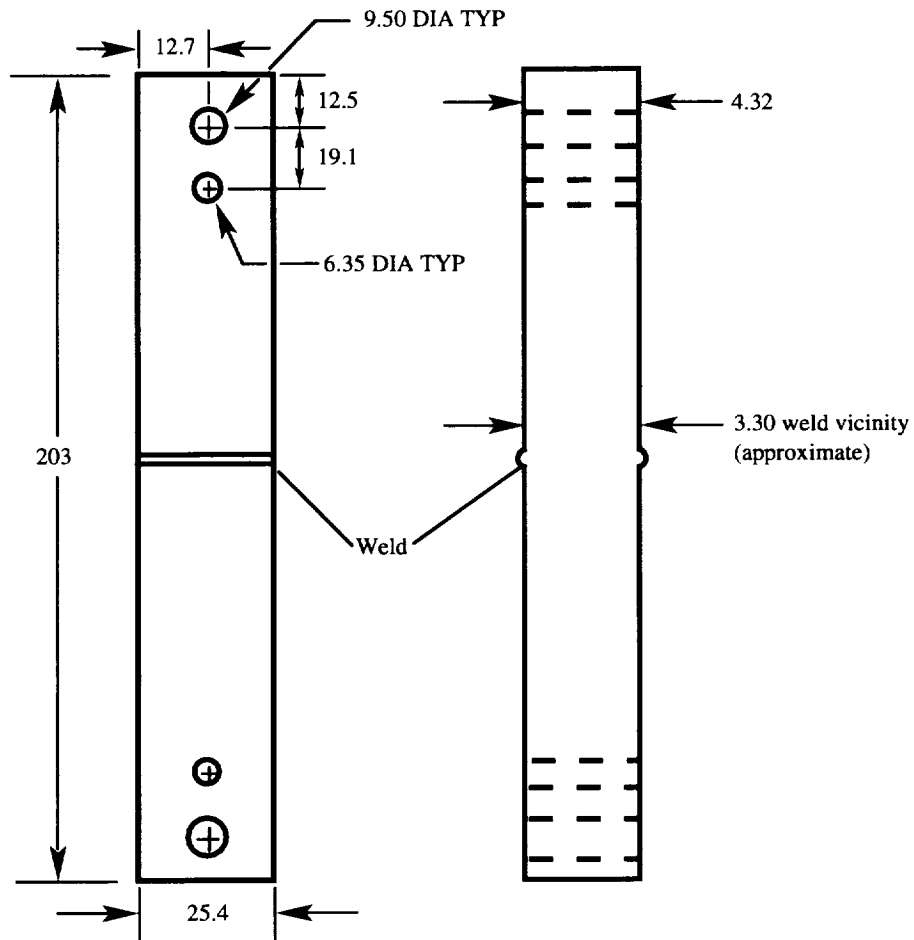


Figure B8. Boeing Aerospace weldment tensile specimen. Dimensions are in mm.

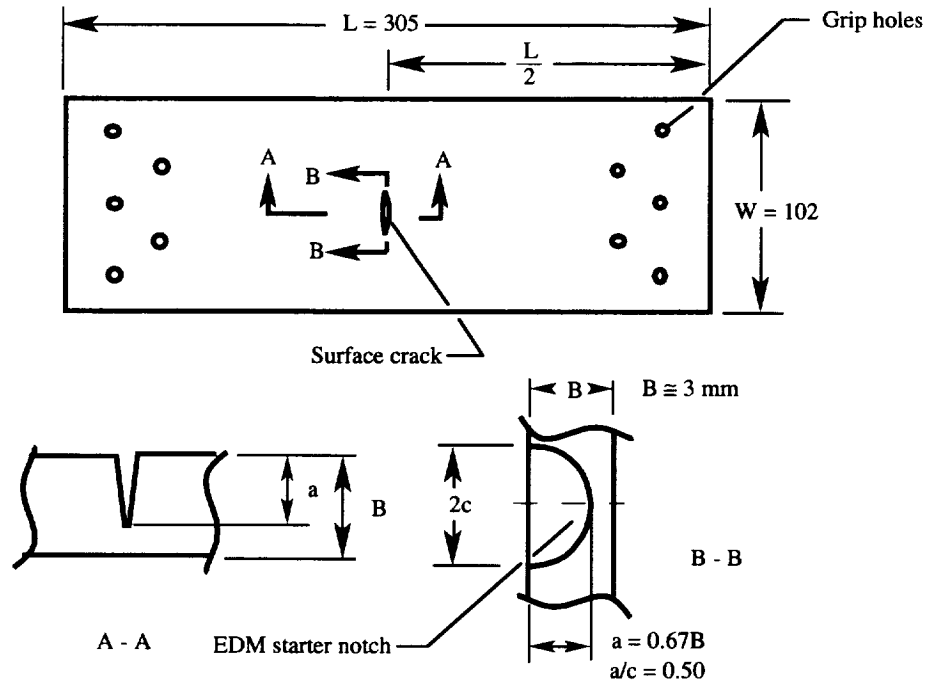


Figure B9. Boeing Aerospace weldment PS(T) specimen. Dimensions are in mm.

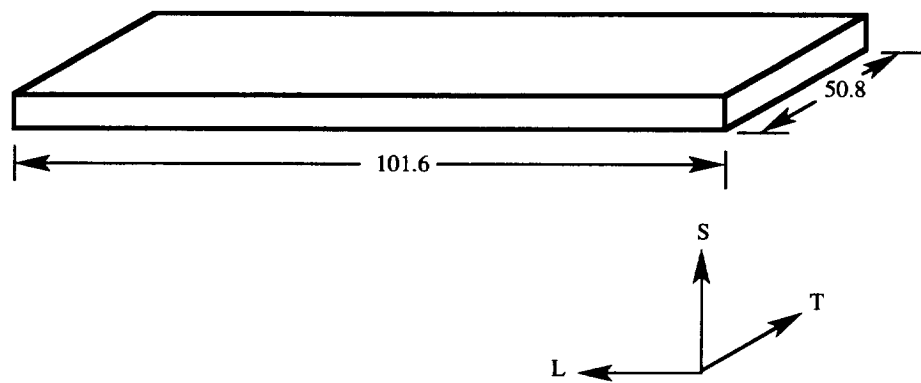
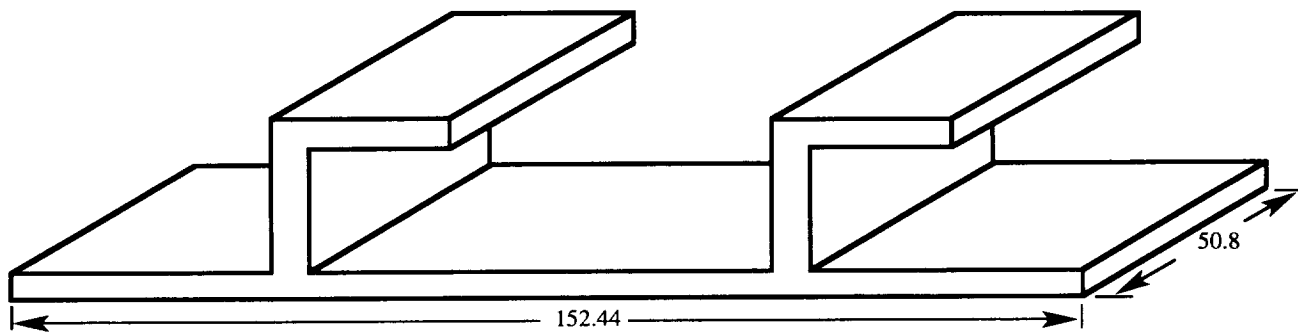
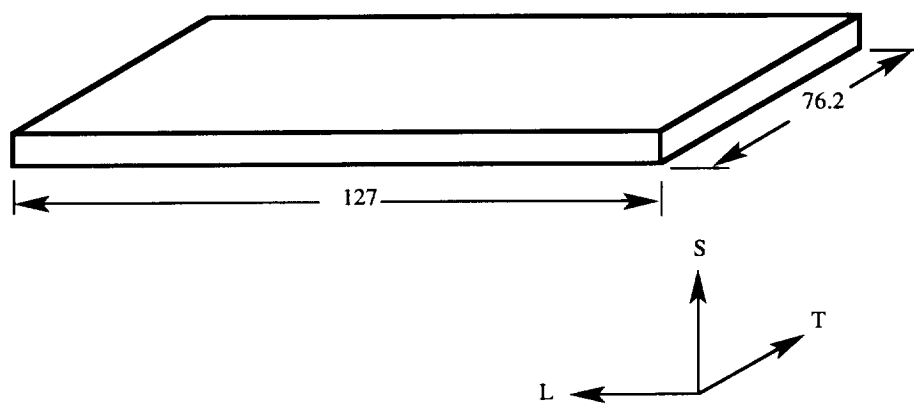


Figure B10. Alcoa exfoliation corrosion test specimen for EXCO test (full-panel thickness). Dimensions are in mm.

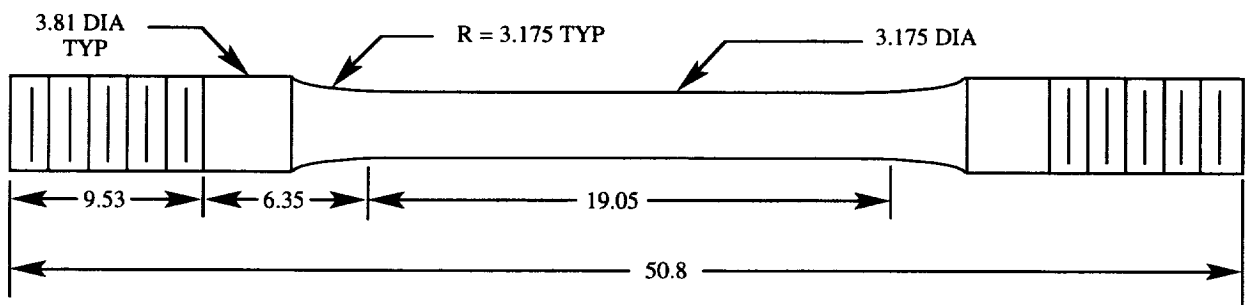


(a) Extrusion section with two stiffeners.

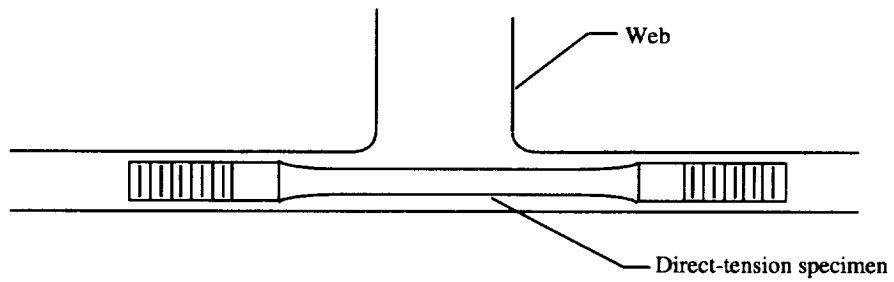


(b) Skin specimen.

Figure B11. Alcoa exfoliation corrosion test specimens for dry bottom MASTMAASIS test (full-panel thickness). Dimensions are in mm.



(a) Direct-tension specimen. Dimensions are in mm.



(b) Schematic of direct-tension specimen position.

Figure B12. LaRC direct-tension stress corrosion specimen.

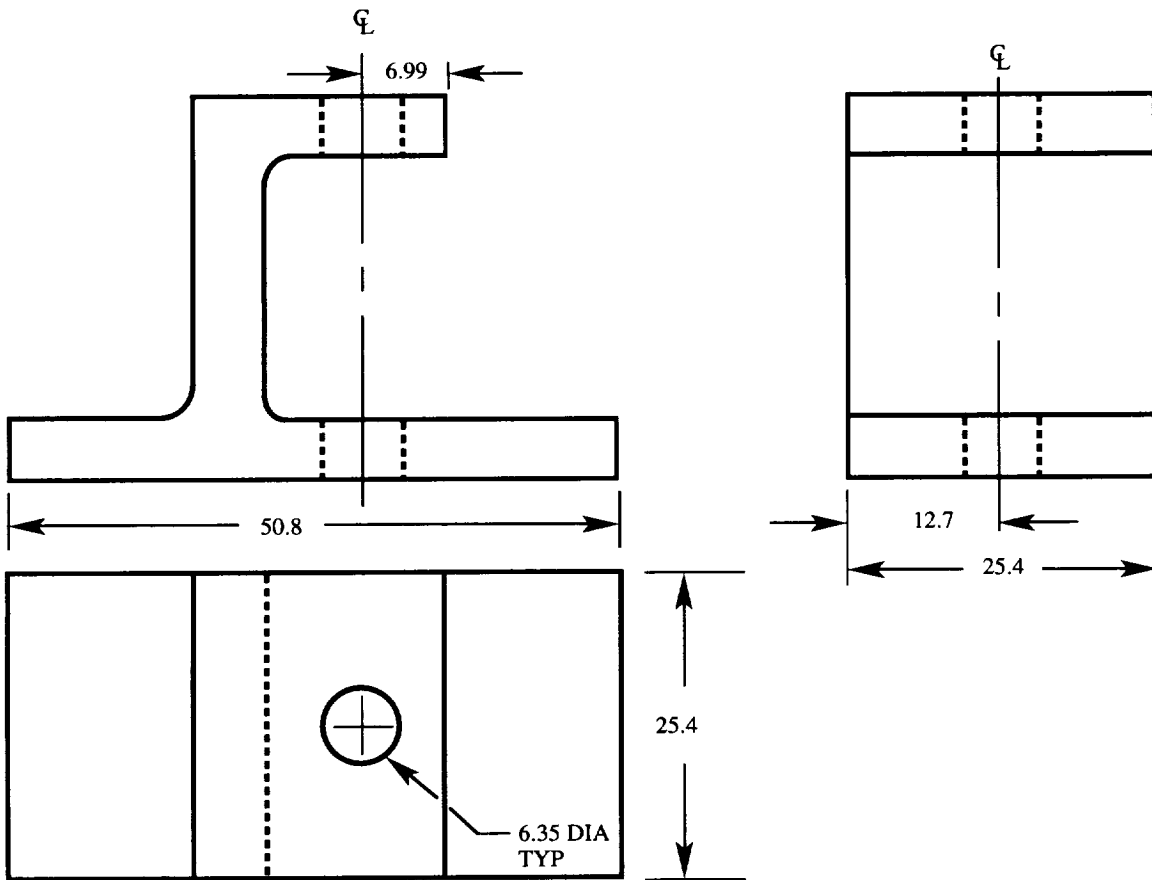
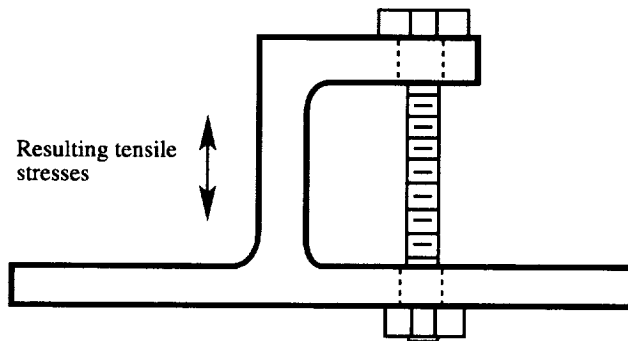
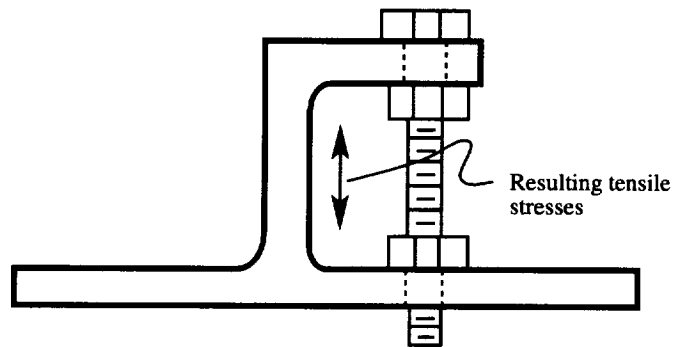


Figure B13. LaRC modified c-ring stress corrosion specimen. Dimensions are in mm.



(a) Tensile stresses at outer web/fillet.



(b) Tensile stresses at inner web/fillet.

Figure B14. Loading methods and resulting tensile stresses for modified c-ring specimen.

Appendix C

Test Results

Tables C1 through C17 present results for individual test specimens from tensile, fracture, and corrosion testing. Table C10 includes average tensile test results for panel 11 and reference literature results for 2219 and 2090 products.

Table C1. Alcoa Tensile Data at 25°C, Panels 1 and 10

Specimen	Nominal stretch, percent	Orientation	Location	Gauge length, mm	Thickness, mm	Width, mm	Breaking load, kN	S_y , MPa	S_u , MPa	EI, percent
1-L1	6	L	Skin	25.4	4.197	6.388	14.972	494.0	558.0	6.0
1-L2	6	L	Base	25.4	4.164	6.337	16.177	599.0	613.0	6.0
1-L3	6	L	Web	25.4	4.197	6.414	15.635	538.0	580.0	6.0
1-L4	6	L	Web-cap	25.4	4.190	6.363	15.813	555.0	593.0	7.0
1-L5	6	L	Cap	25.4	4.185	6.363	15.777	541.0	592.0	^a 5.0
1-LT6	6	LT	Base	25.4	4.188	6.337	15.172	510.0	572.0	9.0
1-LT7	6	LT	Skin	25.4	4.211	6.325	14.665	473.0	551.0	4.0
10-L1	3	L	Skin	25.4	4.201	6.363	15.168	509.0	567.0	8.0
10-L2	3	L	Base	25.4	4.204	6.350	16.836	620.0	631.0	7.0
10-L3	3	L	Web	25.4	4.178	6.350	15.568	546.0	587.0	8.0
10-L4	3	L	Web-cap	25.4	4.191	6.350	15.724	548.0	591.0	^a 8.0
10-L5	3	L	Cap	25.4	4.196	6.350	15.395	525.0	578.0	8.0
10-LT6	3	LT	Base	25.4	4.180	6.363	15.559	536.0	585.0	9.0
10-LT7	3	LT	Skin	25.4	4.183	6.350	14.843	497.0	558.0	4.0

^aBroke outside gauge mark.

Table C2. Boeing Aerospace Tensile Data at 25°C, Panels 4 and 7

Specimen	Nominal stretch, percent	Orientation	Location	Gauge length, mm	Thickness, mm	Width, mm	Breaking load, kN	S_y , MPa	S_u , MPa	EI, percent
4TY-A1	6	L	Skin	50.8	3.188	12.751	20.906	452.0	514.0	4.5
4TY-B1	6	L	Skin	50.8	3.213	12.751	20.016	429.0	489.0	4.0
4TY-C1	6	L	Skin	50.8	3.200	12.764	20.594	452.0	504.0	3.5
4TX-A1	6	LT	Skin	50.8	3.162	12.738	21.572	486.0	536.0	6.5
4TX-B1	6	LT	Skin	50.8	3.200	12.713	21.350	439.0	525.0	7.0
4TX-C1	6	LT	Skin	50.8	3.162	12.738	22.240	468.0	552.0	8.5
7TY-A1	3	L	Skin	50.8	3.188	12.713	23.107	510.0	570.0	9.0
7TY-B1	3	L	Skin	50.8	3.162	12.738	22.729	521.0	565.0	6.5
7TY-C1	3	L	Skin	50.8	3.200	12.751	23.041	516.0	587.0	9.5
7TX-A1	3	LT	Skin	50.8	3.175	12.700	21.773	451.0	540.0	9.5
7TX-B1	3	LT	Skin	50.8	3.200	12.738	22.196	492.0	545.0	9.0
7TX-C1	3	LT	Skin	50.8	3.188	12.751	22.062	492.0	543.0	8.0

Table C3. Boeing Aerospace Tensile Data at -196°C, Panel 4

Specimen	Nominal stretch, percent	Orientation	Location	Gauge length, mm	Thickness, mm	Width, mm	Breaking load, kN	S_y , MPa	S_u , MPa	EI, percent
4TX-A2	6	LT	Skin	50.8	3.175	12.738	23.841	442.0	589.0	14.5
4TX-B2	6	LT	Skin	50.8	3.200	12.738	23.263	427.0	571.0	13.0
4TX-C2	6	LT	Skin	50.8	3.213	12.751	24.064	461.1	587.0	9.5

Table C4. LaRC Tensile Data at 25°C, Panels 11, 6, 4, and 2

Specimen (a)	Nominal stretch, percent	Orientation	Location	Gauge length, mm	Thickness, mm	Width, mm	Breaking load, kN	S_y , MPa	S_u , MPa	EI, percent
11-T1	6	L	Skin	25.4	4.22	6.34	15.28	532.0	571.0	7.4
11-T1	6	L	Skin	25.4	4.22	6.32	15.27	(b)	572.0	(b)
11-T2	6	L	Skin	25.4	3.59	6.32	12.88	515.0	567.0	4.9
11-T2	6	L	Skin	25.4	3.59	6.33	12.83	509.0	564.0	5.6
11-T3	6	L	Skin	25.4	3.63	6.32	12.54	490.0	547.0	3.8
11-T3	6	L	Skin	25.4	3.62	6.35	12.39	496.0	551.0	3.7
6-T4	6	L	Skin	25.4	4.18	6.35	15.04	513.0	567.0	5.2
6-T4	6	L	Skin	25.4	4.29	6.32	15.27	520.0	562.0	7.1
4-TY	6	L	Skin	25.4	4.63	6.27	15.19	457.0	523.0	3.5
4-TY	6	L	Skin	25.4	4.46	6.25	14.33	446.0	514.0	4.4
2-T5	3	L	Skin	25.4	3.20	6.39	11.51	501.0	563.0	5.0
2-T5	3	L	Skin	25.4	3.19	6.43	11.57	506.0	564.0	4.0
11-T2	6	LT	Skin	25.4	3.65	6.33	13.52	546.0	584.0	6.7
11-T2	6	LT	Skin	25.4	3.66	6.33	13.56	548.0	585.0	7.5
11-T3	6	LT	Skin	25.4	3.60	6.35	13.03	506.0	569.0	7.0
11-T3	6	LT	Skin	25.4	3.59	6.32	13.04	511.0	575.0	7.4
6-T4	6	LT	Skin	25.4	3.55	6.29	12.66	524.0	568.0	7.2
6-T4	6	LT	Skin	25.4	3.72	6.33	13.24	512.0	562.0	8.8
4-TX	6	LT	Skin	25.4	4.24	6.24	13.81	428.0	522.0	5.3
4-TX	6	LT	Skin	25.4	4.63	6.27	13.86	392.0	478.0	5.0
2-T5	3	LT	Skin	25.4	3.33	6.32	12.12	524.0	575.0	6.6
2-T5	3	LT	Skin	25.4	3.34	6.41	12.30	521.0	574.0	5.2
2-T5	3	45°	Skin	25.4	3.53	6.37	11.62	448.0	516.0	6.0
2-T5	3	45°	Skin	25.4	3.52	6.48	11.57	440.0	507.0	7.5
11-T2	6	L	Cap	25.4	5.48	6.32	21.61	596.0	627.0	5.9
11-T2	6	L	Cap	25.4	4.44	6.24	17.46	611.0	629.0	7.6
11-T3	6	L	Cap	25.4	5.45	6.36	21.65	595.0	624.0	6.1
11-T3	6	L	Cap	25.4	4.30	6.39	17.18	599.0	624.0	5.2
6-T4	6	L	Cap	25.4	4.62	6.26	18.08	598.0	625.0	7.4
6-T4	6	L	Cap	25.4	4.64	6.32	18.35	594.0	626.0	6.0
2-T5	3	L	Cap	25.4	5.55	6.32	21.58	583.0	615.0	6.9
2-T5	3	L	Cap	25.4	5.49	6.35	21.46	582.0	615.0	7.4
11-T2	6	L	Web	25.4	5.39	6.31	19.62	531.0	577.0	7.0
11-T2	6	L	Web	25.4	5.39	6.38	19.70	522.0	572.0	5.0
11-T3	6	L	Web	25.4	4.64	6.36	17.17	532.0	581.0	5.1
11-T3	6	L	Web	25.4	5.46	6.34	20.02	520.0	578.0	5.7
6-T4	6	L	Web	25.4	5.61	6.31	20.13	519.0	569.0	5.9
6-T4	6	L	Web	25.4	5.62	6.30	20.08	517.0	568.0	4.9
6-T4	6	L	Base	25.4	4.27	6.29	16.64	598.0	620.0	3.3
6-T4	6	L	Base	25.4	4.47	6.30	17.55	613.0	624.0	3.8
2-T5	3	L	Base	25.4	3.57	6.31	13.72	592.0	609.0	4.9
2-T5	3	L	Base	25.4	3.55	6.32	13.60	590.0	606.0	2.8
11-T1	6	LT	Base	25.4	4.19	6.32	14.91	533.0	564.0	1.0
11-T1	6	LT	Base	25.4	4.19	6.32	14.92	523.0	562.0	2.4
11-T2	6	LT	Base	25.4	3.38	6.33	12.02	514.0	562.0	3.7
11-T2	6	LT	Base	25.4	3.40	6.34	12.06	508.0	559.0	4.6
11-T3	6	LT	Base	25.4	3.60	6.34	12.42	469.0	544.0	3.4
11-T3	6	LT	Base	25.4	3.31	6.33	11.27	467.0	538.0	4.0
6-T4	6	LT	Base	25.4	3.99	6.23	14.17	518.0	564.0	3.4
6-T4	6	LT	Base	25.4	3.86	6.32	13.75	516.0	563.0	3.3
2-T5	3	LT	Base	25.4	2.93	6.40	10.65	528.0	567.0	2.2
2-T5	3	LT	Base	25.4	2.91	6.39	10.51	527.0	564.0	3.0

^aSpecimen location:

T1 front of panel 11

T2 middle of panel 11

T3 back of panel 11

T4 front of panel 6

T5 middle of panel 2

TX Boeing Aerospace specimen, panel 4

TY Boeing Aerospace specimen, panel 4

^bNot available.

Table C5. MSFC Tensile Data at 25°C, Panels 11 and 2

Specimen (a)	Nominal stretch, percent	Orientation	Location	Gauge length, mm	Thickness, mm (b)	Width, mm (b)	Breaking load, kN (b)	S_y , MPa	S_u , MPa	El, percent
11-T1	6	L	Skin	50.8	NA	NA	NA	517.0	547.0	2.5
11-T1	6	L	Skin	50.8	NA	NA	NA	513.0	541.0	4.1
11-T1	6	LT	Skin	50.8	NA	NA	NA	565.0	585.0	2.0
11-T2	6	LT	Skin	50.8	NA	NA	NA	541.0	577.0	3.2
11-T3	6	LT	Skin	50.8	NA	NA	NA	514.0	563.0	5.0
11-T1	6	LT	Base	50.8	NA	NA	NA	563.0	587.0	0.9
11-T2	6	LT	Base	50.8	NA	NA	NA	528.0	567.0	0.8
11-T3	6	LT	Base	50.8	NA	NA	NA	483.0	534.0	1.6
2-T5	3	L	Skin	50.8	NA	NA	NA	515.0	548.0	3.4
2-T5	3	LT	Skin	50.8	NA	NA	NA	543.0	582.0	4.3
2-T5	3	LT	Base	50.8	NA	NA	NA	530.0	572.0	1.3

^aSpecimen location:

- T1 front of panel 11
- T2 middle of panel 11
- T3 back of panel 11
- T5 middle of panel 2

^bNA indicates not available.

Table C6. MSFC Tensile Data at -196°C, Panels 11 and 2

Specimen (a)	Nominal stretch, percent	Orientation	Location	Gauge length, mm	Thickness, mm (b)	Width, mm (b)	Breaking load, kN (b)	S_y , MPa	S_u , MPa	El, percent
11-T1	6	L	Skin	50.8	NA	NA	NA	556.0	604.0	2.1
11-T2	6	L	Skin	50.8	NA	NA	NA	585.0	663.0	4.2
11-T2	6	L	Skin	50.8	NA	NA	NA	557.0	614.0	2.6
11-T3	6	L	Skin	50.8	NA	NA	NA	543.0	668.0	9.8
11-T3	6	L	Skin	50.8	NA	NA	NA	521.0	656.0	9.2
11-T1	6	LT	Skin	50.8	NA	NA	NA	(c)	627.0	(c)
11-T1	6	LT	Skin	50.8	NA	NA	NA	(c)	544.0	(c)
11-T2	6	LT	Skin	50.8	NA	NA	NA	(c)	730.0	(c)
11-T2	6	LT	Skin	50.8	NA	NA	NA	610.0	656.0	1.9
11-T3	6	LT	Skin	50.8	NA	NA	NA	571.0	703.0	8.8
11-T3	6	LT	Skin	50.8	NA	NA	NA	554.0	688.0	8.2
11-T1	6	LT	Base	50.8	NA	NA	NA	612.0	621.0	1.0
11-T1	6	LT	Base	50.8	NA	NA	NA	620.0	650.0	1.3
11-T2	6	LT	Base	50.8	NA	NA	NA	592.0	650.0	1.8
11-T2	6	LT	Base	50.8	NA	NA	NA	591.0	645.0	2.8
11-T3	6	LT	Base	50.8	NA	NA	NA	540.0	626.0	2.7
11-T3	6	LT	Base	50.8	NA	NA	NA	541.0	623.0	1.6
2-T5	3	L	Skin	50.8	NA	NA	NA	532.0	607.0	2.9
2-T5	3	L	Skin	50.8	NA	NA	NA	534.0	654.0	8.3
2-T5	3	LT	Skin	50.8	NA	NA	NA	605.0	689.0	3.1
2-T5	3	LT	Skin	50.8	NA	NA	NA	604.0	650.0	3.3
2-T5	3	LT	Base	50.8	NA	NA	NA	530.0	627.0	2.9
2-T5	3	LT	Base	50.8	NA	NA	NA	546.0	621.0	0.5

^aSpecimen location:

- T1 front of panel 11
- T2 middle of panel 11
- T3 back of panel 11
- T5 middle of panel 2

^bNA indicates not available.^cSpecimen broke outside gauge marks.

Table C7. MSFC Tensile Data at -253°C, Panels 11 and 2

Specimen (a)	Nominal stretch, percent	Orientation	Location	Gauge length, mm	Thickness, mm (b)	Width, mm (b)	Breaking load, kN (b)	S_y , MPa	S_u , MPa	EI, percent
11-T1	6	L	Skin	50.8	NA	NA	NA	611.0	667.0	3.2
11-T1	6	L	Skin	50.8	NA	NA	NA	611.0	664.0	^c 2.4
11-T2	6	L	Skin	50.8	NA	NA	NA	585.0	641.0	2.4
11-T2	6	L	Skin	50.8	NA	NA	NA	572.0	653.0	3.8
11-T3	6	L	Skin	50.8	NA	NA	NA	532.0	619.0	3.2
11-T3	6	L	Skin	50.8	NA	NA	NA	541.0	658.0	5.0
11-T1	6	LT	Skin	50.8	NA	NA	NA	659.0	670.0	0.4
11-T2	6	LT	Skin	50.8	NA	NA	NA	614.0	625.0	(d)
11-T2	6	LT	Skin	50.8	NA	NA	NA	614.0	665.0	1.4
11-T3	6	LT	Skin	50.8	NA	NA	NA	563.0	633.0	2.3
11-T3	6	LT	Skin	50.8	NA	NA	NA	558.0	632.0	2.5
11-T1	6	LT	Base	50.8	NA	NA	NA	641.0	683.0	0.9
11-T1	6	LT	Base	50.8	NA	NA	NA	642.0	671.0	0.7
11-T2	6	LT	Base	50.8	NA	NA	NA	586.0	662.0	2.3
11-T2	6	LT	Base	50.8	NA	NA	NA	590.0	687.0	2.6
11-T3	6	LT	Base	50.8	NA	NA	NA	562.0	641.0	1.9
2-T5	3	L	Skin	50.8	NA	NA	NA	532.0	659.0	6.2
2-T5	3	LT	Skin	50.8	NA	NA	NA	604.0	662.0	1.1
2-T5	3	LT	Skin	50.8	NA	NA	NA	616.0	663.0	(d)
2-T5	3	LT	Base	50.8	NA	NA	NA	523.0	610.0	^c 1.7
2-T5	3	LT	Base	50.8	NA	NA	NA	539.0	625.0	2.6

^aSpecimen location:

T1 front of panel 11

T2 middle of panel 11

T3 back of panel 11

T5 middle of panel 2

^bNA indicates not available.^cSpecimen broke at gauge mark.^dSpecimen broke outside gauge marks.

Table C8. Boeing Aerospace Surface Crack (PS(T)) Fracture Tests, Panels 4 and 7

Specimen (a)	Nominal stretch, percent	Temperature, °C	Orientation	W, mm	a, mm	2c, mm	B, mm	Residual strength, MPa	S_{net} , MPa	K_{Ic} , \sqrt{m}
4FX-1	6	25	T-S	63.50	2.82	10.29	3.35	386.75	433.09	^b 40.22
4FX-3	6	25	T-S	63.47	2.64	9.96	3.43	400.54	442.54	^b 40.44
4FY-1	6	25	L-S	63.50	2.67	9.73	3.35	375.72	415.49	^b 37.59
4FY-3	6	25	L-S	63.45	2.57	9.78	3.33	391.58	431.89	^b 39.12
4FX-4	6	-196	T-S	63.47	2.67	10.03	3.40	333.67	416.63	^b 33.85
4FY-2	6	-196	L-S	63.45	2.36	9.96	3.38	430.19	368.71	^b 42.75
4FY-4	6	-196	L-S	63.47	2.41	10.11	3.51	^c 444.66	369.62	^{b,c} 44.29
7FX-1	3	25	T-S	63.55	2.69	9.93	3.30	372.97	470.76	^b 37.92
7FY-1	3	25	L-S	63.53	2.49	9.83	3.53	337.12	486.56	^b 33.19
7FX-2	3	-196	T-S	63.47	2.46	9.88	3.38	^c 192.34	211.17	^c 19.23
7FY-2	3	-196	L-S	63.47	2.41	10.01	3.38	^c 406.75	446.21	^{b,c} 40.66

^aSemicircular flaws, $a/c = 0.48$ to 0.54 .^bNot valid per ASTM E740-88, Section X3.2.2, crack depth (a) and remaining ligament (B-a) not greater than $0.5(K_{Ic}/\sigma_{ys})^2$.^cNot valid per ASTM E740-88, Section 6.3.2.2, fatigue crack less than 5 percent of final crack depth.

Table C9. NIST Surface Crack (PS(T)) Fracture Tests, Panel 6

Specimen (a)	Nominal stretch, percent	Temperature, °C	Orientation	W, mm	a, mm	2c, mm	B, mm	Residual strength, MPa	S_{net} , MPa	K_{Ic} , MPa \sqrt{m}
A1-RT	6	25	T-S	101.60	3.87	19.97	4.10	187.00	218.69	^b 28.60
A2-RT	6	25	T-S	101.60	3.74	19.95	4.08	220.00	255.94	^b 33.70
A3-LN2	6	-196	T-S	101.60	2.93	20.32	4.08	231.00	260.14	^b 32.70
A4-LN2	6	-196	T-S	101.60	2.85	19.53	4.10	257.00	287.34	^b 35.20
A5-LHe	6	-269	T-S	101.60	2.84	19.41	4.05	281.00	314.18	^b 38.50
A6-LHe	6	-269	T-S	101.60	2.75	20.25	4.05	267.00	298.53	^b 36.70
B1-RT	6	25	T-S	63.50	2.62	7.44	4.16	397.00	421.21	^b 32.00
B2-RT	6	25	T-S	63.50	2.44	5.97	4.05	336.00	351.40	23.60
B3-LN2	6	-196	T-S	63.50	2.44	6.18	4.03	346.00	362.80	24.90
B4-LN2	6	-196	T-S	63.50	2.41	6.46	4.05	287.00	301.15	21.20
B5-LHe	6	-269	T-S	63.50	2.84	6.46	4.05	308.00	319.26	22.80
B6-LHe	6	-269	T-S	63.50	2.41	6.34	4.08	336.00	352.06	24.50

^aSemielliptical flaws, $a/c = 0.28$ to 0.38 ; semicircular flaws, $a/c = 0.72$ to 0.38 .

^bNot valid per ASTM E740-88, Section X3.2.2, crack depth (a) and remaining ligament (B-a) not greater than $0.5(K_{Ic}/\sigma_{ys})^2$.

Table C10. Tensile Properties for 2090 Near Net Shape Extrusion and Other Aluminum Products

Product form	Thickness, mm	Temperature, °C	Longitudinal			Transverse			Ref.
			S_y , MPa	S_u , MPa	El, percent	S_y , MPa	S_u , MPa	El, percent	
2090-T86 Ext		25	515.0	544.0	3.3	540.0	563.0	3.4	(a)
2090-T86 Ext		-196	552.0	641.0	5.6	578.0	658.0	6.3	(a)
2090-T86 Ext		-253	575.0	655.0	3.3	602.0	645.0	1.7	(a)
2219-T87 Sheet	1.6	25	401.6	480.8	9.8	397.9	482.9	10.1	31
2219-T87 Sheet	1.6	-196	462.7	589.9	15.0	452.7	597.1	12.0	31
2219-T87 Sheet	1.6	-253	493.0	640.9	16.8	509.2	694.0	14.2	31
2219-T87 Plate	38.1	25	370.1	456.4	10.0	359.9	450.7	10.0	31
2219-T87 Plate	38.1	-196	449.1	579.3	11.9	437.4	569.9	12.4	31
2219-T87 Plate	38.1	-253	501.8	703.3	15.7	482.4	683.8	13.1	31
2090-T86 Ext	T-section	25	572.3	575.0	7.9	530.9	544.7	7.4	11
2090-T86 Ext	T-section	25	537.8	567.5	6.0	457.1	486.1	11.0	32
2090-T8 Sheet	1.6	25	505.0	549.0	6.8				33
2090-T8 Sheet	1.6	-196	568.0	674.0	8.0				33
2090-T83 Sheet	1.6	25	510.2	551.6	6.3	496.4	537.8	7.8	11
2090-T81 Plate	12.7	25	503.3	530.9	7.0	503.3	544.7	2.0	30
2090-T81 Plate	12.7	25	544.7	586.1	7.6	551.6	586.1	6.2	11
2090-T81 Plate	12.7	25	558.5	593.0	8.0	551.6	586.1	6.0	34
2090-T81 Plate	12.7	-196	551.6	613.7	9.0	565.4	606.8	1.0	30
2090-T81 Plate	12.7	-196	599.9	717.1	14.0	627.4	696.4	6.0	34
2090-T81 Plate	12.7	-253	591.0	715.0	12.0	613.0	666.0	1.0	30
2090-T81 Plate	19.1	25	579.2	606.8	8.0	558.5	599.9	6.0	30
2090-T81 Plate	19.1	-196	648.1	737.8	10.0	620.6	689.5	3.0	30
2090-T81 Plate	19.1	-253	665.0	836.0	15.0	663.0	764.0	4.0	30

^aMSFC data from panel 11.

Table C11. Boeing Aerospace Weldment Tensile Data, Panels 4 and 7

Specimen	Nominal stretch, percent	Orientation	Temperature, °C	Gauge length, mm	Thickness, mm	Width, mm	S_y , MPa	S_u , MPa	El, percent
W4AX-T1	6	L	25	25.4	2.88	25.35	173.7	331.6	7.0
W4AX-T3	6	L	25	25.4	2.79	25.40	182.0	325.4	9.0
W4AX-T4	6	L	25	25.4	2.85	25.50	177.9	337.8	10.0
W4AX-T6	6	L	25	25.4	2.74	25.37	182.0	325.4	7.0
W4AX-T2	6	L	-196	25.4	2.67	25.37	236.5	393.6	5.0
W4AX-T5	6	L	-196	25.4	2.87	25.25	226.1	381.9	6.0
W4BX-T1	6	L	25	25.4	3.48	25.55	170.3	295.1	6.0
W4BX-T3	6	L	25	25.4	3.48	25.40	164.1	282.0	9.0
W4BX-T4	6	L	25	25.4	3.43	25.50	173.0	292.3	7.0
W4BX-T6	6	L	25	25.4	3.38	25.32	177.9	312.3	8.0
W4BX-T2	6	L	-196	25.4	3.53	25.35	206.8	320.6	5.0
W4BX-T5	6	L	-196	25.4	3.43	25.43	221.3	338.5	5.0
W4CX-T3	6	L	25	25.4	3.18	25.53	175.8	318.5	9.0
W4CX-T4	6	L	-196	25.4	3.20	25.43		405.4	
WSAX-T1	6	L	25	25.4	3.71	25.58	164.1	295.1	8.0
WSAX-T3	6	L	25	25.4	3.68	25.55	175.1	297.1	9.0
WSAX-T4	6	L	25	25.4	3.81	25.53	167.5	252.3	6.0
WSAX-T6	6	L	25	25.4	3.58	25.53	177.9	302.0	11.0
WSAX-T2	6	L	-196	25.4	3.66	25.40	191.7	368.8	5.0
WSAX-T5	6	L	-196	25.4	3.78	25.63	206.1	295.8	5.0
W4CY-T1	6	LT	25	25.4	3.73	25.43	196.5	296.4	6.0
W4CY-T2	6	LT	-196	25.4	3.78	25.73	206.8	358.5	7.0
WSBY-T1	6	LT	25	25.4	3.23	25.65	164.8	320.6	9.0
WSBY-T3	6	LT	25	25.4	3.45	25.53	151.7	297.1	9.0
WSBY-T4	6	LT	25	25.4	3.48	25.68	168.2	294.4	10.0
WSBY-T6	6	LT	25	25.4	3.63	26.67	142.7	275.1	9.0
WSBY-T2	6	LT	-196	25.4	3.25	25.65	213.0	406.7	10.0
WSBY-T5	6	LT	-196	25.4	3.66	25.15	198.5	348.8	10.0
W7AX-T1	3	L	25	25.4	2.72	25.27	219.2	336.4	9.0
W7AX-T3	3	L	25	25.4	2.77	25.27	222.0	342.6	9.0
W7AX-T4	3	L	25	25.4	3.51	25.40	195.1	297.8	6.0
W7AX-T6	3	L	25	25.4	3.12	22.86	239.9	373.7	8.0
W7AX-T2	3	L	-196	25.4	2.72	25.32	266.8	413.6	5.0
W7AX-T5	3	L	-196	25.4	2.90	25.15	275.1	413.0	5.0

Table C12. Boeing Aerospace Weldment Surface Crack (PS(T)) Fracture Tests, Panels 4 and 7

Specimen (a)	Nominal stretch, percent	Temperature, °C	Orientation	W, mm	a, mm	2c, mm	B, mm	Residual strength, MPa	S_{net} , MPa	K_{Ie} , $\frac{MPa}{\sqrt{m}}$
W4AX-F1	6	25	T-S	101.55	2.39	8.84	2.39	^c 219.23	232.05	^{b,c} 21.43
W4BX-F1	6	25	T-S	101.55	2.03	9.12	2.54	217.16	230.14	^b 21.54
W4CY-F1	6	25	L-S	101.55	1.91	8.89	2.84	215.09	225.47	^b 20.00
W4CY-F4	6	25	L-S	101.35	2.01	9.02	2.51	^c 210.27	222.65	^{b,c} 20.66
W4AX-F2	6	-196	T-S	101.63	2.18	9.63	2.59	244.05	227.54	^b 25.17
W4BX-F2	6	-196	T-S	101.47	1.96	9.12	2.77	246.81	260.39	^b 23.63
W4CY-F2	6	-196	L-S	101.42	2.06	9.27	2.67	^c 214.40	259.74	^{b,c} 21.10
W4CY-F3	6	-196	L-S	101.52	1.93	8.99	2.62	^c 246.12	226.95	^{b,c} 23.63
W7AX-F1	3	25	T-S	101.55	2.46	9.80	3.07	213.71	259.42	^b 21.76
W7AX-F2	3	-196	T-S	101.55	2.41	9.55	3.10	248.18	263.32	^b 24.73

^aSemicircular flaws, $a/c = 0.48$ to 0.54 .^bNot valid per ASTM E740-88, Section X3.2.2, crack depth (a) and remaining ligament (B-a) not greater than $0.5(K_{Ie}/\sigma_{ys})^2$.^cNot valid per ASTM E740-88, Section 7.2, variation in specimen thickness greater than 5 percent.

Table C13. NIST Weldment Surface Crack (PS(T)) Fracture Tests, Panel 3

Specimen (a)	Nominal stretch, percent	Temperature, °C	Orientation	W, mm	a, mm	2c, mm	B, mm	Residual strength, MPa	Snet, MPa	K_{Ie}, \sqrt{m}
W1-2/W2-2	6	25	T-S	63.50	3.26	20.87	4.49	161.00	197.94	^b 23.50
W3-1/W5-1	6	25	T-S	63.50	2.62	19.26	4.28	191.00	223.46	^b 24.60
W4-1/W5-2	6	-269	T-S	63.50	2.65	19.71	4.36	208.00	243.95	^b 27.00
W1-1/W2-1	6	25	T-S	63.50	2.62	5.95	4.06	199.00	208.92	^c 13.90
W3-1/W5-1	6	25	T-S	63.50	2.35	5.78	4.15	216.00	225.19	^c 14.70
W4-1/W5-2	6	-269	T-S	63.50	3.08	6.53	4.28	257.00	272.77	^c 18.80
W1-2/W2-2	6	-269	T-S	63.50	2.58	7.28	4.56	248.00	261.33	^c 19.60

^aSemielliptical flaws, $a/c = 0.28$ to 0.38 ; semicircular flaws, $a/c = 0.72$ to 0.94 .

^bNot valid per ASTM E740-88, Section X3.2.2, general yielding occurred.

^cNot valid per ASTM E740-88, Section X3.2.2, stable crack growth occurred.

Table C14. Alcoa Exfoliation Test Data for 2090-T86 Extrusion, Panel 6

Specimen	Specimen number	24 hr	48 hr	72 hr	96 hr
50.8-mm × 101.6-mm skin panel	682873	N ^a	EA	EA	EB

^aRatings per ASTM G34-90:

N no appreciable attack
EA superficial exfoliation
EB moderate exfoliation

Table C15. Alcoa MASTMAASIS Exfoliation Test Data for 2090-T86 Extrusion, Panel 6

Specimen	Specimen number	1 week	2 weeks	4 weeks
50.8-mm × 101.6-mm skin panel	682873	N (P) ^a	P	P
Extrusion section with two stiffeners	682855-1 Exposed with stiffeners upright	N (P)	N (P)	N (P)
Extrusion section with two stiffeners	682855-2 Exposed with stiffeners facing down	N (P)	N (P)	N (P)

^aRatings per ASTM G34-90:

N no appreciable attack
P pitting

Table C16. LaRC Direct-Tension Stress Corrosion Data for 2090-T86 Extrusion, Panel 6

Specimen	Exposure stress, MPa	Exposure time, days	Breaking stress, MPa	Mean breaking stress Standard deviation
16	0	0	579.19	583.39 ± 7.89
17	0	0	592.50	
18	0	0	578.49	
1	0	40	504.87	512.40 ± 6.65
3	0	40	517.43	
4	0	40	514.95	
5	136	40	502.80	498.09 ± 4.47
6	136	40	497.56	
7	136	40	493.90	
8	273	40	495.49	495.86 ± 1.08
11	273	40	497.08	
12	273	40	495.01	
13	409	40	495.49	494.22 ± 2.49
14	409	40	495.83	
15	409	40	491.35	

Table C17. LaRC Stress Corrosion Data for Modified c-Ring Specimen, 2090-T86 Extrusion, Panel 6

Specimen	Exposure stress	Tensile stress locations (a)	Masked area	Pass/fail (b)
1	0	NA	None	P
2	0	NA	None	P
3	0	NA	None	P
4	0	NA	None	P
5	70% S_y	1	Bolt	P
7	70% S_y	1	Bolt	P
8	70% S_y	1	Bolt	P
9	70% S_y	1	Bolt	P
10	70% S_y	2	Bolt and web	P
6	70% S_y	3	Bolt	P
11	70% S_y	3	Bolt	P
12	70% S_y	3	Bolt	P
13	70% S_y	3	Bolt	P
14	70% S_y	4	Bolt and web	P

^aLocation definitions:

NA not applicable

1 tensile stresses at outer web and fillet; maximum at mid web at specimen edge

2 tensile stresses at outer fillet; maximum at middle of web-skin fillet

3 tensile stresses at inner web and fillets; maximum at middle of web-skin fillet

4 tensile stresses at inner radii; maximum at middle of lower fillet

^bPass (P) or fail rating after 75-day exposure.

REPORT DOCUMENTATION PAGE			Form Approved OMB No. 07704-0188	
Public reporting burden for this collection of information is estimated to average 1 hour per response, including the time for reviewing instructions, searching existing data sources, gathering and maintaining the data needed, and completing and reviewing the collection of information. Send comments regarding this burden estimate or any other aspect of this collection of information, including suggestions for reducing this burden, to Washington Headquarters Services, Directorate for Information Operations and Reports, 1215 Jefferson Davis Highway, Suite 1204, Arlington, VA 22202-4302, and to the Office of Management and Budget, Paperwork Reduction Project (0704-0188), Washington, DC 20503.				
1. AGENCY USE ONLY (Leave blank)	2. REPORT DATE May 1998	3. REPORT TYPE AND DATES COVERED Technical Memorandum		
4. TITLE AND SUBTITLE Characterization of Al-Cu-Li Alloy 2090 Near Net Shape Extrusion			5. FUNDING NUMBERS WU 232-01-04-07	
6. AUTHOR(S) M. J. Birt, M. S. Domack, R. A. Hafley, and W. D. Pollock				
7. PERFORMING ORGANIZATION NAME(S) AND ADDRESS(ES) NASA Langley Research Center Hampton, VA 23681-2199			8. PERFORMING ORGANIZATION REPORT NUMBER L-17611	
9. SPONSORING/MONITORING AGENCY NAME(S) AND ADDRESS(ES) National Aeronautics and Space Administration Washington, DC 20546-0001			10. SPONSORING/MONITORING AGENCY REPORT NUMBER NASA/TM-1998-207668	
11. SUPPLEMENTARY NOTES Birt, Hafley, and Pollock: Analytical Services & Materials, Inc., 107 Research Drive, Hampton, Virginia. Domack: NASA Langley Research Center, Hampton, Virginia.				
12a. DISTRIBUTION/AVAILABILITY STATEMENT Unclassified-Unlimited Subject Category 26 Availability: NASA CASI (301) 621-0390			12b. DISTRIBUTION CODE Distribution: Standard	
13. ABSTRACT (Maximum 200 words) Aluminum-lithium (Al-Li) alloys near net shape extrusions are being evaluated for potential application in launch vehicle structures. The objective of this study was to determine tensile and fracture properties, corrosion resistance, and weldability of integrally stiffened panels of Al-Cu-Li alloy 2090 in the T8 temper. The microstructure was predominantly unrecrystallized. Texture analyses revealed the presence of fiber components in the stiffeners and a combination of fiber and rolling components in the skin. Variations in grain morphology and texture through the extruded cross section were correlated with the tensile, fracture, and corrosion behavior. Tensile strengths at room and cryogenic temperatures of the 2090 extrusions were similar to other 2090 product forms and were higher than 2219-T87, the primary structural material in the Space Shuttle external tank; however, ductilities were lower. The fracture resistance of the 2090 extrusion was lower than 2219-T87 plate at room temperature. At cryogenic temperatures, tensile ductility and fracture behavior of the 2090 extrusion were similar to other 2090 product forms but were lower than 2219-T87 plate. The exfoliation and stress corrosion resistance of the 2090 extrusion compared favorably with the characteristics of other 2090 product forms. The weldability and weldment properties of the extrusions were similar to 2090 and 2219 plates.				
14. SUBJECT TERMS Al-Cu-Li alloy; 2090; Near-net extrusion; Cryogenic properties; Fracture; Tensile properties; Corrosion			15. NUMBER OF PAGES 75	
			16. PRICE CODE A04	
17. SECURITY CLASSIFICATION OF REPORT Unclassified	18. SECURITY CLASSIFICATION OF THIS PAGE Unclassified	19. SECURITY CLASSIFICATION OF ABSTRACT Unclassified	20. LIMITATION OF ABSTRACT	